
GPS Analysis: Strain, Transients, and Colored Noise

Matthias Hackl



München 2012

GPS Analysis: Strain, Transients, and Colored Noise

Matthias Hackl

Dissertation
zur Erlangung des Doktorgrades
an der Fakultät für Geowissenschaften der
Ludwig-Maximilians-Universität München

vorgelegt von
Matthias Hackl
aus Bad Tölz

München, den 08. Mai 2012

-
- 1. Gutachter:** Prof. Dr. Valerian Bachtadse
 - 2. Gutachter:** Prof. Dr. Urs Hugentobler
- Tag der mündlichen Prüfung: 13.07.2012

Zusammenfassung

Satellitengestützte geodätische Messmethoden, insbesondere GPS (Global Positioning System), sind von zunehmender Bedeutung in den Geowissenschaften und erlauben neue Einblicke in verschiedenste geophysikalische Prozesse. Zeitreihen hochpräziser Positionsmessungen von Punkten auf der Erdoberfläche ermöglichen unter anderem die Bestimmung von Relativgeschwindigkeiten tektonischer Einheiten, die Messung von Verformungsraten der Kruste an aktiven Störungen und Vulkanen und erlauben es Rückschlüsse auf die rheologischen Parameter der Lithosphäre und der Asthenosphäre zu ziehen. Mit zunehmender Länge und Genauigkeit der Zeitreihen ist es möglich, auch zeitabhängige dynamische tektonische Prozesse in GPS Zeitreihen zu identifizieren.

Die Schwierigkeiten in der Interpretation der Messungen bestehen unter anderem darin, von Punktmessungen auf kontinuierliche Deformationsmuster zu schließen, zeitlich korreliertes Rauschen zu quantifizieren, um realistische Fehlergrenzen anzugeben, und schließlich zeitabhängige tektonische Signale von zeitabhängigem Rauschen zu trennen. In dieser Arbeit werden Lösungsansätze zu diesen Punkten erarbeitet. Zunächst wird ein Algorithmus entwickelt, durch den aus einem diskreten Geschwindigkeitsfeld, ohne Vorgabe weiterer Randbedingungen (Geometrie der Störungen etc.), der kontinuierliche zweidimensionale Tensor der Verformungsraten abgeleitet werden kann. Aus der Tensoranalysis erhält man Informationen zur maximalen Scher- und Rotationsverformungsrate, sowie zur Dilatationsrate. Die Anwendung dieses Algorithmus auf verschiedene Datensätze in Südkalifornien und Island zeigt, dass hiermit sowohl aktive Störungen identifiziert, als auch Informationen über Bruchflächen von Erdbeben aus ko- bzw. postseismischen GPS Messungen abgeleitet werden können. Außerdem wurden zeitabhängige Signale in den GPS Geschwindigkeitsfeldern ersichtlich.

Im zweiten Teil dieser Arbeit wird ein weiterer Algorithmus eingeführt, der unter Berücksichtigung der Effekte zeitabhängigen Rauschens

die Berechnung der Varianz innerhalb von GPS Geschwindigkeitsfeldern ermöglicht. Somit wird außerdem der Notwendigkeit Rechnung getragen, realistische Fehlergrenzen als Grundlage zur Konfidenzabschätzung von Modellen zu definieren. Dieser Algorithmus basiert auf der Allan Varianz, die bei der Messung der Stabilität von Oszillatoren Verwendung findet und ausschließlich im Zeitbereich berechnet wird. Er wird ausführlich mit verschiedenen synthetischen Zeitreihen und Fehlermodellen getestet und auf einen südafrikanischen Datensatz angewandt. Der Vergleich mit Methoden, die auf einer Spektralanalyse oder einem Maximum Likelihood Estimator beruhen zeigt, dass der relativ schnelle Algorithmus stabile und verlässliche Angaben liefert.

Zuletzt wird der entwickelte Algorithmus erweitert, um die Kovarianz der Geschwindigkeit zu erhalten. Die Anwendung auf verschiedene Datensätze an konvergenten Plattengrenzen, wo regelmäßig Kriechereignisse in Form von Slow Slip Events auftreten, zeigt für einige Stationen stark richtungsabhängige und räumlich korrelierte Geschwindigkeitsfehler. Des Weiteren konnte eine Zeitkorrelation beobachtet werden, die auf einen tektonischen Ursprung der Ereignisse hinweist. Die korrigierten Zeitreihen, von denen die modellierten Ereignisse subtrahiert wurden, haben dagegen richtungsunabhängig eine Zeitkorrelation, die etwa dem $1/f$ Rauschen entspricht, und weisen keine räumlich korrelierten stark exzentrischen Fehlerellipsen auf. Die Analyse ermöglicht somit eine qualitative Bewertung der Modelle zeitabhängiger Signale in GPS Zeitreihen.

Contents

Zusammenfassung	vii
Contents	x
1 Introduction	1
2 Strain rate patterns from dense GPS networks	5
2.1 Introduction	6
2.2 Methods	7
2.2.1 Strain rate analyses	7
2.2.2 Interpolation	8
2.3 Results	10
2.3.1 Geologic setting	11
2.3.2 Data	11
2.3.3 Strain rate tensor	13
2.3.4 Horizontal maximum shear strain rate	15
2.3.5 Dilatation rate	21
2.3.6 Co-seismic strain	23
2.4 Conclusions	23
2.5 Acknowledgments	27
3 Estimation of velocity uncertainties from GPS time series: Examples from the analysis of the South African TrigNet network	29
3.1 Introduction	30
3.2 Time correlated variance	32
3.3 Error model	35
3.3.1 Power law noise	36
3.3.2 White noise, flicker noise, and random walk	38
3.3.3 Seasonal effects	42

CONTENTS

3.3.4	Offsets and velocity changes	44
3.4	TrigNet	46
3.4.1	CATS vs AVR	48
3.5	Conclusion	54
3.6	Acknowledgments	57
4	Velocity Covariance of GPS Time Series in the Presence of Transients and Time Correlated Noise	59
4.1	Introduction	60
4.2	Directional noise analysis	61
4.3	Costa Rica	64
4.4	PANGA	72
4.5	Mount St. Helens	77
4.6	Acknowledgments	80
5	Conclusion and Outlook	81
	References	85
	Acknowledgments	99
	Curriculum Vitae	101

1

Introduction

The Global Positioning System (GPS) designed by the US Department of Defense for military and civilian navigation and positioning became fully operational in 1994. Since then it has become the method of choice for studying a variety of geophysical processes (e.g. Segall and Davis, 1997). The increasing number of continuously operating GPS receivers along with an improving precision of the position measurement provides the possibility to better and better study the motion of tectonic plates, crustal deformation at faults and volcanoes, and glacial isostatic adjustment. GPS is also used to contribute to atmospheric and ionospheric studies and measurements of sea level changes. Recent developments in high rate GPS indicate an increasing role of GPS in seismology (e.g. Larson, 2009).

Along with the availability of longer position time series and the increasing accuracy of the measurements GPS will become still more important in the study of time dependent transient tectonic signals, providing insights into processes such as earthquake cycles from which we can derive information on rheologic properties of the crust and asthenosphere. However, there are still several important aspects that need to be addressed. Among others, the following three points are important to understand the signal derived by geodetic measurements: (1) the derivation of continuous deformation patterns from point measurements without to have to specify the fault geometry, (2) the provision of realistic uncertainty estimates, and

(3) the separation of the signal from time correlated noise. Those points are addressed in the different parts of this thesis, which is structured in three main chapters that have been published in or are submitted to peer reviewed journals with myself as first author. Although not part of the thesis, the work developed for my dissertation has already been utilized by two other papers of which I am a co-author (Jiang *et al.*, 2012; Malservisi *et al.*, 2012).

Chapter 2 provides a method to obtain the full continuous 2d strain rate tensor from dense GPS networks. This work was motivated by the need to identify regions of strain accumulation in seismic hazard assessment. It has been partially funded by Munich Re and was published in *Natural Hazards and Earth System Sciences*. The presented method is designed to detect previously unknown structures, so it does not require any additional information like fault geometry. A comparison by the Southern California Earthquake Center (Sandwell *et al.*, 2010) of 16 methods to calculate strain rates showed that our algorithm is amongst the best performing and provides the most reliable results of all the methods that do not include fault geometries.

Additionally, this work showed that many GPS velocity fields exhibit significant transient signals. On the one hand these signals bias the results, if they are not modeled properly, on the other hand they provide important information about different geophysical properties. Although uncertainties were not introduced explicitly in the analysis, during the work for this chapter it became apparent that realistic GPS velocity uncertainty estimates are inevitable for any confidence estimates of models based on GPS data.

As a result, in Chapter 3 I adopted the Allan Variance that is commonly used in the estimation of oscillator stability and modified it in order to characterize the time correlated noise content in GPS time series. This work that provides realistic velocity uncertainty estimated in the presence of time correlated noise, has been published in the *Journal of Geophysical Research*. The algorithm is computationally cheap and has been tested thoroughly with synthetic time series and different error models. The calculations are done in the time domain, which makes it robust to gaps in time series. Additionally, the velocity uncertainty estimation is separated into two independent steps, which provides the possibility to independently test for an appropriate error model. The method has been applied to the South African TrigNet network and tested with an independent method

based on maximum likelihood estimation.

Finally, in Chapter 4 I enhanced the method to estimate the velocity uncertainty providing the full velocity covariance in the presence of time correlated noise that may vary in different directions. This work has been submitted to the *Geophysical Journal International* and provides realistic 2d GPS velocity confidence intervals. This analysis forms the basis for the study of transient signals in GPS time series that are caused by tectonic processes. So the analysis was applied to time series of GPS networks that are affected by transients. GPS sites in Costa Rica and Cascadia exhibit a highly time correlated signal in some preferred direction that can be explained by tectonic related transients like slow slip events or volcanic induced deformation. Models that account for these signals can independently be tested by analyzing the noise content of the residual time series.

2

Strain rate patterns from dense GPS networks

by *M. Hackl, R. Malservisi, and S. Wdowinski*

Published in Natural Hazards and Earth System Sciences, 2009, 9(4), 1177-1187

Abstract

The knowledge of the crustal strain rate tensor provides a description of geodynamic processes such as fault strain accumulation, which is an important parameter for seismic hazard assessment, as well as anthropogenic deformation. In the past two decades, the number of observations and the accuracy of satellite based geodetic measurements like GPS greatly increased, providing measured values of displacements and velocities of points. Here we present a method to obtain the full continuous strain rate tensor from dense GPS networks. The tensorial analysis provides different aspects of deformation, such as the maximum shear strain rate, including its direction, and the dilatation strain rate. These parameters are suitable to characterize the

mechanism of the current deformation. Using the velocity fields provided by SCEC and UNAVCO, we were able to localize major active faults in Southern California and to characterize them in terms of faulting mechanism. We also show that the large seismic events that occurred recently in the study region highly contaminate the measured velocity field that appears to be strongly affected by transient post-seismic deformation. Finally, we applied this method to co-seismic displacement data of two earthquakes in Iceland, showing that the strain fields derived by these data provide important information on the location and the focal mechanism of the ruptures.

2.1 Introduction

The 1994, $M_w = 6.7$ Northridge and the 1995, $M_w = 6.8$ Kobe earthquakes caused unprecedented damages of more than US\$40 billion and US\$100 billion, respectively. This was considerably more than could have been expected by earthquakes of comparable moment magnitude in California and Japan. These large damages were explained by the unexpectedly high magnitudes of these events for these particular areas (Smolka, 2007). These two events demonstrated in a dramatic way the shortcomings of traditional seismic hazard assessment, mainly based on probabilistic models derived from catalogs of regional seismicity and supplemented by additional geologic information only for known active faults (e.g. McGuire, 1993; Muir-Wood, 1993). In the case of Northridge, the rupturing fault was previously unknown without any surface expression and, hence, termed blind thrust fault. In Kobe the fault was assumed to be related to low seismic hazard.

The basic explanation for seismic activity is derived from the elastic rebound theory (Reid, 1910), suggesting that earthquakes are the result of a sudden release of elastic strain energy accumulated in a steadily deforming crust. Thus, seismic hazard assessment might be improved by detecting localized patterns of crustal deformation. Due to the development of satellite based positioning technologies, such as the Global Positioning System (GPS), it is nowadays possible to detect small displacements of the Earth's surface with sub-centimeter precision. These observations provide insights into crustal motion and deformation processes at new scales in both spatial density and accuracy. However, precise repeated positioning measurements provide only displacement information of a finite number of points. In order to derive local and regional deformation patterns, an analysis method needs to be applied.

Here we present a fast and economic method to identify deformation and strain rate patterns in Southern California from dense geodetic networks by using a simple interpolation scheme that requires only geodetic velocities as input. This method is independent of the local geologic setting, thus it can easily be applied wherever geodetic measurements are available, even if the local geology is not fully known. By interpolating the velocity component fields using splines in tension (Wessel and Bercovici, 1998), it is possible to detect major active faults as well as regions of high strain rate related to tectonic activity or human-induced deformation (i.e. oil and water pumping). We applied this method to data collected in Southern California, a tectonically active region between the North American and the Pacific plates. We also applied the method to data from regions experiencing post-seismic and co-seismic deformation, gaining information about transient behavior and rupture mechanisms.

Although strain rate is a good indicator of the deformation accumulated in a region, it does not directly correlate with the amount of elastic energy released by seismic events. Thus, it can only be a supportive, independent observation for regional seismic hazard estimation; additional information and models are required to fully quantify the amount of elastic energy stored in the area. Still, the results of this method can be utilized as a starting point for further numerical models and/or geological investigations to estimate current fault activities.

2.2 Methods

2.2.1 Strain rate analyses

Previous works used geodetic observations to quantify the regional strain rate pattern and the accumulating strain on faults. Here we provide a brief overview of the various methods; a full analysis and comparison of those works is out of the scope of this paper. Probably the most common method is based on a discretization of the investigated area into triangles (e.g. Delauney triangulation) and computation of internal strain rate for each triangle (see e.g. Frank, 1966; Shen *et al.*, 1996; Cai and Grafarend, 2007; Fernandes *et al.*, 2007; Wdowinski *et al.*, 2007). This method is very similar to the computation of stress and strain rate for each element in a finite element model, another way used to calculate a continuous strain field from geodetic data (Jimenez-Munt *et al.*, 2003). In general, these methods

do not have redundancy of data and hence can not detect and remove outliers. Furthermore they produce a continuous displacement field, but the obtained strain rate is discontinuous.

Other methods use inversion techniques to map the strain rate field. For example, Spakman and Nyst (2002) based their inversion on the technique of seismic tomography. They assign strain rate to a previously discretized area by using different paths of relative displacement between pairs of observation points. Haines *et al.* (1998), Kreemer *et al.* (2000), and Beavan and Haines (2001) used point observations of displacement observed by geodetic networks and strain evaluated by geologic and geophysical information (e.g. earthquake focal mechanisms) to invert for the Eulerian pole that locally minimizes the strain rate and velocity field residuals along a regional curvilinear reference system. As any inversion scheme these methods are computationally expensive. Furthermore, tomographic methods need to impose the location of faults so they can only be used to quantify the slip deficit on known structures, but not to identify unknown faults. In general, inversion based methods require assumptions on the constitutive law of the crust in order to relate the observed deformation to strain rate.

Interpolation of geodetic data can produce continuous strain rate fields suitable to identify new structures without having to assume anything about the deformation mechanisms. For this reason, different schemes have been suggested. Wdowinski *et al.* (2001) interpolated the velocity field along small circles relative to the pole of rotation that minimizes the residual (called pole of deformation). Allmendinger *et al.* (2007) used different approaches (nearest neighbor and distance weighted) to obtain continuous velocity fields from which a strain rate pattern can be calculated. Kahle *et al.* (2000) interpolated velocity fields in the Eastern Mediterranean by using a least-square collocation method based on a covariance function. Here we use a computationally cheap and fast spline interpolation of gridded data.

2.2.2 Interpolation

The principal aim of our method is to obtain a continuous strain rate field using only geodetic data. To do this, we performed a separate interpolation of the east and north velocity components on a regular grid using the splines in tension algorithm described by (Wessel and Bercovici, 1998). The tension is controlled by a factor T , where $T = 0$ leads to a minimum curvature (i.e. natural bicubic spline), while $T = 1$ leads to a maximum curvature, allowing for maxima and minima only at observation points. As long as the grid size

is not significantly smaller than the average site distribution, the results are not very sensitive to the choice of T . We set $T = 0.3$, the value suggested by Wessel and Bercovici (1998) for topographic interpolation. In order to perform the interpolation, the region is divided into a regular grid with cell size comparable to the average distance of geodetic sites. For cells with only one value, the observed value was assigned to the cell. Where a grid cell contained more than one observation, the median of all the included data was computed. Since the grid size is based on the average density of GPS sites, regions of denser datasets often need to be averaged. In spite of the loss of information, this has the advantage that outliers are removed and do not bias the results.

The interpolation will give two continuous scalar fields corresponding to the north and east components of the velocity. A basic assumption in this process is that the two components of the interseismic velocities are independent. Indeed, the correlation between the two fields is usually small and the error introduced by this assumption is smaller than the one associated with the interpolation scheme itself.

Since we use a spline interpolation function for the two components of the velocity fields, it is possible to calculate the derivatives along the local north and east directions, producing four continuous fields that can be linearly combined in a continuous representation of the strain rate tensor.

Assuming small deformations, the components of the strain rate tensor are defined as:

$$\dot{\epsilon}_{ij} = \frac{1}{2} \left(\frac{\partial v_i}{\partial x_j} + \frac{\partial v_j}{\partial x_i} \right) \quad (2.1)$$

where i, j substitute east and north.

In a similar way, it is possible to compute the antisymmetric rotation rate tensor:

$$\dot{\omega}_{ij} = \frac{1}{2} \left(\frac{\partial v_i}{\partial x_j} - \frac{\partial v_j}{\partial x_i} \right) \quad (2.2)$$

At this point, any tensorial analysis can be performed. The eigenspace analysis of the tensor is the starting point for the full description of deformation at every gridpoint, providing different aspects of the strain rate. The eigenvectors of the strain rate, for example, represent the direction of maximum and minimum strain rates, while their associated real eigenvalues λ_1 and λ_2 represent the magnitude (note that we follow the notation that positive values indicate extension and negative values stand for compression).

The maximum shear strain rate and its direction might provide a tool to identify active faults, since motion along faults is related to shear on

that structure. Faults oriented in this direction are the ones most likely to rupture in a seismic event. The maximum shear strain rate at every gridpoint can be obtained by a linear combination of the maximum and minimum eigenvalues:

$$\dot{\epsilon}_{\text{max_shear}} = \frac{\lambda_1 - \lambda_2}{2}, \quad (2.3)$$

while the direction of maximum shear is oriented 45° from the direction of the eigenvector corresponding to the largest eigenvalue:

$$\theta_{1,2} = \frac{1}{2} \arctan \left(\frac{2\dot{\epsilon}_{ij}}{\dot{\epsilon}_{ii} - \dot{\epsilon}_{jj}} \right) \pm 45^\circ \quad (2.4)$$

Note that Eqn. (2.4) corresponds to two conjugate perpendicular directions that cannot be distinguished without further constraints.

The trace of the tensor,

$$\delta = \dot{\epsilon}_{ii} + \dot{\epsilon}_{jj} \quad (2.5)$$

corresponds to the relative variation rate of surface area (dilatation) and thus can indicate regions of thrusting or normal faulting.

It is interesting to note that our method is not limited to the analysis of inter-seismic data. We also applied the method to co-seismic displacement vectors to obtain the associated strain field, which is useful for identifying rupture zones or even deducing earthquake focal mechanisms (see Section 2.3.6). If the studied velocity field is affected by post-seismic deformation, the method can be used to evaluate time dependent changes of the strain rate. It is interesting that the use of inter-seismic velocities not corrected by transient behavior contaminates the strain rate field in a way that can be used to obtain information about the rupture mechanism (see Section 2.3.5) and about the structure and rheological properties of the crust.

2.3 Results

In order to test the method, we chose to apply it to a region with a dense coverage of geodetic measurements and well known from a geologic, seismic, and geomorphologic point of view. For this reason, we chose to apply the method to observations in Southern California, because (1) it is one of the most extensively instrumented areas of the world, (2) it has high density of known active faulting, (3) it is well understood from a geological and geophysical point of view.

2.3.1 Geologic setting

Tectonics in Southern California are dominated by the right lateral transcurrent plate boundary between the North American (NA) and Pacific plates. The two plates have been grinding past each other for about 25-30 Myr, creating a broad deformation zone mainly composed of subparallel strike slip faults. This zone has been shifted several times before the current San Andreas Fault Zone developed about eight Myr ago (Atwater and Stock, 1988).

The present day relative motion between NA and the Pacific Plate is at first order right lateral with a total velocity of about 49 ± 3 mm/yr (e.g. Plattner *et al.*, 2007), oriented $\sim N 37^\circ W$. While in Central California $\sim 80\%$ of the motion is taken up by the San Andreas Fault (SAF) (Prescott *et al.*, 2001), in Southern California it is partitioned on different faults, of which the SAF, the San Jacinto Fault (SJF), and the Elsinore Fault (ELS) are the most prominent ones. These three faults account for about 80% of the relative motion (Bennett *et al.*, 1996). This fault system consists of multiple segments, whose interaction is still not completely understood. The remaining 20% of the slip are accommodated offshore and along different fault systems further east, like the Eastern California Shear Zone (ECSZ) and the Basin and Range area (Fig. 2.1). In the past two decades four earthquakes $M_w \geq 6.5$ occurred in the region, their location and focal mechanism¹ are also shown in Fig. 2.1.

2.3.2 Data

We used data provided mainly by two sources, the Southern California Earthquake Center (SCEC) (Shen *et al.*, 2003) and the Scripps Orbit and Permanent Array Center (SOPAC) (Jamason *et al.*, 2004). The SCEC dataset is composed of observations based on different geodetic techniques between 1970 and October 2001 (a full description is given by Shen *et al.* (2003)). The SOPAC dataset consists of continuous GPS measurements covering the time period from 1990 to 2008. It includes data provided by the Plate Boundary Observatory² (PBO). To better allow for constraints on areas along the border of our study region, we also included campaign observations from the Eastern California Shear Zone (ECSZ) and North-

¹from: USGS National Earthquake Information Center, <http://neic.usgs.gov/neis/sopar/>, accessed September 2008

²<http://pbweb.unavco.org/?pageid=88>

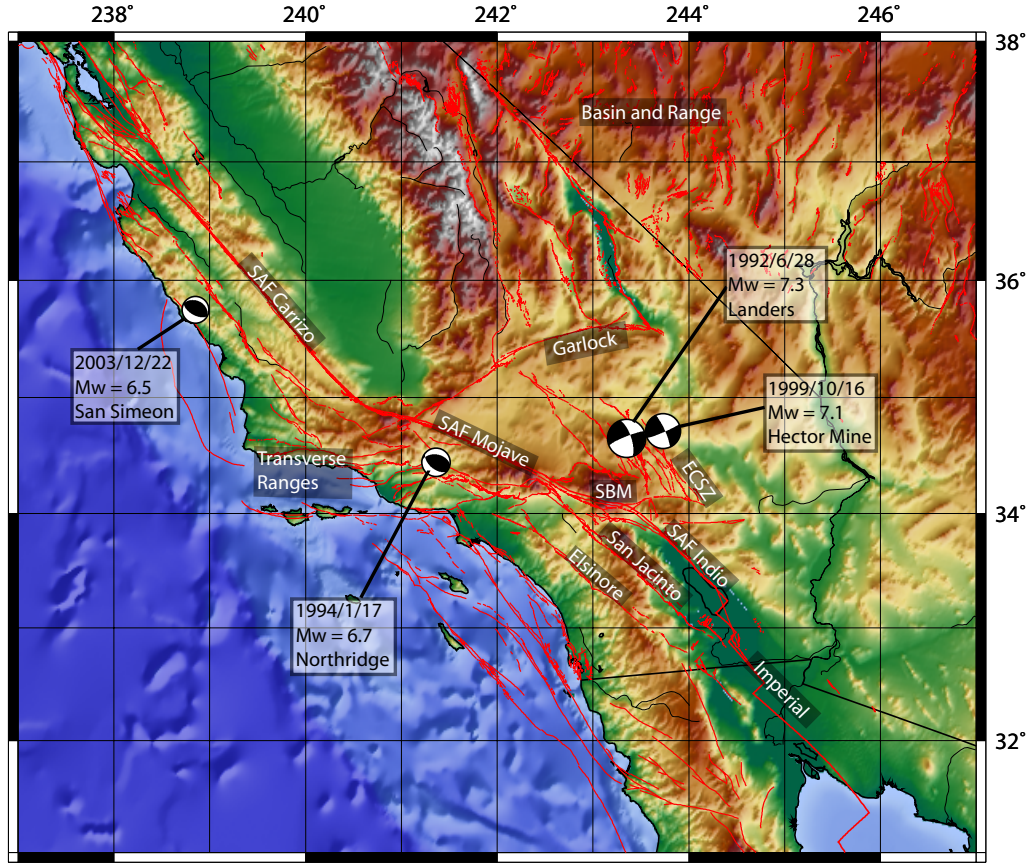


Figure 2.1: Topographic map of Southern California with major faults. Red lines indicate known faults and plate boundaries from: US Geological Survey and California Geological Survey, 2006, Quaternary fault and fold database for the United States, accessed September 2008, from USGS web site: <http://earthquakes.usgs.gov/regional/qfaults/> and Michaud *et al.* (2004). SAF: San Andreas Fault, SBM: San Bernadino Mountains, ECSZ: Eastern California Shear Zone. Focal mechanisms from USGS.

Table 2.1: Table of GPS velocity datasets used in the calculation.

Institution	Number of sites used	Sampling period
SCEC	769	1970–Oct 2001
SOPAC	991	1990–2008
UM	72	1994–2001

ern Baja California, Mexico, collected and processed by the University of Miami (UM) (Dixon *et al.*, 2002; Plattner *et al.*, 2007, and LaFemina, P., personal communication, 2008) (see Table 2.1). In order to merge the different datasets, the SOPAC and UM data were rotated into the SCEC North America fixed reference frame (RF), using the Eulerian pole that minimizes the residuals of the velocities at common sites (a list of common sites and residuals is given in the supplementary material of Hackl *et al.* (2009)).

The final dataset consisted of 1261 velocity vectors within the area of interest in Southern California and adjacent regions (see Fig. 2.2). Note, that all the data centers provided the velocities corrected for discontinuities in the time series (i.e. co-seismic, instrumentation changes, and transient effects), providing long term inter-seismic velocities. This means that the strain map obtained from the data should be a representation of the long term strain accumulation in the region.

2.3.3 Strain rate tensor

Based on the distribution of the GPS observations, we tested different grid sizes to identify the best resolution. Too fine grid size results in a highly irregular strain rate map with high strain rate peaks at observation sites. It would be possible to increase the tension T for the interpolation, but we noticed that such an interpolation introduces numerous artifacts. Too coarse grid size results in a very low and highly delocalized strain rate. The ideal situation would be to have a grid with at least one observation per cell. After different tests we found that a regular grid with cell size of 0.04° , is most suitable for the interpolation of the horizontal velocity field components for Southern California. Using GMT routines (Wessel and Smith, 1991), we calculated the strain rate tensor as described in Section 2.2.2. The script used to produce the results in this paper is attached in the electronic supplementary material in Hackl *et al.* (2009). Fig. 2.3 shows the three components of the strain rate tensor. In order to avoid over-interpreting artifacts due

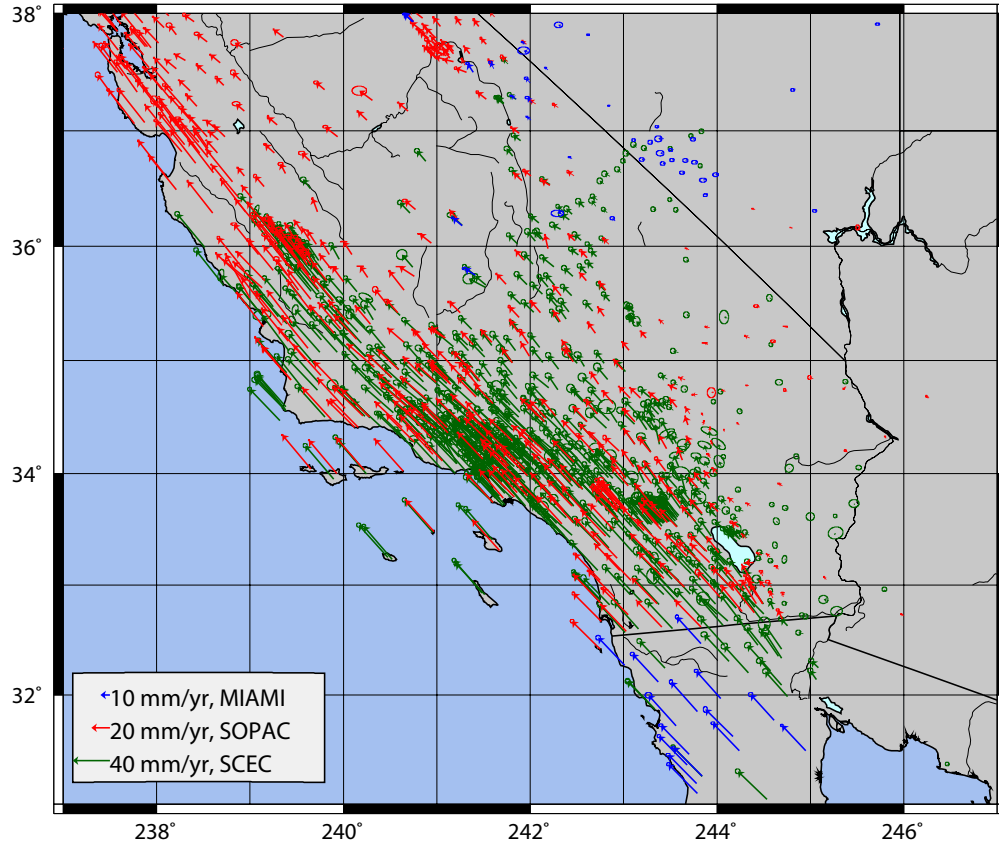


Figure 2.2: Map of Southern California with velocity arrows used in this study in a fixed North America reference frame. Red arrows: velocity provided by the Scripps Orbit and Permanent Array Center (SOPAC); blue arrows: data from the University of Miami; green arrows: data from the crustal motion map (version 3) by the Southern California Earthquake Center (SCEC).

to the interpolation scheme, we masked out (white color) interpolated values located at distances greater than $\sim 0.5^\circ$ (15 grid cell) from the closest observation site in all the figures.

This method is not suitable to calculate absolute values of strain rates. Since this value is related to the gradient of the velocity field, the rate is limited by the grid size, the minimal distance along which it is possible to observe a velocity change. This is a shortcoming of the introduced method, because the absolute values of the strain rate are limited by this fact and might hence be underestimated. Smaller grid sizes could overcome this problem, but they are associated with increasing uncertainties. However, the method is suitable to determine relative strain and strain rate changes quite well.

2.3.4 Horizontal maximum shear strain rate

The plate boundary in Southern California is mainly of transcurrent nature. Thus, the direction and magnitude of the maximum shear strain rate are good scalar fields to represent the strain rate tensor. These two parameters are suitable to characterize the amount of localization of the shear deformation and the direction along which strike slip faulting is more favorable. In Fig. 2.4, the color scale indicates the magnitude of the maximum shear strain rate, while the crosses indicate the two conjugate maximum shear directions. At first glance, the image shows a very high similarity with the seismic hazards maps published by USGS³. This is essentially due to the fact that the “warm” color regions in Fig. 2.4 clearly reflect the location of the principal plate boundary between North America and the Pacific, following the trace of the SAF. The maximum shear strain rate is highest in the south along the Imperial Fault and along the central section of the SAF (north of the Carrizo Segment). This can partially be a consequence of the fact that in these regions the fault system is less complex, thus the deformation can better localize along the major segments of the fault. Probably, the high shear strain rates are related to the local aseismic creep of those segments of the SAF system. Creeping faults release part of the relative motion between the two sides by aseismic slip, implying that a large part of the deformation is accommodated on the fault plane in a really narrow region with very high shear strain rates. These do not necessarily correspond to high seismic hazard, since large parts of the deformation is not accumulated as elastic

³see e.g.: <http://earthquake.usgs.gov/hazards/products/>

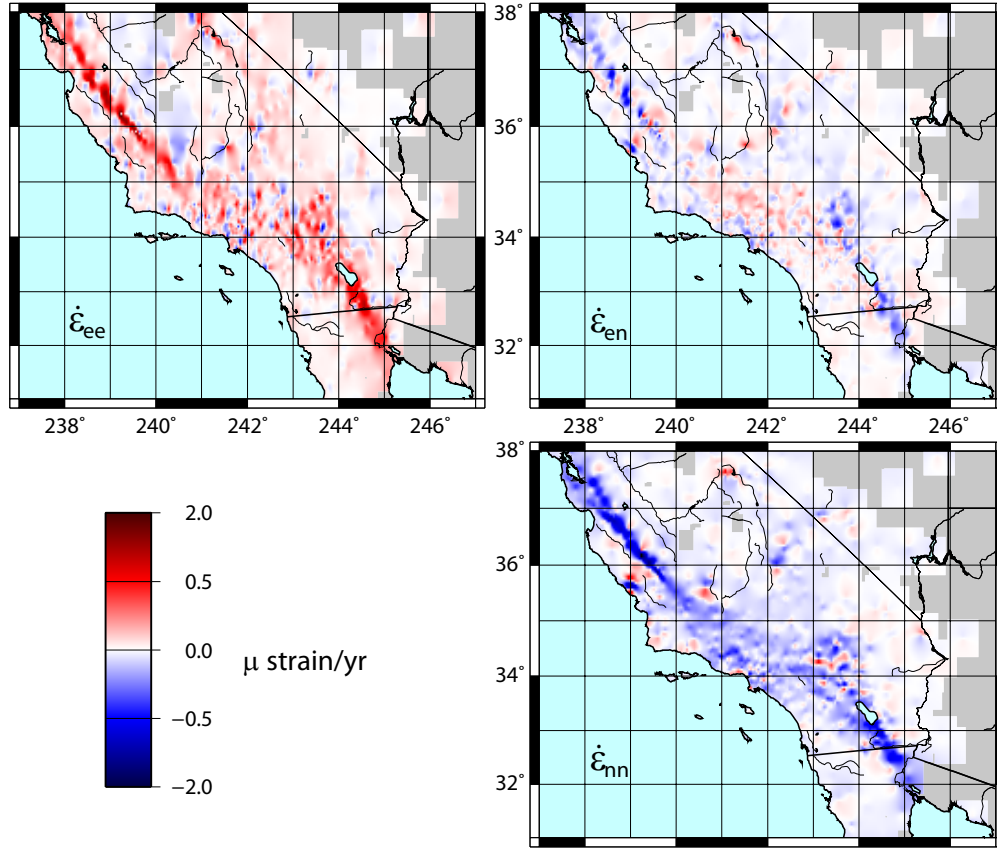


Figure 2.3: Continuous symmetric strain rate tensor components obtained by summing the directional derivatives of the previously interpolated continuous velocity component fields (see Eqn. 2.1). Each panel corresponds to one of the three components of the strain rate tensor as indicated in each figure. Calculated values at a distance greater than $\sim 0.5^\circ$ (15 cells) from any observation site are masked out.

energy (Bürgmann *et al.*, 2001; Malservisi *et al.*, 2005). Central Southern California is dominated by a more complex structure of slip partitioning, which is also reflected in broader zones of relatively high shear strain rates, extending from the ECSZ to the Transverse Ranges.

At the transition between the Transverse Range region and the Imperial Valley, the map clearly shows that the maximum shear strain rate is partitioned between the SAF and SJF, with a minor contribution at the Elsinore Fault. The secondary plate boundary along the ECSZ/Walker Lane is also clearly visible. This plate boundary separates the Sierra Nevada Block from the Basin and Range and accounts for about 11 mm/yr of relative motion (Dixon *et al.*, 2000). The map shows relatively high shear strain rates in the Owens Valley region and at the south eastern part of the Mojave Region (probably due to recent large seismic events in the region). The Great Valley, which is characterized by low strain rates in the map, is essentially rigid and almost no deformation is observed. Within the Great Valley some deformation is observed at latitude $\sim 35.5^\circ$ N. Although it might be related to artifacts due to the lack of data, it is interesting to note that this region is intensively used for oil extraction. Wdowinski *et al.* (2007) already suggested that anomalous signals there may reflect data contamination by oilfield operations near Bakersfield. The two regions of deformation are also clearly visible as large subsiding areas in regional InSAR studies (Amelung, F., personal comm., 2008).

Apart from creeping fault regions, locations of past large seismic events appear on the map as particularly bright spots. This is notable for the location of the Landers (1992, $M_w = 7.3$), Hector Mine (1999, $M_w = 7.1$), and San Simeon (2003, $M_w = 6.6$) earthquakes. Apart from these recent events, also large earthquakes that happened before the start of the data acquisition seem to be apparent in the dataset. In particular, there are bright spot at the location of the 1872 (Intensity XI) Owens Valley and 1993 Eureka Valley ($M_w = 6.1$) events. Since the velocities have been corrected for co-seismic displacements and for short term post-seismic deformations, it is likely that the observed high shear strain rates are related to visco-elastic relaxation. According to visco-elastic models (e.g. Savage and Lisowski, 1998), the surface velocity at a locked fault is highest right after an earthquake and decreases with time at a rate controlled by the local rheology. This transient behavior does not only explain why regions of recent seismic events appear much brighter, but also the relatively low rates at the SAF Mojave, the Transverse Range, and the Elsinore Fault, which have not experienced

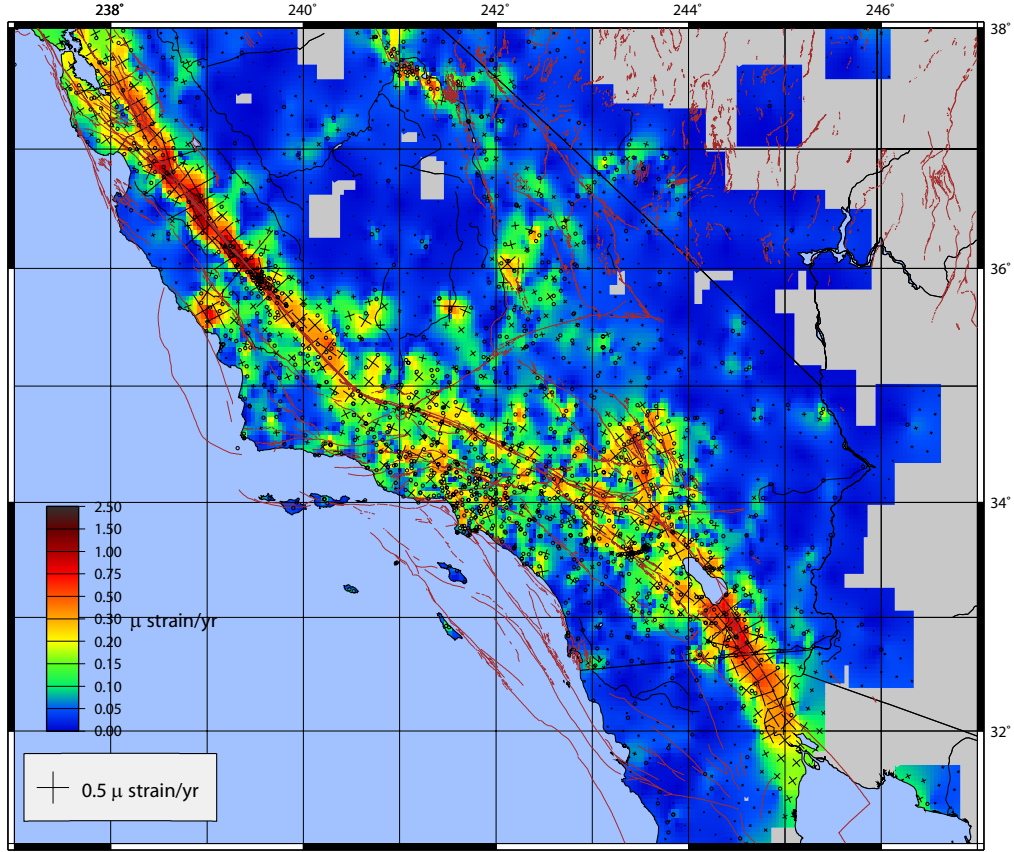


Figure 2.4: Map of Southern California with magnitude (see colorbar) and direction (and its perpendicular, see black crosses) of maximum shear strain rates. The size of the crosses is proportional to the magnitude of the maximum shear strain rate. Locations of observation sites are indicated by black circles and known faults (see Fig. 2.1) by brown lines. Values at a distance greater than 15 grid cells from any observation site are masked out.

large seismic events in the past century and are supposed to be late in their earthquake cycles.

In order to test the interpolation and to analyze transient behavior, we performed separate analyses of the data from SCEC and SOPAC. As shown in Table 2.1, the two datasets include observations from different time spans (Fig. 2.5). In particular, the inclusion of data released by PBO within the SOPAC dataset allows for studying a more recent velocity field. A visual inspection of the two figures shows that it is not possible to do a full comparison of the two strain rate fields. The interpolation method is particular sensitive to site density, as high strain rates are directly related to big velocity changes within a narrow region. This becomes apparent in places like the Los Angeles Basin, where the SCEC dataset is much denser than the SOPAC one. The method is also sensitive to the smoothing of the fields at the boundaries, as shown, for example, at the northern end of the SAF and at the Imperial fault. Thus, it is crucial to include observations for regions outside the one of interest (here: the inclusion of the data from UM or PBO data outside Southern California) in order to reduce possible artifacts caused by edge smoothing.

Nevertheless, we note a considerable change of the maximum shear strain rate between the maps in Fig. 2.5 in regions with comparable data distribution like the San Simeon area or the Landers/Hector Mine region. In the San Simeon region, the bright spot is present only in the SOPAC field. Since the 2003 earthquake happened after the release of the SCEC CMM v3 velocity field that was utilized here. The absence of the signal in the old strain rate field clearly indicates that the high shear is not associated with fault loading, but with post-seismic relaxation (see Fig. 2.6).

In a similar way, we can observe that, despite the similar coverage of geodetic observations, the maximum shear strain rate in the Landers/Hector Mine area is situated closer to the location of the Landers event for the SCEC data, and closer to the Hector Mine event for the SOPAC data. We relate this location shift of the maximum shear strain rate to the time span of the data collection in the two datasets. The post-seismic relaxation due to the 1992 Landers earthquake is clearly visible in the shear strain rate calculated using SCEC data only (see Fig. 2.5, A), whereas the high strain rates are probably related to post-seismic effects of the 1999 Hector Mine and the 2003 $M_w = 6.5$ San Simeon events, which show up in Fig. 2.5 (B). Unfortunately, a similar analysis was not possible for the Owens Valley and Eureka Valley events, since the signal is mainly derived from episodic GPS observations conducted by the UM group and cannot be divided into

2 STRAIN RATE PATTERNS FROM DENSE GPS NETWORKS

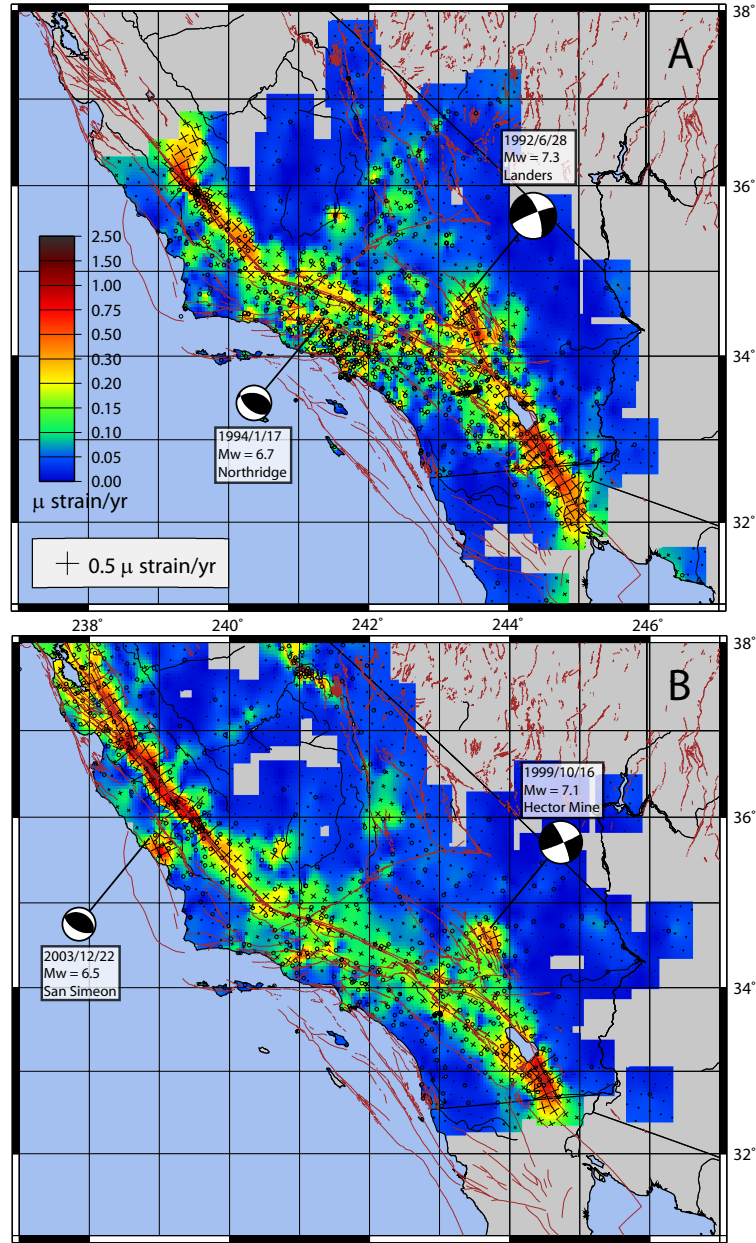


Figure 2.5: Same as Fig. 2.4 using subsets of the data. (A) Map of the maximum shear strain rate based only on velocity data of SCEC collected between 1970 and October 2001. (B) Map of the maximum shear strain rate using data from SOPAC spanning the period from 1990 up to September 2008. Values at a distance greater than 15 grid cells from any observation site are masked out. Brown lines indicate known faults (see Fig. 2.1).

different observation periods. A full study of the time series of the single GPS observations and the variation of the velocities with time is necessary to further investigate time dependent changes in the strain rate fields. Still, the comparison of the two strain rate fields shows that the method is also suitable for studying transient strain rates.

To conclude, the direction of maximum shear strain rate, indicated by the crosses in Figures 2.4 and 2.5, is mainly controlled by the direction of the SAF and is mainly parallel to the fault traces. While parts of the SAF show a partial rotation of the maximum shear strain rate direction along the Transverse Range, this is not the case in the Los Angeles basin, where the direction of the maximum shear strain rate does not appear to be oriented along the SAF. Probably, this is due to the fact that this region is controlled by thrust faulting and the current analysis of the strain rate does not allow for the full study of the three-dimensional tensor.

2.3.5 Dilatation rate

As a second example of the strain rate tensor analysis, we look at its trace. The sum of the diagonal elements of the tensor gives the rate of relative change of area (volume in 3-D) and provides the possibility to identify regions of compression or extension. Fig. 2.6 shows an example of this analysis using only SOPAC data in the region of the San Simeon earthquake. As previously mentioned, the velocity field in this area is strongly influenced by post-seismic visco-elastic relaxation and/or afterslip induced by the 2003 event. Indeed, the map of dilatation rate in the earthquake region reproduces the pattern of compression and extension of the published focal mechanism¹. The highly localized dilatation pattern suggests that afterslip and not a broad-scale visco-elastic relaxation is the dominant post-seismic mechanism. A dilatation rate pattern similar to the focal mechanism was also obtained for the Hector Mine earthquake. Using SCEC data only, we obtained a more complex dilatation rate pattern from post-seismic deformation of the Landers event, which coincides quite well with Coulomb stress data modeled by King *et al.* (1994). The obtained patterns show the strength of the introduced method in the analysis of the transient behavior of the strain rate and that the local velocity field is highly influenced by transient deformation probably induced by earthquake cycle effects.

At the northern end of the SAF in Fig. 2.6, we see that the dilatation rate shows a complex pattern. It is possible that this pattern reflects an artifact of the analysis. But it is worthy to note that this region corresponds to

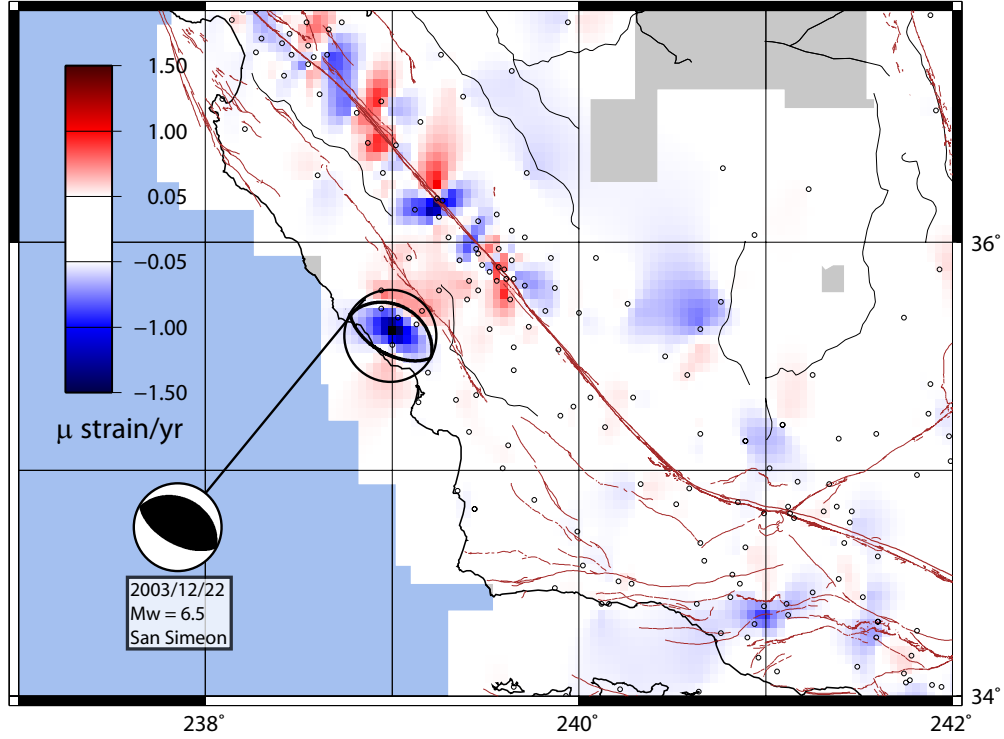


Figure 2.6: Continuous dilatation rate field (see colorbar) of western central California calculated from inter-seismic velocities, where negative values indicate compression and positive values extension. Black circles indicate site positions and brown lines known faults (see Fig. 2.1). Values at a distance greater than 15 grid cells from any observation site are masked out. The dilatation pattern reflects the focal mechanism of the San Simeon $M_w = 6.5$ earthquake on December 22nd, 2003 (from USGS¹). The high dilatation rates along the SAF are probably caused by creeping segments.

the transition between creeping and locked parts of the SAF and that the regional deformation may be influenced by the local pattern of creep and transient deformation (Nadeau and Guilhem, 2009). Furthermore, this is also the location of the 2004 Parkfield $M_w = 6.0$ earthquake, which influences the local strain rate. A more detailed analysis of this pattern is beyond the scope of this work.

2.3.6 Co-seismic strain

As a last example, we applied our method to a static displacement field instead of velocity data. The same interpolation method can be used to analyze a displacement field and results in strain instead of strain rate. It provides insights into the co-seismic deformation, slip location, and rupture characteristics. We applied the method to the two $M_w = 6.5$ and $M_w = 6.4$ earthquakes on 17 and 21 June, 2000 in the South Iceland seismic zone, analyzing the displacement of 50 sites in South Western Iceland (Árnadóttir *et al.*, 2001) (see Fig. 2.7). As expected by the strike slip nature of the two events, the rupture zones appear very clearly in a map of the maximum shear strain. The two bright spots in the map coincide with the location of the aftershocks recorded in the two weeks after the events⁴. Furthermore, the direction of the high shear zone is in good agreement with one of the planes of the focal mechanisms¹. This suggests that the interpolation can clearly identify the region of the rupture.

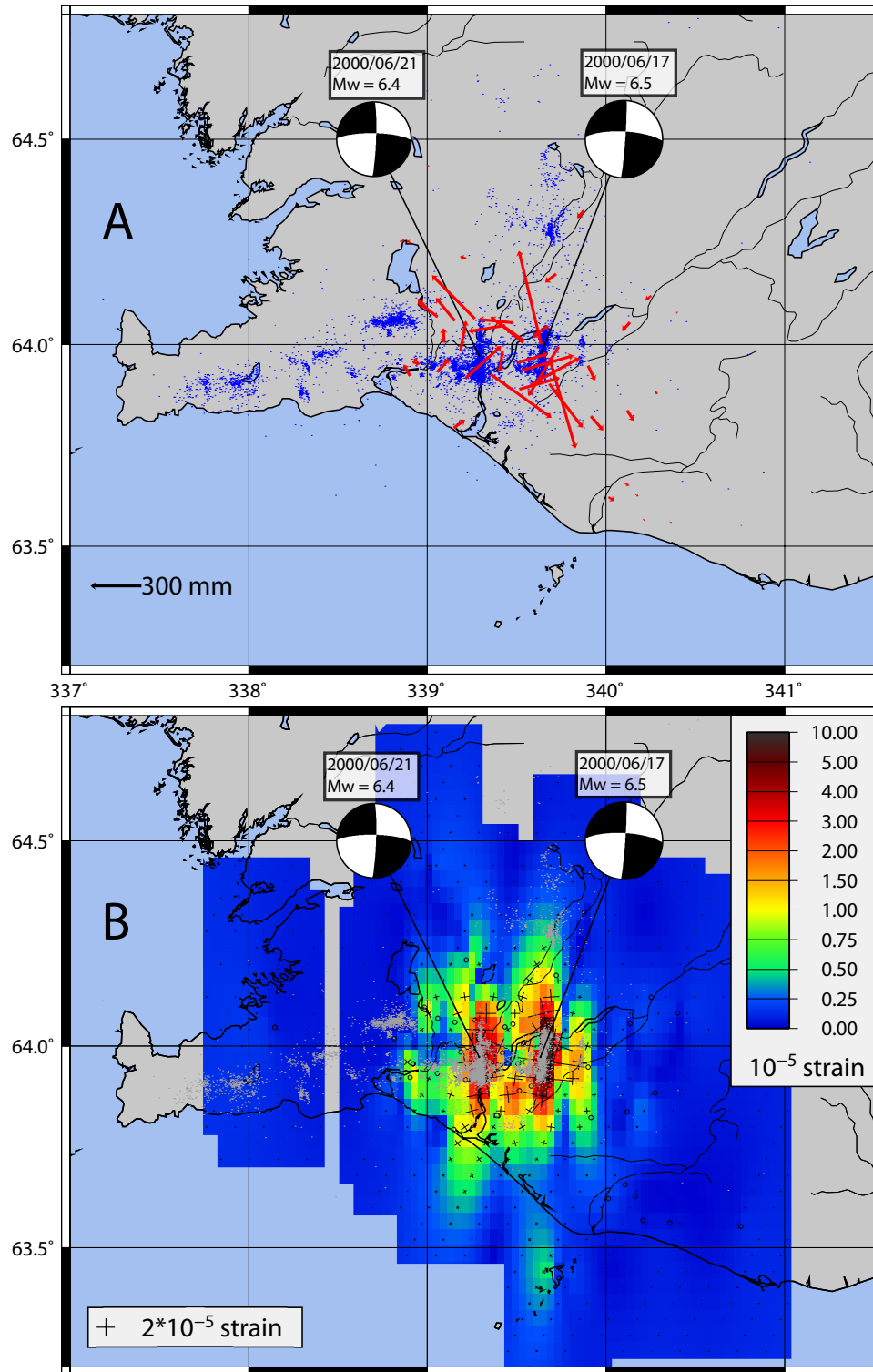
The dilatation analysis shows that the far field has a very good agreement with the observed focal mechanism. The region between the two faults is clearly influenced by both events presenting a more complex pattern than the one expected by the focal mechanisms. However, our geodesy based analysis can provide independent information for resolving the rupture plain ambiguity of the focal mechanism solution.

2.4 Conclusions

Given the importance of strain accumulation on the earthquake cycle, the study of regional strain rate is crucial for any seismic hazard assessment. Interpolation methods, as the one presented here, allow a derivation of the

⁴from: Icelandic Meteorological Office, <http://hraun.vedur.is/ja/englishweb/earthquakes.html>, accessed September 2008

2 STRAIN RATE PATTERNS FROM DENSE GPS NETWORKS



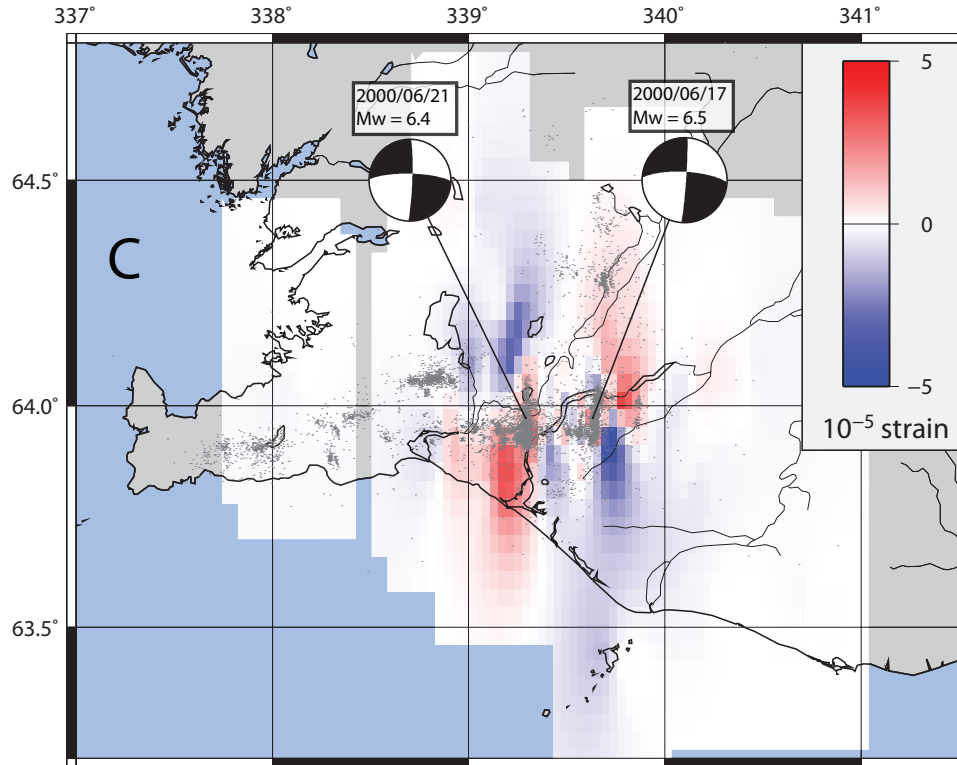


Figure 2.7: Coseismic displacement (**A**), shear strain (**B**), and dilatation (**C**) caused by the two strike slip events on 17 June and 21 June, 2000 in the South Iceland seismic zone. Focal mechanisms from USGS¹. Dots indicate seismic events in the period from 15 to 30 June, 2000 (from: Icelandic Meteorological Office⁴). The shear strain reflects the position and direction of the ruptures, while the dilatation coincides with focal mechanisms.

full tensor of strain rate from dense geodetic networks without the necessity to include any assumptions on the deformation mechanisms.

The analysis of the Southern California GPS data clearly shows that the method is capable to identify major regions of deformation. In particular, it indicates the importance of “secondary” plate boundaries like the Eastern California Shear Zone or the San Jacinto fault as regions of localized deformation. This suggests the importance of studying the full diffuse boundary between the NA and Pacific plates in the analysis of deformation patterns. An analysis of the maximum shear strain rate indicates that, apart from the LA basin, the direction of maximum shear is mainly controlled by the orientation of the SAF.

The strain rate map of Southern California also indicates a strong influence of transient effects. In particular, high strain rates are associated with regions of creeping, where the deformation is strongly localized close to the fault plane, and with regions affected by post-seismic deformation. Our analysis of the SCEC and SOPAC data for Southern California clearly demonstrates that the post-seismic deformation associated with past events is a strong component of the velocity field. An analysis of the evolution of the strain rate field is possible through the use of velocities derived from different periods. This analysis would provide important insight into the post-seismic mechanism and rheological properties of the crust and the asthenosphere. The presence of localized strain rate associated with seismic events that did not happen recently, like the Owens Valley or Landers earthquakes, indicates that the visco-elastic relaxation (e.g. Savage and Lisowski, 1998) has a strong impact on the observed geodetic field. This transient behavior can create a major challenge in the seismic hazard assessment. Current low strain rates at active faults cannot directly be related to low seismic hazard. At the contrary, the associated low strain rates can be an indication that the fault is late in its earthquake cycle, thus the rupture probability might be particularly high. On the other hand, bright spots in a strain rate map associated with faults that recently experienced earthquakes could be related to a current low seismic hazard. Similarly, the high strain rates at creeping sections of a fault can be associated to low seismic hazard. Thus, the strain rate map can contribute to seismic hazard assessment through the identification of regions of localized deformation, but numerical modeling of the full lithospheric behavior, the seismic history, and geological studies of the single faults are necessary in order to fully quantify the amount of elastic energy accumulated. Still, geodetically derived strain rate maps produce important geometric and regional constraints necessary for a

correct modelling of the faults in the area. This analysis can also provide important information regarding the regions where more geological studies are necessary.

Finally, we would like to point out that the interpolation of geodetic data should not be limited to the study of velocity fields and associated strain rates, but can also be applied to other fields like co-seismic displacement data. For example, the analysis of the co-seismic strain derived from the observed displacements during the June 2000 earthquakes in Iceland indicates that the obtained strain tensor provides important insights into the location and direction of the events as well as information about the rupture.

2.5 Acknowledgments

We acknowledge the Southern California Integrated GPS Network and its sponsors, the W. M. Keck Foundation, NASA, NSF, USGS, SCEC and SOPAC, PBO (UNAVCO) for providing data used in this study. We are grateful to Marleen Nyst and an anonymous reviewer for their careful reviews and Roland Bürgmann and Christian Sippl for their comments. Thanks to the Icelandic Meteorological Office and Thóra Árnadóttir for the Icelandic data. This research was possible for the support of Munich Re and was partially funded by the DFG grant MA4163/1-1.

3

Estimation of velocity uncertainties from GPS time series: Examples from the analysis of the South African TrigNet network

by M. Hackl, R. Malservisi, U. Hugentobler, and R. Wonnacott
Published in Journal of Geophysical Research, 2011, 116(B11404)

Abstract

We present a method to derive velocity uncertainties from GPS position time series that are affected by time correlated noise. This method is based on the Allan variance, which is widely used in the estimation of oscillator stability and neither requires spectral analysis nor Maximum Likelihood Estimation (MLE). The Allan variance of the rate (AVR) is calculated in the time domain and hence is not too sensitive to gaps in the time series. We derived analytical expressions of the AVR for different kinds of noises

like power law noise, white noise, flicker noise, random walk, and found an expression for the variance produced by an annual signal. These functional relations form the basis of error models that have to be fitted to the AVR in order to estimate the velocity uncertainty. Finally we applied the method to the South Africa GPS network TrigNet. Most time series show noise characteristics that can be modelled by a power law noise plus an annual signal. The method is computationally very cheap and the results are in good agreement with the ones obtained by methods based on MLE.

3.1 Introduction

Satellite based geodetic techniques provide an outstanding tool to measure crustal motions and deformations. Geodetically derived velocities of surface points provide necessary constraints to study tectonic plate motion, strain localization of active geological features, and to estimate rheological properties of the crust and the underlying asthenosphere (e.g. Dixon, 1991). In general, geodetic velocities and their uncertainties are indirectly derived through repeated position measurements of given points.

The measured relative position $x(t)$ of the point is the result of antenna motion and noise $\varepsilon(t)$. Any contribution to the measured antenna position is either modelled or considered to be noise. In geodynamics and tectonics the constant long term (inter-seismic) rate is usually of major interest. Unfortunately, a constant long term signal is not the only contribution to the antenna motion. Sudden (e.g. offset due to antenna changes or co-seismic displacement), periodic (e.g. annual or semiannual seasonal deformations), or transient (e.g. post-seismic deformation) signals are typically present in position time series. Some of the deviations from the long term linear motion due to these contributions can be modelled and subtracted in order to improve the measured velocity of the observed point (Segall, 2010). Still, the “corrected” time series remain affected by multiple sources of noise that cannot be completely removed from the signal (e.g. atmospheric delays, clock instability, monument motion, orbit error, etc.).

Johnson and Agnew (1995), Zhang *et al.* (1997), Mao *et al.* (1999), and Williams *et al.* (2004) showed that GPS velocity uncertainties are underestimated by factors from 2 to 11, if only white noise (not time correlated noise) is considered. This suggests that time correlated noise has to be taken into account in the calculation of velocity uncertainties.

Mao *et al.* (1999) presented an error model that includes colored (time correlated) noise. Their empirical formula is based on spectral analysis and Maximum Likelihood Estimation (MLE) of 23 globally distributed GPS stations with three years of data and takes into account flicker noise and random walk.

Williams (2003b) also presented an empirical method to derive velocity uncertainties, followed by the presentation of CATS, a software package for the analysis of time series (Williams, 2008). CATS can be used to perform a thorough time series analysis based on MLE for a variety of error models. A full analysis of the colored noise included in the time series through MLE is computationally expensive (depending on the error model up to $\mathcal{O}(n^3)$, for a time series of length n). Bos *et al.* (2008) presented an MLE approach that reduced the number of computations significantly ($\mathcal{O}(n^2)$ for a power law plus white noise error model), if there are no gaps in the time series. However, many published GPS velocity uncertainties are still computed assuming pure white noise or scaling the white noise by some empirical value derived from the repeatability of the time series (e.g. Dixon *et al.*, 2000). Only in a few cases is time correlated noise included, in general through the use of some empirical formula that does not require a full analysis of the time series (e.g. Mao *et al.*, 1999). Still these methods can lead to both large overestimation and underestimation of the correct velocity uncertainty.

There has been some debate on the choice of the error model and whether a random walk signal, mainly due to monument motion, is present in geodetic data or not. Continuous strainmeter and tiltmeter measurements at the Ida and Cecil Green Piñon Flat Observatory show a power law process close to random walk (Wyatt, 1982, 1989). This is in agreement with geodimeter and trilateration measurements (Langbein *et al.*, 1987; Langbein and Johnson, 1997). However, the analyses of Zhang *et al.* (1997) and Mao *et al.* (1999) suggest that flicker noise is the prevalent signal in GPS time series and random walk plays a secondary role. A comprehensive analysis of Southern California and South Nevada GPS sites by Langbein (2004, 2008) using MLE reveals that the time series are characterized by either flicker noise, random walk, general power law noise, or a combination of them and only in a few cases are these noises more complex including band-pass-filtered noise, first-order Gauss-Markov processes, or broadband seasonal noise. Recent studies by Hill *et al.* (2009) and King and Williams (2009) on short baselines, however, suggest that monument stability is not a dominant error source. Santamaría-Gómez *et al.* (2011) favor an error model consisting of white noise plus a power law noise, which is close to flicker noise for many

sites. This is also in agreement with Hill *et al.* (2009) and King and Williams (2009).

However, it is very difficult to distinguish between time correlated noise and velocity variations from transient phenomena (like post seismic deformation). For example Hackl *et al.* (2009) showed that the long term inter-seismic velocity field in Southern California (active plate boundary) can be affected by seismic cycle effects, which could explain a trend towards higher time correlation nearby active tectonic features.

Here we present a method to estimate GPS velocity uncertainties. In contrast to the different scaling methods, our method accounts for site characteristics but does not require spectral analysis nor MLE. It is based on the Allan Variance, an analysis often used as a measurement of frequency stability in clocks and oscillators (Allan, 1966; Barnes, 1966; Rutman, 1978) and it is applied to the slope of the time series. As the calculation is done in the time domain, the method is not too sensitive to gaps in the data and it is computationally cheap. The method provides the variance of the rate as a function of the considered time span (up to $\sim 1/4$ of the total time series length) without any assumption of the noise characteristics. The method is an extension of the one suggested by Caporali (2003) to estimate the stability of time series as a function of time. It is tested with synthetic time series and finally applied to the South Africa GPS network TrigNet, a network almost not affected by tectonic deformation.

3.2 Time correlated variance

Like many geophysical phenomena, noise in GPS position time series can be described as a power law process (Mandelbrot, 1983; Agnew, 1992). This one-dimensional stochastic process $\varepsilon(t)$ is characterized by a power spectrum of the form

$$P_x(f) = P_0 \left(\frac{f}{f_0} \right)^\nu, \quad (3.1)$$

where f is the temporal frequency, P_0 and f_0 are normalizing constants, and ν is the spectral index (Mandelbrot and Van Ness, 1968). White noise corresponds to $\nu = 0$, flicker noise to $\nu = -1$, random walk to $\nu = -2$. There are many ways to deal with time correlated noise mostly based on spectral analyses (e.g. Lomb, 1976; Scargle, 1982) or on MLE (e.g. Williams, 2008; Bos *et al.*, 2008). Another way to deal with time correlated noise was

developed to calculate clock uncertainties and is called Allan variance or two-sample variance (Allan, 1966; Barnes, 1966; Rutman, 1978). It is defined as one half of the average of the squared differences between consecutive readings of the observable sampled over a certain interval τ (Eqn. 3.2).

$$\sigma^2(\tau) = \frac{1}{2(n-1)} \sum_i (m_{i+1}(\tau) - m_i(\tau))^2 \quad (3.2)$$

where τ is the bin length, n the number of bins, and $m_i(\tau)$ the mean of the observable in the i -th bin.

The variance computed in this way is a function of the distribution being measured and the sample period. For stationary processes ($\nu > -1$) this variance is identical to the classical variance and thus it can be identified with the variance of the observable (Allan, 1966). In the case of non-stationary processes the Allan variance for a certain bin length is independent of the time series length and the sampling frequency. Thus, the Allan variance is convergent in contrast to the classical variance. Although the meaning of a variance is questionable in the case of non-stationary processes the Allan variance still provides insights into the noise characteristics in those cases (Allan, 1987).

The Allan variance has already been applied to geodetic time series to study uncertainties associated with site positions (Le Bail, 2004). Here, the Allan variance has been modified in the sense that the mean of each bin is replaced by its slope. To avoid confusion we will call the variance computed in this way Allan variance of the rate (AVR). In simple terms, the time series is divided into n bins of equal length τ . Then the slope of the time series is calculated for every bin by linear regression. The AVR corresponding to a given τ is then defined as one half of the variance of the differences of the slopes of two consecutive bins. Fig. 3.1 shows a synthetic time series and the corresponding AVR that is displayed in a log-log plot as a function of the bin length τ . The statistical significance of the AVR depends on the number of bin pairs used in the computation. In tests with synthetic time series reasonable results were obtained down to four bin pairs. The necessity of at least four bins to compute a statistical significant variance limits the maximum time span for which the variance can be directly computed to $\sim 1/4$ of the total length of the time series. The statistics of the AVR can be significantly improved at the expense of computational time for computing the AVR for overlapping bins (e.g. Howe *et al.*, 1981). This requires more calculation steps, but provides better results in terms of statistical significance. The variance associated to the full series needs to

3 ESTIMATION OF VELOCITY UNCERTAINTIES FROM GPS TIME SERIES: EXAMPLES FROM THE ANALYSIS OF THE SOUTH AFRICAN TRIGNET NETWORK

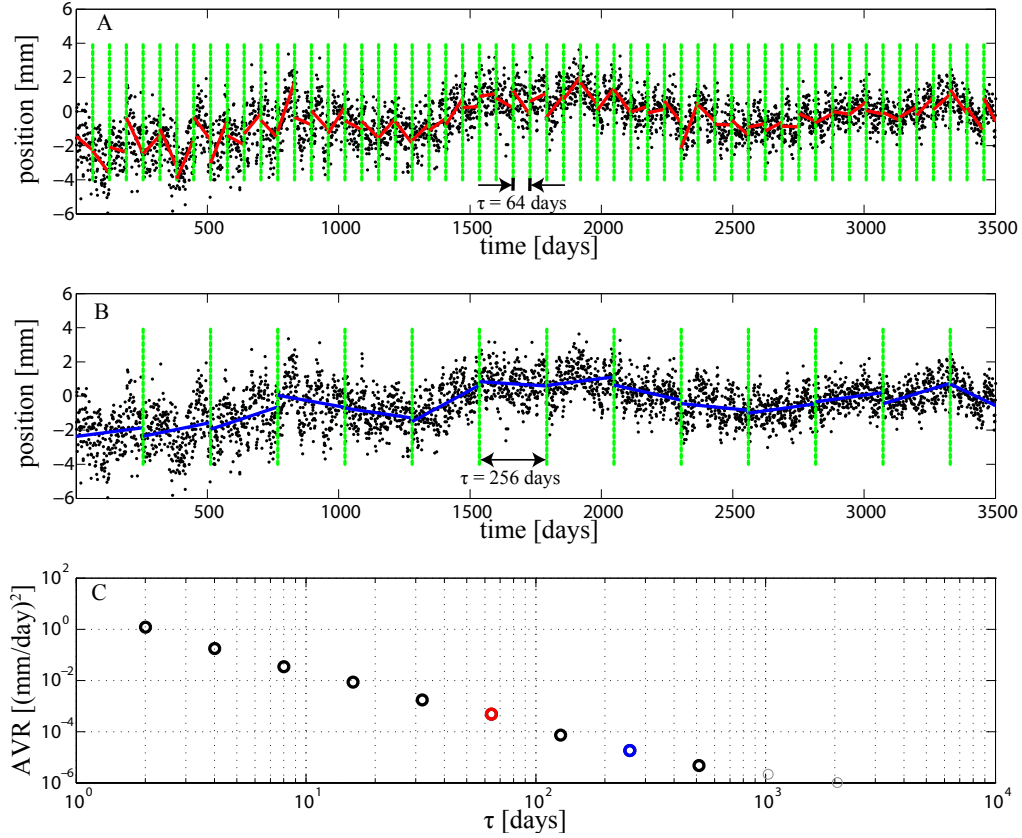


Figure 3.1: Synthetic time series (*A,B*) and corresponding AVR (*C*). The time series is divided in n bins of length τ and the slope of each bin is calculated by linear regression (red and blue lines in *A*, *B*). The AVR is calculated using Eqn. 3.2. The red circle at $\tau = 64$ days corresponds to the bins shown in *A*, the blue circle at $\tau = 256$ days corresponds to the bins shown in *B*. The light grey circles in the AVR are based on less than four bin pairs, hence they are statistically poorly constrained and should not be included in the fit of an error model.

be extrapolated assuming an error model. Still the AVR provides a visual representation of the improvement of the velocity uncertainty with increasing time length independently from the selected error model.

Gaps in the time series do not dramatically affect the calculation of the AVR. We tested the method with synthetic time series where gaps were created removing up to 50% of the points and obtained very similar results compared to the corresponding time series without gaps. As an empirical rule derived by tests with synthetic time series we found that if a bin contains at least 30% of the data points and the time span covered in the bin is at least 50% of τ it can be included in the calculation. It is worthy to mention that it does not make a difference whether the time series is detrended or not, since only the difference of slopes of consecutive bins is used. While the upper limit of the length of τ is specified by the time series length, the lower limit is specified by the sampling rate and numerical stability. Testing with synthetic time series we found that starting from bin length τ larger than four times the sampling rate improves the numerical stability of the calculation drastically.

3.3 Error model

The method described in Section 3.2 provides the velocity uncertainty for any interval length of the time series within the accessible range of τ limited by the necessity of multiple bins to get a statistically significant value of the variance and by the sampling period ($4t < \tau < L/4$, where t is the sampling period and L the length of the time series). In most cases we want to assess the velocity uncertainty corresponding to the full length of the time series. In order to do so an error model based on assumptions on the noise characteristics is required and a corresponding function has to be adjusted to the slope variance. Its extrapolation to the full length of the time series can then be interpreted as the variance of the velocity of the full time series. The extrapolation requires a function based on assumptions on the noise characteristics. Unless a complete analysis of all noise contributions in GPS time series is considered, the choice of the right error model will be subject to debate. Here, some of the most common error models were applied to the AVR of synthetic time series, in order to validate the presented method.

3.3.1 Power law noise

Agnew (1992) analyzed the time-domain behavior of Gaussian power law noise (Eqn. 3.1) and derived the relation

$$\sigma_x(T) \propto T^{-\frac{(\nu+1)}{2}} \quad (3.3)$$

for the standard deviation σ_x of the position for a given time series with a spectral index ν and length T . This implies that for $\nu \leq -1$ the position uncertainty does not decrease with increasing the length of the time series, the process is not stationary. It has been stated by (Allan, 1966; Bos *et al.*, 2008) that the variance σ^2 of the linear velocity v is proportional to:

$$\sigma_v^2(T) \propto T^{-(\nu+3)} \quad (3.4)$$

Here we provide a mathematical proof of this relation. The time domain behaviour of the one-dimensional power law process $x(t)$ is characterized by the Eqn. (3.1). Following the argumentation of Agnew (1992) an expression for the variance of the velocity $\sigma_w^2(T)$ can be derived by introducing

$$\begin{aligned} w_T(t) &= v(t+T) - v(t) \\ &= \frac{d}{dt} (x(t+T) - x(t)) \end{aligned} \quad (3.5)$$

which can be rewritten as a convolution using the formulation of Bracewell (1965)

$$\begin{aligned} w_T(t) &= \frac{d}{dt} (x(t) * [\delta(t-T) - \delta(t)]) \\ &= x(t) * \frac{d}{dt} [\delta(t-T) - \delta(t)] \end{aligned} \quad (3.6)$$

The Fourier transform of this expression is

$$F_w(f) = \int_{-\infty}^{\infty} x(t) \cdot e^{-2\pi i t f} dt \cdot \int_{-\infty}^{\infty} \frac{d}{dt} [\delta(t-T) - \delta(t)] \cdot e^{-2\pi i t f} dt \quad (3.7)$$

This can be rewritten as

$$F_w(f) = F_x(f) \cdot 2\pi i f \cdot (e^{-2\pi i T f} - 1) \quad (3.8)$$

by applying

$$\int_{-\infty}^{\infty} \frac{d\delta(x)}{dx} f(x) dx = \frac{d}{dx} f(0) \quad (3.9)$$

Then the power spectrum $P_w(f)$ of can be calculated by

$$\begin{aligned} P_w(f) &= F_w \cdot F_w^* \\ &= F_x \cdot F_x^* \cdot 2\pi i f \cdot (e^{-2\pi i T f} - 1) \cdot [2\pi i f \cdot (e^{-2\pi i T f} - 1)]^* \\ &= P_x(f) \cdot 32\pi^2 f^2 \sin^2(\pi f T) \end{aligned} \quad (3.10)$$

The variance $\sigma_w^2(T)$ of the velocity $w(T)$ is defined as

$$\begin{aligned} \sigma_w^2(T) &= \int_0^\infty P_w(f) df \\ &= \int_0^\infty P_x(f) \cdot 32\pi^2 f^2 \sin^2(\pi f T) df \end{aligned} \quad (3.11)$$

Finally, $P_x(f)$ can be specialized by Eqn. (3.1) and the integration variable changed to $u := \pi f T$. Then we find

$$\begin{aligned} \sigma_w^2(T) &= \frac{32P_0}{\pi^{\nu+1} f_0^\nu} T^{-(\nu+3)} \int_0^\infty u^{\nu+2} \sin^2(u) du \\ &= C_\nu \frac{P_0}{f_0^\nu} T^{-(\nu+3)} \end{aligned} \quad (3.12)$$

Note, that the integral tends to infinity and $C_\nu \rightarrow \infty$, if all frequencies from 0 to ∞ are considered. In reality, they are limited by the sampling frequency and the length of the time series, thus C_ν can be an arbitrary large number. However, in the case of Gaussian distributed noise this expression nevertheless implies the linear relationship

$$\mu = -(\nu + 3) \quad (3.13)$$

between the spectral index ν and the slope μ of the AVR in a log-log plot (see Table 3.1). This relationship between μ and ν is also in agreement with Williams (2003b). Unlike the position, the velocity information still improves with observation length for $\nu > -3$.

In the case of a power law noise the AVR of the velocity as a function of the length of the time series can be modelled by:

$$\sigma_v^2(T) = a_{pl} \cdot T^\mu \quad (3.14)$$

In order to test the presented method, 21,000 time series with spectral indices $-2 \leq \nu \leq 0$ were created and analyzed. A subset of 1,000 points were taken from time series of 10,000 points to avoid boundary effects. All time

3 ESTIMATION OF VELOCITY UNCERTAINTIES FROM GPS TIME SERIES: EXAMPLES FROM THE ANALYSIS OF THE SOUTH AFRICAN TRIGNET NETWORK

Table 3.1: Spectral index ν and corresponding slopes of the AVR in a log-log plot μ for the most frequently mentioned noises with Gaussian distribution.

	ν	μ
white noise	0	-3
flicker noise	-1	-2
random walk	-2	-1

series were generated as a superposition of Ornstein-Uhlenbeck processes (Kasdin, 1995; Milotti, 2006). The time series were also analyzed using CATS, a *psd* spectral analysis Matlab routine (Stoica and Moses, 1997; Welch, 1967; Oppenheim and Schaffer, 1989) and by a method introduced by Lomb (1976) and Scargle (1982). The Matlab routine is based on the periodogram, which is a widely used, simple, and fast algorithm, although it is known to be a biased estimate (e.g. Stoica and Moses, 1997) and is included only for completeness.

The results are summarized in Fig. 3.2 showing the average and the dispersion of the difference between the estimated spectral index for the different methods and the spectral index utilized to create the time series. The errorbars denote the standard deviation of the estimates. Although CATS is clearly the best performing method, it is evident that all the different methods are able to estimate the correct spectral index within the corresponding dispersion and with a relative accuracy smaller than 0.1. A bias in the *psd* method is clearly visible for low spectral indexes. We also note that the AVR tends to produce a slightly higher power spectrum at high spectral indexes probably due to the numerical stability choice of starting the integration from $\tau > 4t$ (thus partially decreasing the contribution of white noise). We also note an increase in the dispersion of the results at lower spectral indexes probably due to the necessity to limit the interpolation to τ not longer than $1/4$ of the length of the time series.

3.3.2 White noise, flicker noise, and random walk

Previous studies (e.g. Zhang *et al.*, 1997; Mao *et al.*, 1999) suggested that the noise in GPS time series consists of a combination of white noise, flicker noise, and random walk. One reason for the use of these three particular noise contributions was that the derivations of the corresponding covariance matrices existed only for these integer spectral indices. Although today it is

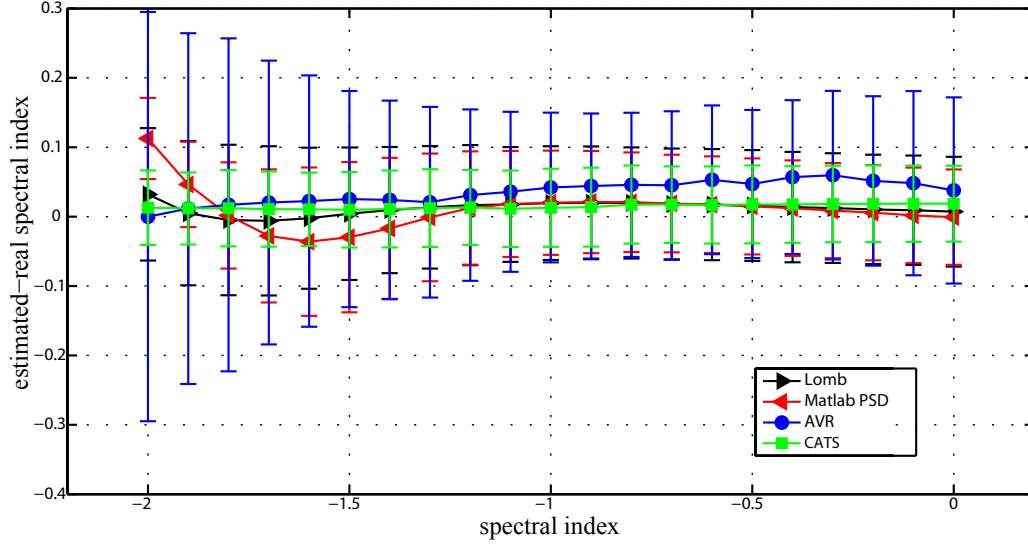


Figure 3.2: Estimated spectral indices with standard deviations from synthetic time series. The time series were created with length of 10,000 days, but only 1,000 were used in order to avoid boundary effects. 1,000 time series of each spectral index were created and analyzed by the AVR method introduced here. The spectral indices were estimated by a nonlinear fit weighting the data points by τ (blue). For comparison 100 time series of each spectral index were analyzed by CATS (green), a MatLab implemented function to calculate the power spectral density (red), and a method introduced by Lomb (1976) and Scargle (1982) (black). The later two methods provide power spectra and the spectral indices were calculated by linear regression of the log-log representation of the power spectra.

3 ESTIMATION OF VELOCITY UNCERTAINTIES FROM GPS TIME SERIES: EXAMPLES FROM THE ANALYSIS OF THE SOUTH AFRICAN TRIGNET NETWORK

possible to derive the covariance matrix for any power law noise by fractional differencing and integrating, the estimation of the spectral index along with the noise magnitudes is computationally expensive. Therefore most GPS velocity uncertainties are still calculated assuming an error model consisting of the aforementioned noise types.

The method presented here is also able to deal with error models consisting of a combination of white noise, flicker noise, and random walk by using the relationship between spectral index and power law behavior of the AVR (Eqn. 3.13). For this error model the variance of the rate can be written as:

$$\sigma_{wn+fl+rw}^2(\tau) = a_{wn} \cdot \tau^{-3} + a_{fl} \cdot \tau^{-2} + a_{rw} \cdot \tau^{-1} \quad (3.15)$$

where a_{wn} , a_{fl} , and a_{rw} are the coefficients for white noise, flicker noise, and random walk respectively. Table 3.1 summarizes the different noise types, their spectral indices and the corresponding AVR exponents.

In the case of a linear combination of different noise types it is interesting to look at the values τ_{co} , where the slope of the AVR changes (crossover bin length). For these bin lengths the contribution of the corresponding noise types have the same magnitude. The τ_{co} separate regimes where the specific noise contributions are dominant. Noise processes with lower spectral indices, for example random walk, are dominant at larger bin lengths, while noise with a higher spectral index such as white noise is dominant for shorter bin lengths. Therefore error sources with a correspondingly small ν ($\nu \rightarrow -\infty$) can never be ruled out for finite time series, since low spectral index processes may become dominant for bin lengths exceeding the length of the time series.

Similarly to what we did for testing the power law model, synthetic time series consisting either of one noise type or a combination of different noise types were created. Then the AVR was computed. Finally, we adjusted the parameters a_{wn} , a_{fl} , and a_{rw} in the error model function (Eqn. 3.15) to fit the AVR (see Fig. 3.3 and Table 3.2). In general we were able to estimate the correct noise contributions in the accessible range of bin lengths (a region bounded below by four times the sampling frequency and above by 1/4 of the length of the time series).

As an example we can look at the case of “white noise + random walk” (Fig. 3.3 E). Eqn. (3.15) was adjusted to the variances looking for the values of a_{wn} , a_{fl} , and a_{rw} that represent the calculated variances best. We used those parameters to extrapolate function (3.15) to the full length of the time series (red lines Fig. 3.3). This value is the velocity variance of the given time series. As expected for this particular synthetic time series with

3.3. ERROR MODEL

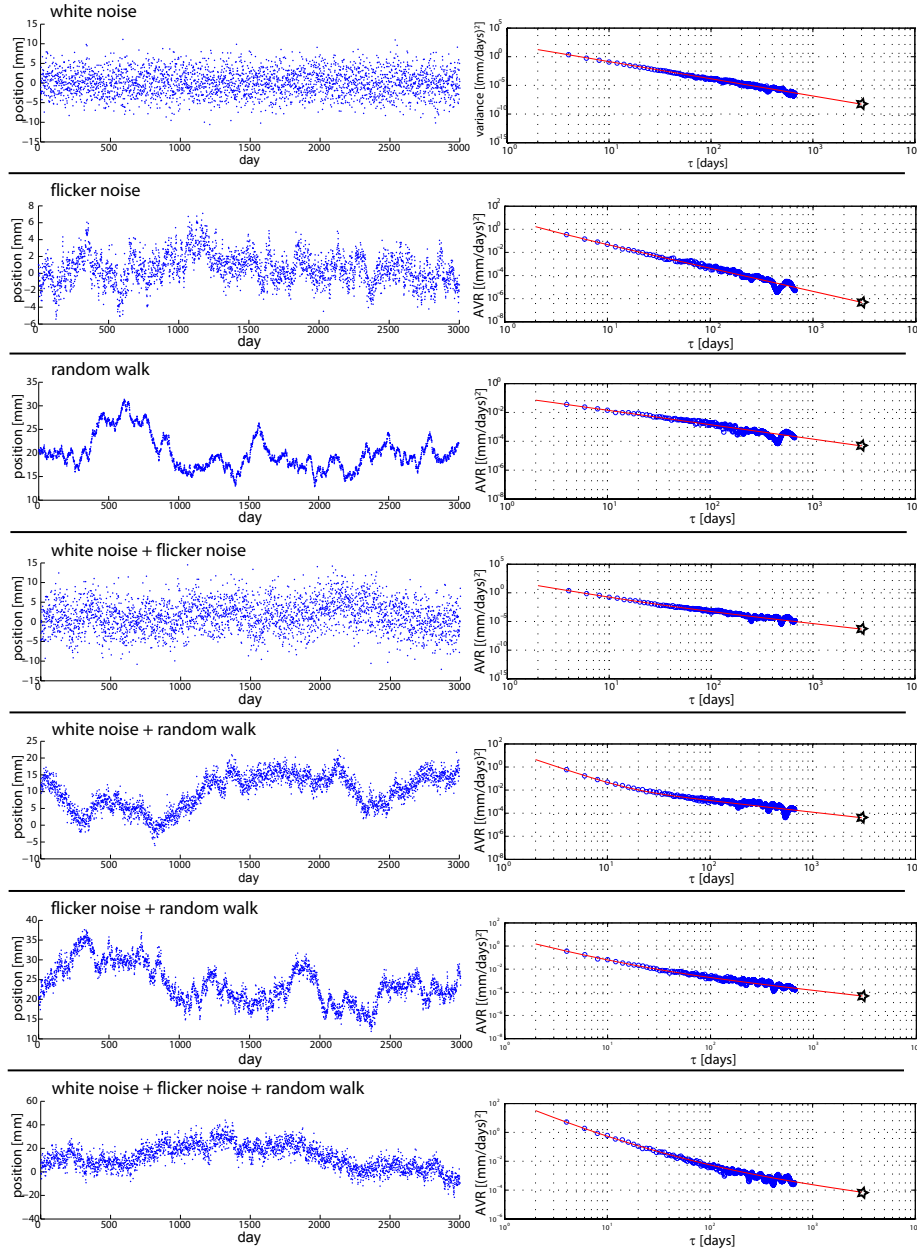


Figure 3.3: Synthetic time series (left) and the corresponding AVRs (right). The time series consist of white noise, flicker noise, or random walk and any possible combination of these noise types. The coefficients in Eqn. 3.15 - the error model (red lines in the figures on the right) - are estimated by least square fitting to the variances based on more than four bin pairs (blue circles in variance plots) and are summarized in Table 3.2. The cross over periods τ_{co} (in days) confine intervals where the different noise contributions are dominant.

3 ESTIMATION OF VELOCITY UNCERTAINTIES FROM GPS TIME SERIES: EXAMPLES FROM THE ANALYSIS OF THE SOUTH AFRICAN TRIGNET NETWORK

Table 3.2: Parameter estimates of example time series shown in Fig. 3.3

noise	a_{wn} [mm ² · day]	a_{fl} [mm ²]	a_{rw} [mm ² /day]	σ_v^2 [(mm/yr) ²]
white noise	142	$2.22 \cdot 10^{-14}$	$2.22 \cdot 10^{-14}$	0.026
flicker noise	4.94	4.26	$2.22 \cdot 10^{-14}$	0.25
random walk	$2.22 \cdot 10^{-14}$	$2.22 \cdot 10^{-14}$	0.143	2.52
wn + fl	136	4.17	$2.22 \cdot 10^{-14}$	0.25
wn + rw	34.7	$2.22 \cdot 10^{-14}$	0.122	2.33
fl + rw	2.21	4.67	0.143	2.53
wn + fl + rw	191	33.6	0.204	3.09
	$\tau_{co}(wn-fl)$ [days]	$\tau_{co}(fl-rw)$ [days]	$\tau_{co}(wn-rw)$ [days]	
white noise	$6.38 \cdot 10^{15}$	1.00	$7.99 \cdot 10^7$	
flicker noise	1.16	$1.92 \cdot 10^{14}$	$1.49 \cdot 10^7$	
random walk	1.00	$1.15 \cdot 10^{-13}$	$3.34 \cdot 10^{-7}$	
wn + fl	32.5	$1.88 \cdot 10^{14}$	$7.81 \cdot 10^7$	
wn + rw	$1.56 \cdot 10^{15}$	$1.82 \cdot 10^{-13}$	169	
fl + rw	0.473	32.8	4.01	
wn + fl + rw	5.69	165	30.6	

only white noise and random walk the coefficient a_{fl} is negligible. For this particular time series, the crossover bin length of white noise and random walk $\tau_{co}(wn - rw)$ is 169 days. This means that for observations shorter than this time span white noise is the dominant noise contribution while for longer observations it is random walk. For flicker noise a virtually vanishing contribution is estimated and crossover bin lengths are thus meaningless.

3.3.3 Seasonal effects

Many GPS time series show annual signals mainly due to seasonal loading. In most cases the seasonal signals are just modelled by the first and the second harmonics of a sine function, where the fundamental period is one year. The signal is then subtracted from the time series. Blewitt and Lavallée (2002) showed that a seasonal signal still affects the velocity uncertainty and presented the following series to estimate the velocity uncertainty introduced by a seasonal signal:

$$\sigma_{annual}^2(\tau) = \frac{18T^2 a_1^2}{\pi^2 \tau^4} \sum_{k=1}^{\frac{T}{2\Delta t}} \frac{1}{k^3} \left(\cos\left(\frac{\pi k \tau}{T}\right) - \frac{T}{\pi k \tau} \sin\left(\frac{\pi k \tau}{T}\right) \right)^2 \quad (3.16)$$

where a_1 is the amplitude of the contribution at the fundamental period T , Δt is the sampling interval, and τ is the length of the time series. Blewitt and Lavallée (2002) indicated that the contributions with $k = 1, 2$ (annual and semiannual) account for $\sim 90\%$ of the total variance. Eqn. (3.16) is limited to $\tau > T$, which makes it difficult to use it for fitting in the presence of noise, since the adjustment should include the full range of τ . Bos *et al.* (2010) showed the importance of including the effect of colored noise when dealing with periodic signals.

A periodic signal is not a stochastic process and as a consequence the AVR cannot directly be identified with the velocity variance. Here we discuss the effect of a periodic signal on the AVR and show how the method presented here can be used to estimate the amplitude at the fundamental period, which then can be used along with Eqn. (3.16) to estimate correct velocity uncertainties. There are two advantages of doing so: (1) the amplitude is estimated along with other (colored) noise parameters and (2) the phase is not present in this formulation.

The AVR for a pure sinusoidal signal of the form

$$x(t) = a \cdot \sin\left(\frac{2\pi}{T}t + \Phi\right) \quad (3.17)$$

where a is the amplitude of the signal, T its period, and Φ a phase can be calculated analytically with Maple (TM). The expression obtained is very complex and not suitable for fitting an error model, but it can be approximated by

$$\sigma_{annual}^2(\tau) = \frac{36T^2a^2}{\pi^2\tau^4} \sin^2\left(\frac{\pi\tau}{T}\right) \cdot \left(\frac{T}{\pi\tau} \sin\left(\frac{\pi\tau}{T}\right) - \cos\left(\frac{\pi\tau}{T}\right)\right)^2 \quad (3.18)$$

where a is the amplitude of the sinusoidal signal that can be solved for by fitting the data for a given period T (e.g. $T = 365$ days for an annual signal).

Eqn. (3.18) is identical to the one derived by Blewitt and Lavallée (2002) for the velocity bias from a sinusoidal signal, apart from a phase not present on the AVR. The absence of the phase term is due to the fact that the AVR is computed using the difference of consecutive bin pairs. At every phase of a harmonic signal the difference is zero at integer multiples of T independent from the phase. In this way, as long as we have enough bins, the phase bias to the AVR is averaged out.

It is possible to apply the AVR and to fit an adequate model that accounts for the colored noise (like the ones described in Sections 3.3.1 and

3.3.2) combined with the expression of the annual signal (Eqn. 3.18). By fitting the AVR to this model, a (that can be identified with a_1 in Eqn. 3.16) can be estimated along with the parameters describing the time correlated noise (e.g. μ and a_{pl} in Eqn. 3.14). The values obtained by the fit can then be used in a linear combination of the selected noise model (e.g. Eqn. 3.14) and Eqn. 3.16 to extrapolate the variance to the full length of the time series.

As an example we created a synthetic time series consisting of flicker noise plus an annual signal of arbitrary phase. Fig. 3.4 shows the time series (top) and the corresponding AVR (bottom). The red curve represents the adjusted model consisting of a linear combination of Eqn. 3.14 and Eqn. 3.18 corresponding to the parameters a_{pl} , μ , and a_1 that best reproduce the observed variance. The obtained parameter a_1 (corresponding to the amplitude of the sinusoidal signal) can now be used in the linear combination of Eqn. 3.14 and Eqn. 3.16 for extrapolation to the full length of the time series (black curve in Fig. 3.4). The values of the black curve at the full time series length corresponds to the velocity variance when we take into account both colored noise and a periodic signal.

Note, that for $\tau > T$ the variance introduced by an annual signal decreases with τ^{-4} , even faster than white noise.

3.3.4 Offsets and velocity changes

Sometimes GPS time series are affected by offsets or changes in rates. Sources for offsets could include antenna changes or co-seismic displacements. Velocity changes have been observed after large earthquakes, but could also be related to other effects like monumentation or water pumping. These signals affect the AVR. Although no analytical expressions for these cases were derived, we want to point out some characteristics.

An offset in the time series causes a change in trend of the AVR. In the case of “white noise + offset” the slope variance shows a similar behavior like a random walk process, which is in agreement with Williams (2003a).

If there is a change of rate in the time series, it is possible that the corresponding AVR of the rate shows a kink and increases with τ for a certain range of integration intervals.

The above mentioned error models are not suitable for uncertainty estimation of time series affected by offsets or velocity changes, since the models do not account for those effects. However, it is possible to identify corresponding patterns in the AVR and correct affected time series and/or apply different kinds of error models.

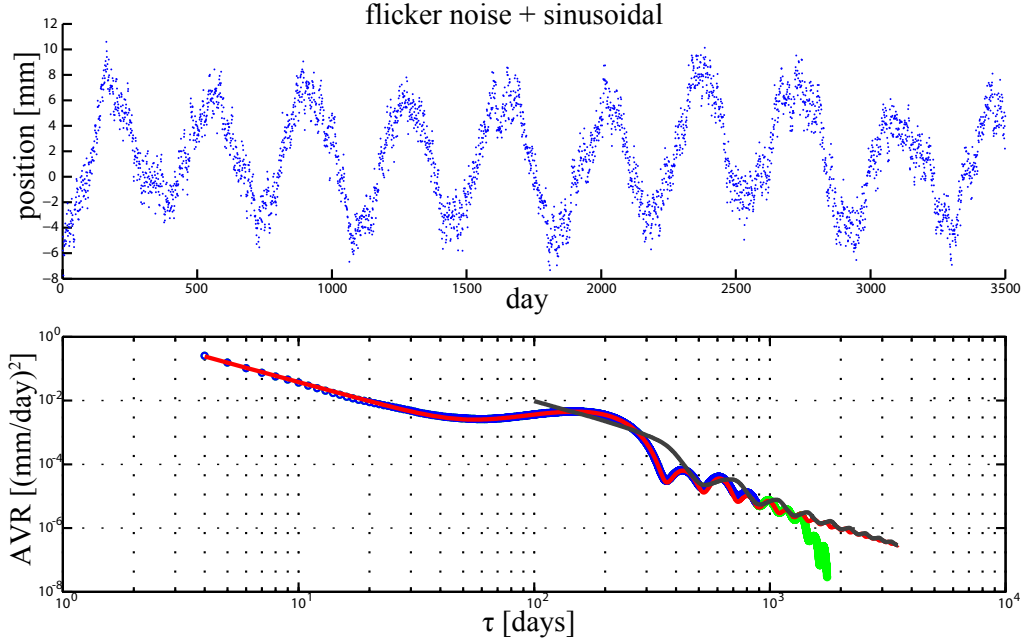


Figure 3.4: Synthetic time series consisting of flicker noise plus a sinusoidal signal with period $T = 365$ days and amplitude $a = 5$ mm (top) and the corresponding AVR (bottom). Green circles are based on four or less independent bin pairs and thus not included in the fitting. Blue circles are based on more than four bin pairs and were used to fit a linear combination of Eqn. 3.14 and Eqn. 3.18 (red line). The obtained values are $a_{pl} = 3.9$, $\mu = -2.0$, and $a_1 = 4.7$, which compares well to the amplitude of the periodic signal. For extrapolation to the length of the time series the obtained parameter were set into a linear combination of Eqn. 3.14 and 3.16 (black line). The calculated velocity uncertainty in this case is $\sigma_v = 0.20$ mm/yr.

3.4 TrigNet

TrigNet is a network of about 50 continuously operating GNSS base stations distributed throughout South Africa (see Fig. 3.5). Data span up to nine years for most of the TrigNet sites and are freely available (<http://www.trignet.co.za/>). They were processed using the Bernese GPS Software, V5.0 (Dach *et al.*, 2007) using state of the art analysis strategies and standards. For consistency, orbit products from the CODE (Center for Orbit Determination in Europe) Analysis Center of the International GNSS Service (IGS) were used (Dow *et al.*, 2009). Tracking data were analyzed in daily batches in ionosphere-free linear combination and phase ambiguities were resolved to integers. Two-hourly troposphere zenith delay and daily gradient parameters were estimated for each station. Station velocities were retrieved by combining daily solutions at the normal equation level. Some 30 IGS stations were included into the network to realize the geodetic datum.

The obtained velocities were rotated into a South Africa fixed reference frame by an Euler rotation minimizing the velocity residuals (Malservisi *et al.*, 2008). Most residual velocities are < 1 mm/yr (Table 3.3), as expected for an Archean cratonic region not affected by tectonic deformation. In order to solve for any internal deformation the velocity uncertainty is crucial. In theory, the residuals with respect to the stable region like South Africa should be of the same order of magnitude as the error. The formal error is about $0.01 - 0.02$ mm/yr for the horizontal components of most sites - a magnitude smaller than the observed residuals, suggesting a clear signal in the observed velocity field. Given the almost random distribution of the azimuth of the residuals we expect that for the majority of the sites this is not the case and that the error is largely underestimated due to the fact that the formal error neglects time correlated noise.

On the other hand, the application of the method introduced by Mao *et al.* (1999) produced errors significantly larger (almost one order of magnitude) than the residuals indicating that the uncertainties of the velocity field are overestimated. Given the importance of the associated error in the interpretation of such small residuals, it is clearly important to make a more complete analysis of the uncertainty associated with the studied velocity field. The AVR provides a quick method to improve the error estimation. Given the availability of specific algorithms to compute time correlated uncertainties for GPS velocities like CATS, the algorithm presented by Bos *et al.* (2008), or the one presented here we strongly suggest that neither pure white noise models nor empirical methods (e.g. Mao *et al.*, 1999) should be

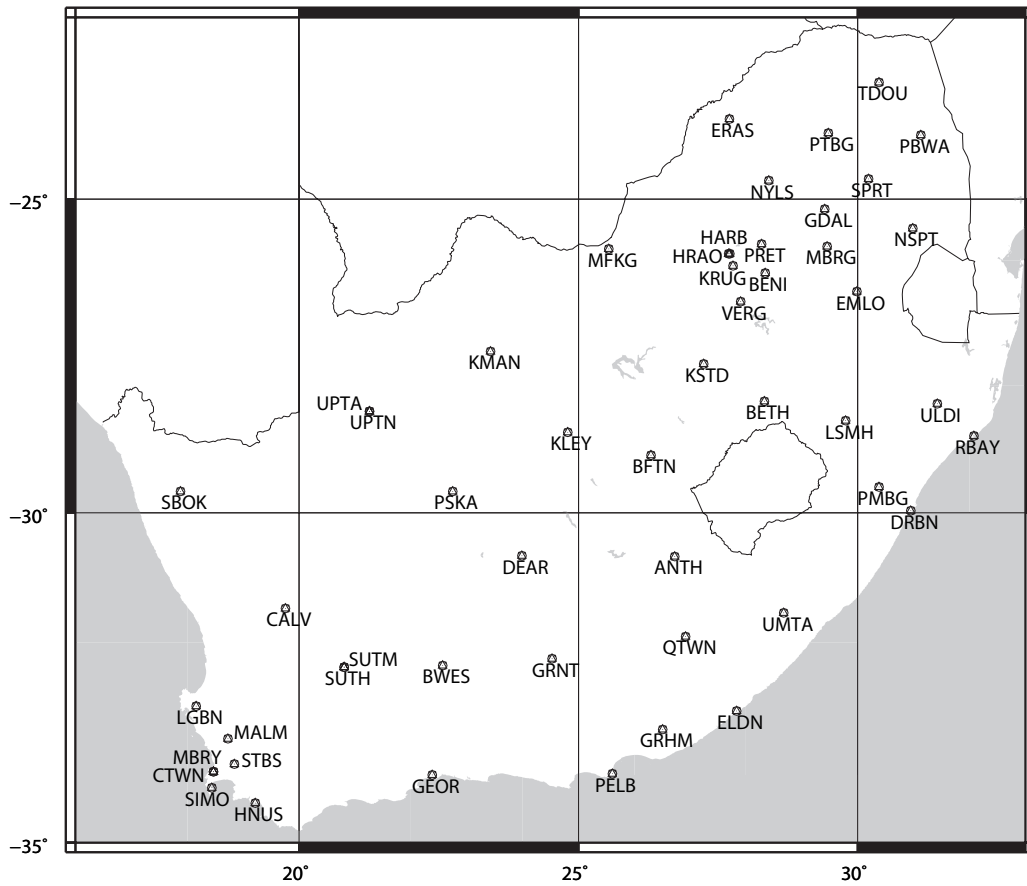


Figure 3.5: Spatial distribution of the South African GPS network TrigNet.

3 ESTIMATION OF VELOCITY UNCERTAINTIES FROM GPS TIME SERIES: EXAMPLES FROM THE ANALYSIS OF THE SOUTH AFRICAN TRIGNET NETWORK

used for the estimation of velocity uncertainties from continuous GPS or semi-permanent sites with sufficient amount of data.

3.4.1 CATS vs AVR

In order to estimate correct velocity uncertainties for the TrigNet time series CATS and the AVR method were applied. For both methods the same error model consisting of a power law noise plus an annual signal was used. The three components were treated independently in the calculation of the uncertainty, which is common practice. For the majority of the sites the spectral indices computed for the three components of the velocity are very similar, indicating that all the components are subject to the similar type of noise.

In the case of the AVR an error model consisting of a linear combination of Eqn. (3.14) and Eqn. (3.18) was adjusted to the variances, solving for the parameters a_{pl} , μ , and a_1 by weighted nonlinear least-squares. In order to improve the numerical stability of the least-square fit, only bins with lengths $\tau > 6$ days were included in the parameter estimation. To put more importance to the variances at greater τ and to stabilize the estimation of the parameters the computed variances were weighted by τ . In tests with synthetic time series this weighting clearly improved the parameter estimation. This method is similar to the use of the logarithm of the data, a common practice in inversion methods when dealing with data with very different scales. Finally, the velocity uncertainties were estimated by extrapolating the linear combination of Eqn. (3.14) and Eqn. (3.16) to the full length of the time series. As an example Fig. 3.6 shows the time series and the corresponding slope variance at Hermanus (HNUS).

In general, the calculations led to comparable results for both methods as summarized in Table 3.3 and Fig. 3.7. Note, that the calculation times are significantly different, on a standard desktop PC (Dual Core 2.93 GHz, 4 GB RAM) the analysis of the network using CATS takes several days, while it takes only a few minutes (hours in the case of overlapping bins) to calculate the uncertainties using the AVR of the rate.

The results calculated with the Allan variance tend to be slightly more conservative. A possible reason for this difference could be how white noise, that is likely to be present in the time series, is treated in the two methods.

The shift towards higher uncertainties in our method becomes more apparent for sites with larger uncertainty σ , probably due to the fact that these time series are in general shorter thus more influenced by white noise.

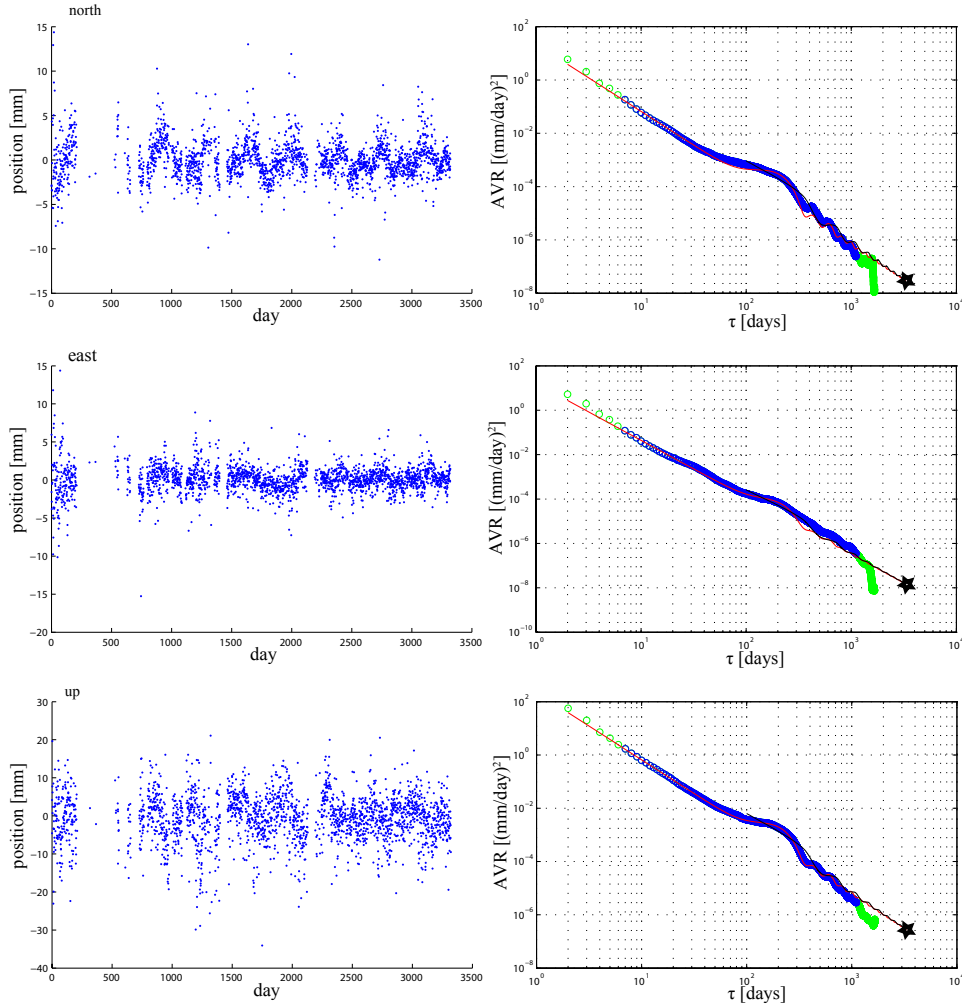


Figure 3.6: Time series (left) and corresponding AVRs (green and blue circles in the figures on the right) of the velocities for the three components of the GPS site at Hermanus (HNU5), South Africa. Variances that are based on more than six bin pairs (blue circles) were used to fit an error model (red line), which consists of a linear combination of power law noise (Eqn. 3.14) and an annual signal (Eqn. 3.18). The following parameters were obtained: $a_{pl}(north) = 22.3$, $\mu(north) = -2.53$, $a_1(north) = 1.32$, $a_{pl}(east) = 16.3$, $\mu(east) = -2.57$, $a_1(east) = 0.58$, $a_{pl}(up) = 225$, $\mu(up) = -2.53$, and $a_1(up) = 3.26$. The rate uncertainty is the result of the extrapolation of the black curve (see Fig. 3.4). The stars in the variance plots denote the variances of the velocities, the corresponding standard deviations are $\sigma(north) = 0.065$ mm/yr, $\sigma(east) = 0.045$ mm/yr, and $\sigma(up) = 0.053$ mm/yr.

3 ESTIMATION OF VELOCITY UNCERTAINTIES FROM GPS TIME SERIES: EXAMPLES FROM THE ANALYSIS OF THE SOUTH AFRICAN TRIGNET NETWORK

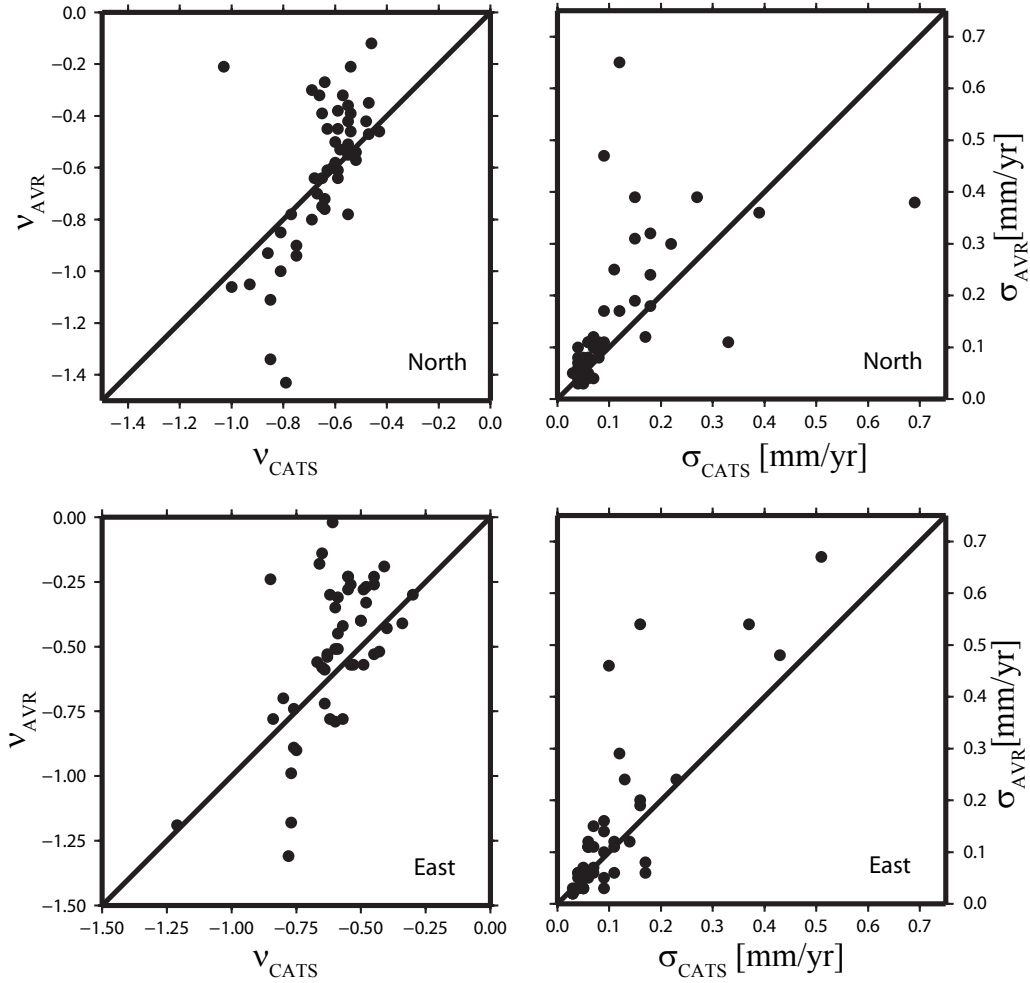


Figure 3.7: Scatter plots of the spectral indices (left) and the calculated velocity uncertainties (right) of the north (top) and the east (bottom) components of the TrigNet data set using CATS and AVR.

Another reason for discrepancies of the two methods could be non Gaussian noise. The estimation of the spectral index in our method is based on the assumption of Gaussian distributed noise and the result could deviate from the one obtained by a different method.

In general, the results of the two methods are more similar in cases where the selected error model fits well the computed AVR (i.e. the red curve in the figures fits well the blue dots). This behavior emphasizes the importance of the right choice of the error model and also shows the potential of the AVR to visually check whether an error model is suitable or not.

3 ESTIMATION OF VELOCITY UNCERTAINTIES FROM GPS TIME SERIES: EXAMPLES FROM THE ANALYSIS OF THE SOUTH AFRICAN TRIGNET NETWORK

Table 3.3: Trignet residual velocities, their uncertainties, and the corresponding spectral indices. Length indicates the time span covered by the time series. The uncertainties were calculated using CATS and the AVR method presented here. The formal error is on the order of $0.01 - 0.02$ mm/yr in most cases.

site	lon [°]	lat [°]	length [days]	comple- teness	v_{east} [mm/yr]	v_{north} [mm/yr]	σ_{CATS}^{east} [mm/yr]	σ_{CATS}^{north} [mm/yr]	σ_{east}^{AVR} [mm/yr]	σ_{north}^{AVR} [mm/yr]	ν_{CATS}^{east}	ν_{CATS}^{north}	ν_{AVR}^{east}	ν_{AVR}^{north}
HRAO	27.69	-25.89	3374	0.89	-0.51	-0.20	0.09	0.06	0.05	0.05	-0.59	-0.59	-0.31	-0.45
SUTH	20.81	-32.38	3372	0.90	0.18	0.11	0.10	0.05	0.46	0.06	-0.78	-0.60	-1.31	-0.60
HNUS	19.22	-34.42	3320	0.67	-0.08	-0.06	0.04	0.05	0.05	0.06	-0.40	-0.47	-0.43	-0.47
GEOR	22.38	-34.00	3274	0.52	-0.77	-0.27	0.05	0.04	0.05	0.07	-0.65	-0.59	-0.58	-0.64
PELB	25.61	-33.98	3267	0.51	0.02	-0.03	0.07	0.18	0.15	0.32	-0.75	-1.00	-0.90	-1.06
ELDN	27.83	-33.04	3266	0.70	-0.20	-0.05	0.04	0.04	0.03	0.05	-0.57	-0.55	-0.42	-0.55
BFTN	26.30	-29.10	3185	0.61	2.59	-1.18	0.29	0.09	1.83	0.47	-1.17	-0.85	-1.80	-1.34
UMTA	28.67	-31.55	3164	0.71	0.49	-0.24	0.03	0.05	0.02	0.04	-0.48	-0.65	-0.27	-0.39
BETH	28.33	-28.25	3164	0.78	-0.13	-0.04	0.03	0.03	0.03	0.05	-0.48	-0.52	-0.33	-0.57
PMBG	30.38	-29.60	3159	0.44	0.20	-0.12	0.05	0.04	0.05	0.04	-0.60	-0.55	-0.51	-0.36
LSMH	29.78	-28.56	3159	0.62	0.15	0.13	0.03	0.04	0.02	0.03	-0.45	-0.54	-0.23	-0.39
KLEY	24.81	-28.74	3159	0.60	0.27	-0.03	0.11	0.04	0.11	0.10	-0.80	-0.55	-0.70	-0.78
DRBN	30.95	-29.97	3155	0.57	0.27	-0.12	0.05	0.05	0.03	0.08	-0.60	-0.65	-0.35	-0.64
HARB	27.71	-25.89	3150	0.88	-0.07	0.07	0.05	0.06	0.03	0.07	-0.62	-0.63	-0.30	-0.61
SBOK	17.88	-29.67	3134	0.79	-0.02	-0.31	0.06	0.06	0.05	0.08	-0.63	-0.68	-0.53	-0.64
DEAR	23.99	-30.67	3125	0.67	-0.10	-0.20	0.03	0.04	0.02	0.08	-0.55	-0.64	-0.28	-0.72
CALV	19.76	-31.48	3125	0.77	-0.27	-0.11	0.09	0.07	0.16	0.12	-0.76	-0.65	-0.89	-0.75
ULDI	31.42	-28.29	3108	0.66	0.24	0.00	0.04	0.06	0.03	0.11	-0.49	-0.64	-0.28	-0.76
RBAY	32.08	-28.80	3098	0.50	0.27	-0.30	0.06	0.05	0.11	0.03	-0.57	-0.54	-0.78	-0.21
LGBN	18.16	-32.97	3003	0.71	0.18	0.02	0.05	0.06	0.06	0.11	-0.64	-0.69	-0.59	-0.80
ERAS	27.70	-23.69	2949	0.64	-0.06	-0.23	0.05	0.05	0.03	0.05	-0.55	-0.55	-0.23	-0.42
MBRG	29.45	-25.77	2927	0.71	0.14	0.72	0.09	0.09	0.10	0.17	-0.76	-0.75	-0.74	-0.94
PTBG	29.47	-23.92	2924	0.62	-0.26	0.23	0.06	0.04	0.12	0.06	-0.62	-0.52	-0.78	-0.54
NSPT	30.98	-25.48	2879	0.72	-0.04	0.05	0.06	0.11	0.06	0.25	-0.63	-0.81	-0.54	-1.00
PBWA	31.13	-23.95	2843	0.71	0.32	0.00	0.07	0.06	0.07	0.04	-0.67	-0.63	-0.56	-0.45

site	lon [°]	lat [°]	length [days]	comple- teness	v_{east} [mm/yr]	v_{north} [mm/yr]	σ_{east}^{CATS} [mm/yr]	σ_{north}^{CATS} [mm/yr]	σ_{east}^{AVR} [mm/yr]	σ_{north}^{AVR} [mm/yr]	ν_{CATS} east	ν_{CATS} north	ν_{AVR} east	ν_{AVR} north
SIMO	18.44	-34.19	2703	0.51	-0.58	0.10	0.04	0.09	0.06	0.10	-0.34	-0.60	-0.41	-0.50
SUTM	20.81	-32.38	2578	0.92	-0.21	0.20	0.04	0.05	0.03	0.07	-0.45	-0.61	-0.26	-0.60
EMLO	29.98	-26.50	2561	0.78	-0.03	0.01	0.04	0.09	0.06	0.11	-0.54	-0.77	-0.57	-0.78
KMAN	23.43	-27.46	2531	0.79	0.20	-0.12	0.05	0.07	0.06	0.10	-0.59	-0.67	-0.51	-0.70
KSTD	27.24	-27.66	2529	0.61	-0.18	-0.42	0.06	0.05	0.11	0.06	-0.64	-0.58	-0.72	-0.53
MFKG	25.54	-25.81	2456	0.56	0.19	1.49	0.06	0.12	0.11	0.17	-0.60	-0.86	-0.79	-0.93
ANTH	26.72	-30.68	2260	0.77	0.02	0.20	0.05	0.06	0.07	0.08	-0.53	-0.59	-0.57	-0.61
TDOU	30.38	-23.08	2106	0.71	0.26	-1.89	0.12	0.15	0.29	0.39	-0.77	-0.85	-0.99	-1.11
GRNT	24.53	-32.25	2092	0.59	0.61	-0.05	0.09	0.07	0.03	0.04	-0.61	-0.46	-0.02	-0.12
BWES	22.57	-32.35	1987	0.56	0.34	0.20	0.17	0.08	0.06	0.08	-0.65	-0.54	-0.14	-0.46
PRET	28.28	-25.73	1901	0.83	0.16	-1.62	0.07	0.12	0.06	0.65	-0.59	-0.79	-0.45	-1.43
PSKA	22.75	-29.67	1694	0.85	0.14	-0.03	0.11	0.08	0.06	0.10	-0.66	-0.60	-0.18	-0.58
QTWN	26.92	-31.91	1679	0.78	0.74	1.15	0.16	0.15	0.54	0.31	-0.77	-0.75	-1.18	-0.90
NYLS	28.41	-24.70	1307	0.73	0.04	-0.17	0.09	0.08	0.14	0.11	-0.49	-0.43	-0.57	-0.46
GDAL	29.41	-25.16	1307	0.47	-0.10	0.57	0.11	0.08	0.12	0.09	-0.54	-0.47	-0.26	-0.35
MBRY	18.47	-33.95	1266	0.48	-0.07	0.23	0.17	0.33	0.08	0.11	-0.34	-0.52	0.11	0.15
GRHM	26.51	-33.32	1177	0.79	-0.07	0.23	0.07	0.27	0.11	0.39	-0.45	-0.81	-0.53	-0.85
UPTN	21.26	-28.41	1039	0.68	0.32	-0.68	0.14	0.17	0.12	0.12	-0.55	-0.64	-0.23	-0.27
SPRT	30.19	-24.67	969	0.89	2.04	-0.73	0.43	0.69	0.48	0.38	-0.84	-1.03	-0.78	-0.21
MALM	18.73	-33.46	850	0.85	0.18	0.06	0.16	0.15	0.20	0.19	-0.50	-0.48	-0.40	-0.42
STBS	18.84	-33.84	841	0.89	0.04	0.79	0.16	0.18	0.19	0.18	-0.50	-0.57	-0.40	-0.32
BENI	28.34	-26.20	794	0.87	6.66	2.71	0.51	0.22	0.67	0.30	-0.85	-0.59	-0.24	-0.38
KRUG	27.77	-26.08	791	0.86	0.03	-2.13	1.21	0.46	1.78	0.92	-1.21	-0.93	-1.19	-1.05
VERG	27.90	-26.66	788	0.91	-0.99	0.79	0.13	0.18	0.24	0.24	-0.43	-0.55	-0.52	-0.51
CTWN	18.47	-33.95	628	0.93	-0.07	0.23	0.37	1.25	0.54	1.12	-0.30	-0.69	-0.30	-0.30
UPTA	21.26	-28.41	508	0.87	0.18	-0.45	0.23	0.39	0.24	0.36	-0.41	-0.66	-0.19	-0.32

3.5 Conclusion

Although CATS provides a broad set of different error models and a more robust estimation of the velocity uncertainty being based on MLE, the method presented here gets similar results and is faster for many choices of error models. The computation time is on the same order than for the algorithm presented by Bos *et al.* (2008) in the case of overlapping bins. The AVR has also the advantage to separate the estimation of the velocity uncertainty into two independent steps. First the variance is calculated as a function of varying bin length. In a second step an error model is used to compute the velocity uncertainty. This provides the possibility to choose an error model according to the computed variances and eventually the possibility to change the model in the case that the fit of the variance is not satisfactory without having to redo the full analysis. It is thus possible to dedicate more effort in the choice and the adjustment of the error model.

Once the error is estimated correctly, the residual velocities for the TrigNet GPS network are of the same order than the estimated uncertainties for the majority of the sites in Fig. 3.8, as expected for stable rigid plate setting. Some of the sites do still present significant residuals. In particular, some sites in the region around Johannesburg (e.g. HRAO) show a clear velocity signal that is likely caused by human induced deformation. Sites in the northeastern part of South Africa (e.g. PBWA or ULDI) have significant eastward residuals possibly associated with the deformation at the complex plate boundary between the Nubian and Somalian plates (Stamps *et al.*, 2008). We also want to point out that some of the residuals can be associated with monumentation problems. In particular, PRET is installed on an unstable building, while QTWN and GEOR are combinations of multiple sites loosely connected by survey ties. BFTN and TDOU show high temporal correlations and relatively large errors, which could be related to local hydrological effects or monumentation problems. It is important to note that this interpretation of the velocity field as tectonic or non-tectonic deformation is only possible after a correct estimation of the effects of time correlated noise on the velocity uncertainties.

Fig. 3.9 shows the standard deviations of the velocities for the three components of the Trignet sites. As expected for sites that are subject to similar noise the shapes of the curves are quite similar for the different sites, but also for the three components with the up component being shifted towards larger uncertainties. The bump at $\tau \approx 183$ days that is present in most of the curves results from the seasonal signal present in the time series.

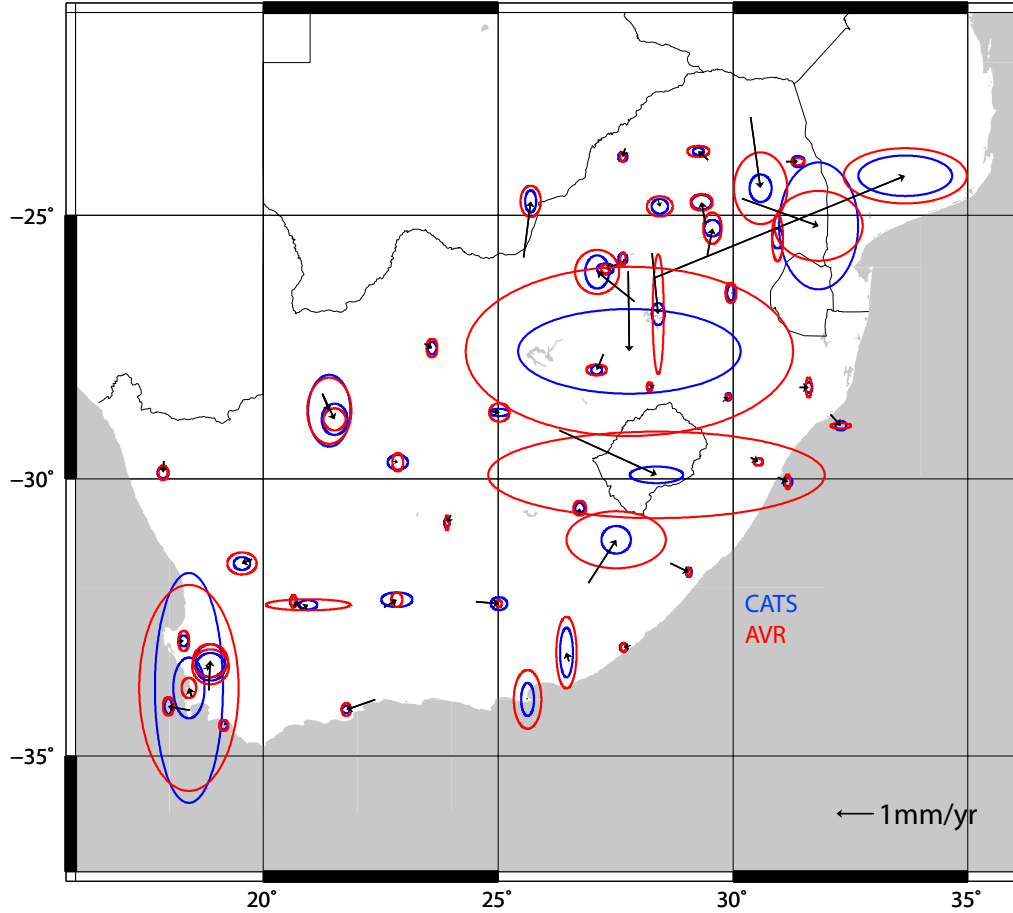


Figure 3.8: Horizontal residual velocity field of the South African GPS network TrigNet. The velocities are plotted with two error ellipses (95% confidence interval) corresponding to the different methods of uncertainty estimation (see Table 3.3). Blue ellipses correspond to the uncertainties calculated with CATS, red ellipses to the uncertainties calculated by the AVR method.

3 ESTIMATION OF VELOCITY UNCERTAINTIES FROM GPS TIME SERIES: EXAMPLES FROM THE ANALYSIS OF THE SOUTH AFRICAN TRIGNET NETWORK

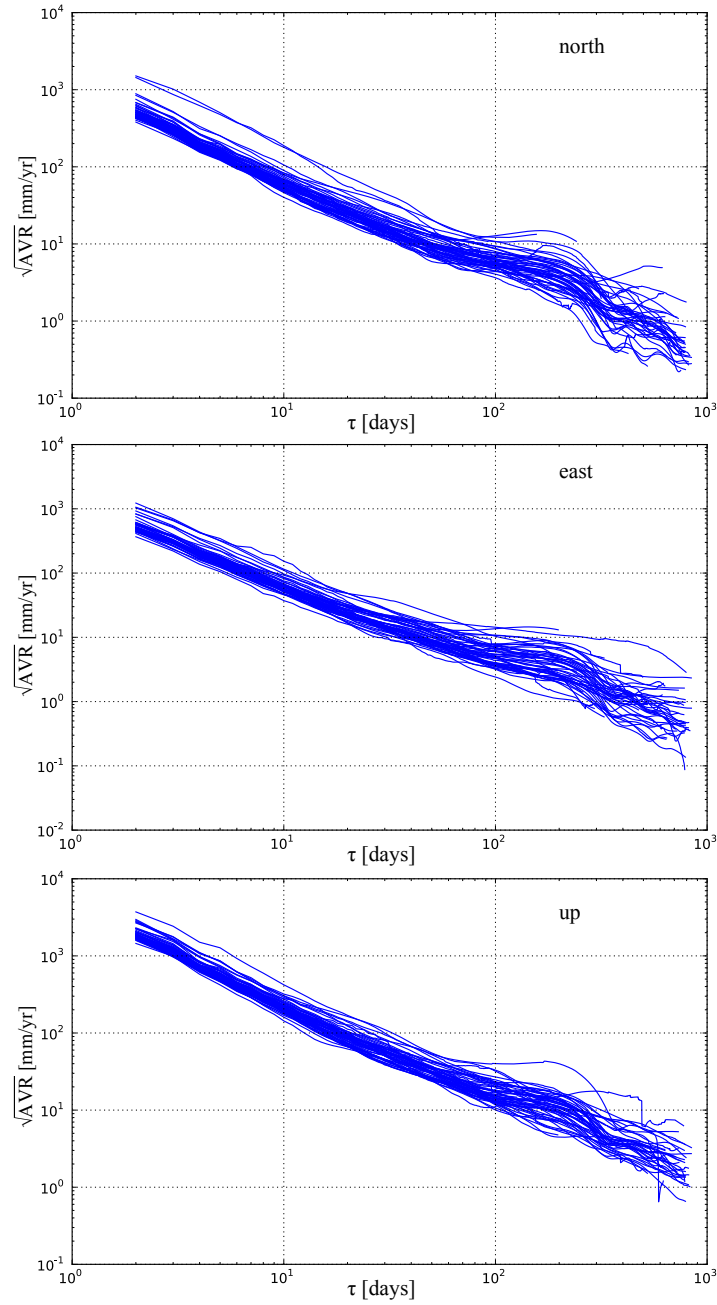


Figure 3.9: Standard deviations of the rates for three components of the Trignet sites as a function of bin length. Most of the sites show an almost linear behavior in the log-log plot and a bump at $\tau \approx 183$ days. The shapes of most of the curves are similar indicating similar sources of noise for the majority of the sites, which is also true for the different components.

Apart from that the almost linear behavior in the log-log plot indicates that a power law assumption is reasonable, although a trend to convexity is present in some curves suggesting a piecewise power law behavior. The curves of a few sites differ significantly from the average shape and are very likely subject to additional processes. They possibly require additional processing and modelling and the velocities obtained should be handled with special care. Note, that the method presented here provides this kind of analysis independently of assumptions on the error model.

3.6 Acknowledgments

We used data provided by the National Geo-spatial Information, Mowbray, South Africa and the International GNSS Service (IGS). GPS analyses were performed with the BERNese GPS software. This research benefitted from the availability of IGS data products. Figures were created using Matlab and the GMT software (Wessel and Smith, 1991). We appreciate constructive comments of Shimon Wdowinski and three anonymous reviewers that improved significantly the manuscript through constructive and thoughtful comments. This study was funded by DFG grants MA 4163/1-1 and MA 4163/1-2. MH is supported by the Elitenetzwerk Bayern and different research projects of Valerian Bachtadse.

4

Velocity Covariance of GPS Time Series in the Presence of Transients and Time Correlated Noise

by *M. Hackl, R. Malservisi, U. Hugentobler, and Y. Jiang*
Submitted to Geophysical Journal International

Abstract

We provide a method to derive the covariance of GPS velocities in the presence of time correlated noise based on the Allan variance of the rate (AVR). The velocity variance is calculated for different directions, which allows for noise properties, that are direction dependent. The results of this covariance analysis are not only useful for estimating realistic uncertainties for any model or application based on GPS velocities, but are of particular interest if the analyzed time series exhibits transient signals. Since time correlated noise and transients might result in similar patterns of time correlation in the velocity variance, this analysis can be used to test models of the tran-

sient processes. We show that GPS sites in subduction zones experiencing slow slip events (SSEs) show significant time correlation in the direction of the SSE associated with highly eccentric velocity confidence ellipses in the direction of relative plate motion. This time correlation is reduced significantly after modeling and subtracting these events from the time series. We use data from Mount St. Helens to show that models of volcanic activity, based on GPS time series similarly benefit from our noise analysis.

4.1 Introduction

GPS position time series provide an outstanding tool to measure crustal motion and deformation (e.g. Dixon, 1991; Segall and Davis, 1997). The availability of longer time series and the enhanced data quality allow a better and better analysis of time dependent effects in continental deforming zones. These analyses may provide insights to processes as the seismic cycle and allow drawing conclusions on parameters as the rheology of the crust and the underlying asthenosphere (e.g. Malservisi *et al.*, 2001; Schmalzle *et al.*, 2006; Perfettini and Avouac, 2007; Bürgmann and Dresen, 2008).

However, time series are subject to many different kinds of time correlated noise, whose various sources like the impact of multipath, clock and orbit errors, ionospheric and tropospheric effects can hardly be quantified properly (Johnson and Agnew, 1995; Zhang *et al.*, 1997; Mao *et al.*, 1999; Williams *et al.*, 2004; Langbein, 2008). Networks of GPS sites may also be affected by spatially correlated noise (e.g. Wdowinski *et al.*, 1997; Dong *et al.*, 2006). The effect of the correlated noise on the time series can be similar to the one caused by transients posing the problem of separating the signal from the noise (e.g. Williams, 2003b,a; Hackl *et al.*, 2011). One way to adress this problem has been introduced by Ji and Herring (2011), who were able to identify transient signals in GPS time series from the Akutan volcano by state estimation and principal component analysis.

Transient events in GPS time series are very common. They can result, for example, from post seismic relaxation (e.g. Savage and Lisowski, 1998; Perfettini and Avouac, 2007; Hackl *et al.*, 2009; Hammond *et al.*, 2010), glacial isostatic adjustment (e.g. Johansson *et al.*, 2002; Sella *et al.*, 2007), volcanic deformation (e.g. Dzurisin, 2003; Saballos *et al.*, 2012), anthropogenic deformation (e.g. Bawden *et al.*, 2001), and atmospheric processes (e.g. Jade and Vijayan, 2008, and references therein) and affect continuous GPS (CGPS) time series. A prominent tectonic mechanism that occurs at

many subduction type plate boundaries and can result in a deviation from a linear trend in GPS time series are slow slip events (SSEs) (e.g. Hirose *et al.*, 1999; Dragert *et al.*, 2001). A review of the process can be found in Schwartz and Rokosky (2007). To first order SSEs manifest themselves as quasi-periodic offsets in GPS time series (e.g. Szeliga *et al.*, 2008; Schmidt and Gao, 2010). Williams *et al.* (2004); Hackl *et al.* (2011) showed that uncorrected offsets in time series make the noise to appear more time correlated (in the case of white noise plus offset it is similar to random walk). In general transient signals occur in some preferred direction and affect regional networks of GPS time series. Therefore we developed an algorithm based on the Allan Variance of the rate (AVR) (Hackl *et al.*, 2011) that is capable of classifying time correlated noise for every chosen direction and used the results to calculate the variance and covariance of the rate along with the noise parameters. Based on this, we are able to identify sites in Costa Rica and Cascadia affected by transients and to draw conclusions on the quality of models accounting for SSEs.

4.2 Directional noise analysis

GPS time series provide the temporal variation of the antenna position and can be interpreted as long term rate, possibly including some time dependent effects (e.g. annual signals, post seismic relaxation, etc), and time correlated noise. Note that if the time dependent effects are not explicitly included in the analysis, they are implicitly considered to be part of the noise. In this paper we focus on the analysis of the noise to infer the uncertainty of the long term rate. The uncertainty is defined by the standard deviation σ , which is derived from the variance σ^2 and provides a confidence interval. In the following we assume only Gaussian distributed noise and refer to the standard deviation as the uncertainty. In the two dimensional case the confidence interval is represented by the confidence ellipse or error ellipse (in three dimensions it is the error ellipsoid). Most velocity vectors are drawn along with the 95% confidence ellipse, this also holds for this paper. The 2d representation of the variance is called variance ellipse and, unlike the confidence ellipse, for most applications it does not have a relevant physical meaning.

Following Strang and Borre (1997) the horizontal velocity variance can be expressed by the positive definite covariance matrix

4 VELOCITY COVARIANCE OF GPS TIME SERIES IN THE PRESENCE OF TRANSIENTS AND TIME CORRELATED NOISE

$$\Sigma = \begin{pmatrix} \sigma_1^2 & \sigma_{12} \\ \sigma_{12} & \sigma_2^2 \end{pmatrix} \quad (4.1)$$

where σ_1^2 and σ_2^2 are the variances in x_1 and x_2 direction and σ_{12} is the covariance. This is a positive-semidefinite matrix, thus it can be diagonalized by non-negative diagonal elements σ_{max}^2 and σ_{min}^2 and geometrically represented by a variance ellipse.

According to the law of error propagation (e.g. Bevington and Robinson, 2003), the velocity variance in direction φ defined by the unit vector $(\cos \varphi, \sin \varphi)^T$, is calculated by

$$\begin{aligned} \sigma^2(\varphi) &= (\cos \varphi, \sin \varphi) \begin{pmatrix} \sigma_1^2 & \sigma_{12} \\ \sigma_{12} & \sigma_2^2 \end{pmatrix} \begin{pmatrix} \cos \varphi \\ \sin \varphi \end{pmatrix} \\ &= \sigma_1^2 \cos^2 \varphi + 2\sigma_{12} \cos \varphi \sin \varphi + \sigma_2^2 \sin^2 \varphi \end{aligned} \quad (4.2)$$

This result can also be obtained by pure geometrical considerations based on the confidence ellipse. The principal semi-axes of the confidence ellipse represent the maximum and minimum velocity uncertainties σ_{max} and σ_{min} , respectively, or multiples of them. In the case of a two dimensional Gaussian distribution the probability of a velocity to fall inside the confidence ellipse can be calculated by

$$W = 1 - e^{-\frac{1}{2}k^2}, \quad (4.3)$$

where k indicates the multiple of σ that underlies the confidence ellipse.

The squares of σ_{max} and σ_{min} are the entries of the diagonalized form of Σ . The velocity uncertainty in any direction φ is given by the projection of the ellipse in that direction (Fig. 4.1). Thus the velocity uncertainty $\sigma(\varphi)$ is identical to the support function of an ellipse, the so-called pedal curve:

$$\sigma(\varphi) = \sqrt{\sigma_{max}^2 \cos^2(\varphi - \alpha) + \sigma_{min}^2 \sin^2(\varphi - \alpha)} \quad (4.4)$$

where α is the angle between x_1 -axis and the major semi-axis of the ellipse. This pedal curve is the locus of points, where any line from the origin intersects a perpendicular line that is tangent to the ellipse. It can be shown (e.g. Strang and Borre, 1997) that Eqn. (4.4) is also equivalent to Eqn. (4.2) if Σ is not diagonalized.

The antenna position at any solution can be projected into every direction by the dot product of the position vector and the unit vector of the chosen direction. In the horizontal 2d case the east and north components of the position time series can be used to compute the projected position in

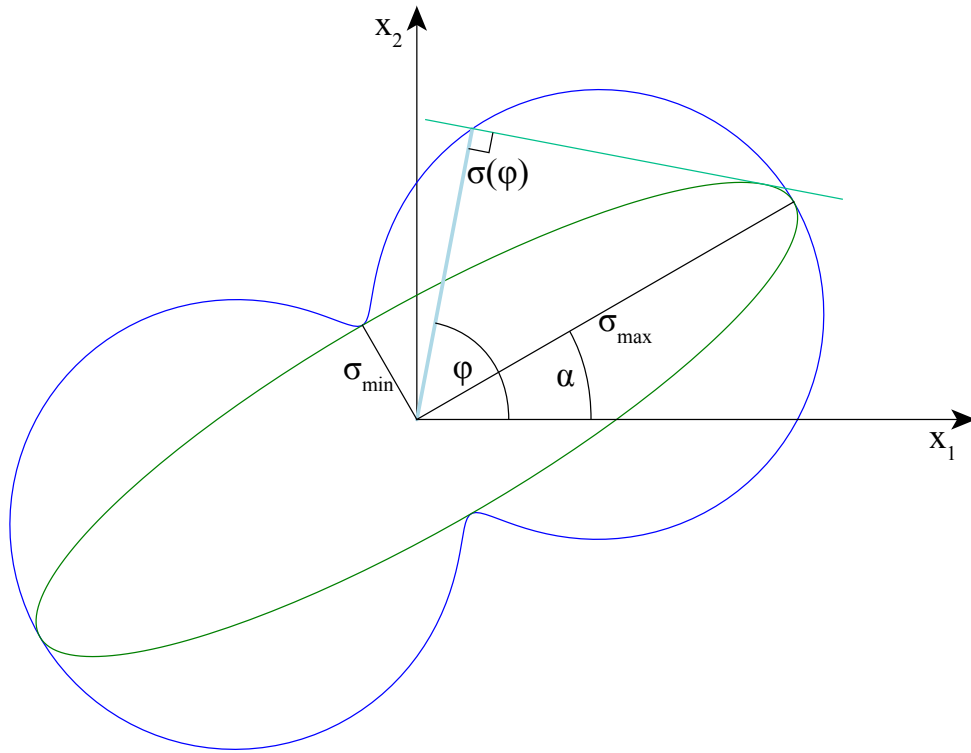


Figure 4.1: Confidence ellipse (green) and corresponding support function (blue).

4 VELOCITY COVARIANCE OF GPS TIME SERIES IN THE PRESENCE OF TRANSIENTS AND TIME CORRELATED NOISE

any given direction φ at each time. The resulting time series is used to calculate the corresponding velocity variance $\sigma^2(\varphi)$. If the velocity variance is known for at least three different horizontal directions φ , the full horizontal covariance matrix of the velocity can be obtained by inverting Eqn. (4.2). Of course, this analysis can easily be extended to three dimensions, considering six unknowns and Σ being a 3×3 matrix that is represented by an ellipsoid. Due to the law of error propagation the horizontal confidence ellipse is the projection of this 3d ellipsoid on to the horizontal plane.

In order to derive the horizontal covariance matrix we project the east and north components of a position time series into at least three different directions φ obtaining time series $\xi_\varphi(t)$. Then the velocity variance $\sigma^2(\varphi)$ is calculated for each time series by applying the Allan variance of the rate (AVR) (Hackl *et al.*, 2011) and fitting an adequate error model. By doing so it is possible to obtain different time correlation parameters for different directions. Finally, the covariance matrix is obtained by fitting Eqn. 4.2 to the different velocity variances. This process is also shown in more detail in Fig. 4.2.

4.3 Costa Rica

We analyzed the time series computed by Jiang *et al.* (2012) of twelve continuous GPS sites in Costa Rica, ten in the Nicoya peninsula and two close to the peninsula. The network was initiated in 2002 to study strain accumulation of slow slip events in the adjacent subduction zone (Outerbridge *et al.*, 2010) and completed in 2008. For each site the horizontal components of the time series were projected into 18 different horizontal directions and the AVR for every direction was calculated. Then we applied two different error models, (1) “white noise + flicker noise + random walk” and (2) “white noise + power law noise” to compute the variance of the rate for each of the 18 directions. These variances are then fitted using Eqn. (4.2) in order to obtain the 2d velocity covariance for the two different error models. As an example Fig. 4.2 (top) shows this process in more detail for site GRZA for the “white noise + power law noise” model. The blue dots correspond to the variances of the time series projected into directions varying of 10° in azimuth. These results are fitted using Eqn. 4.2 (green curve) and the principal components, which are graphically represented by the red variance ellipse, are estimated. The corresponding 1σ confidence ellipse (black) is presented in the lower part of Fig. 4.2 together with the function representing the pro-

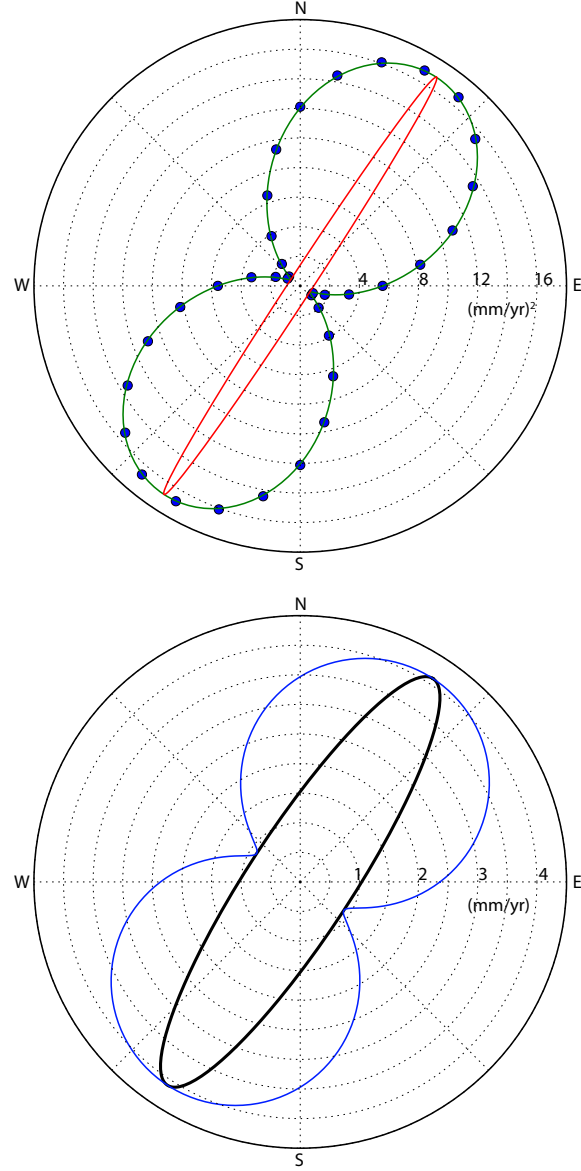


Figure 4.2: Horizontal velocity variances (top) of site GRZA based on a white noise plus power law noise error model. Blue dots represent the estimated variances for the different directions. These variances have been fitted (green curve) using Eqn. 4.2. Note, that the corresponding variance ellipse (red curve) represents the variance and not the uncertainty. The black ellipse (bottom) represents the 1σ confidence ellipse. The blue curve is the pedal curve and represents the actual 1σ uncertainty in any direction.

4 VELOCITY COVARIANCE OF GPS TIME SERIES IN THE PRESENCE OF TRANSIENTS AND TIME CORRELATED NOISE

jection of the uncertainty into all horizontal directions (pedal curve). The ellipse in Fig. 4.2 (bottom) shows the one sigma confidence ellipse (1σ uncertainty) and the projection of the uncertainty into all horizontal directions (blue pedal curve).

The results from the analysis of the Costa Rican sites are summarized in Tables 4.1 and 4.2, and in Figs. 4.4 and 4.5. It is interesting to note that the uncertainty estimates of the two different error models produce very similar results in terms of azimuth and magnitude of the confidence ellipse for most sites (black and red ellipses in Fig. 4.4). As observed by Hackl *et al.* (2011), the few cases with significantly different results correspond to sites where the chosen error model does not fit the AVR very well. Sites BON2, GRZA, LEPA, LMNL, PUMO, and QSEC show relatively large and eccentric velocity confidence ellipses with the major semi-axis oriented SW-NE. While the direction of the inter-seismic rate coincides well with the relative plate motion direction, the rate uncertainty is highest normal to the plate boundary, approximately rotated of 20 degrees to the east with respect to the relative plate motion direction. This is probably related to the fact that strain at this plate boundary is partitioned between a nearly normal component at the subduction zone and a trench parallel strike slip component in the back-arc associated with a fore-arc block (LaFemina *et al.*, 2009; Outerbridge *et al.*, 2010; Jiang *et al.*, 2012). A similar behavior is observed at many oblique subduction type plate boundaries (e.g. Fitch, 1972; McCaffrey, 1992).

Offsets and velocity changes in time series result in a noise pattern that is similar to highly time correlated noise (Williams, 2003a; Hackl *et al.*, 2011). If offsets occur in some preferred direction, an increased time correlation and therefore a larger uncertainty would be inferred in that particular direction. Hence, a possible explanation for the large eccentricities of the site velocity uncertainties are SSEs that can to first order be described as offsets (Brown *et al.*, 2005, 2009; Tryon, 2009; Outerbridge *et al.*, 2010; Davis *et al.*, 2011; Walter *et al.*, 2011). Jiang *et al.* (2012) identified five events close to the Nicoya peninsula during the period from 2002 to 2011.

The orientations of the major semi-axis of the uncertainty ellipses of the six above mentioned sites are in good agreement with the direction of the induced surface displacement due to the SSEs modeled by Jiang *et al.* (2012). Although the stations HATI, IND1, and PNEG present a similar pattern, their signals appear to be more complicated. Only HUA2 and PUJE show a different pattern with the major semi-axes being oriented N-S. These two sites lie in between two different patches that experience SSEs as indicated

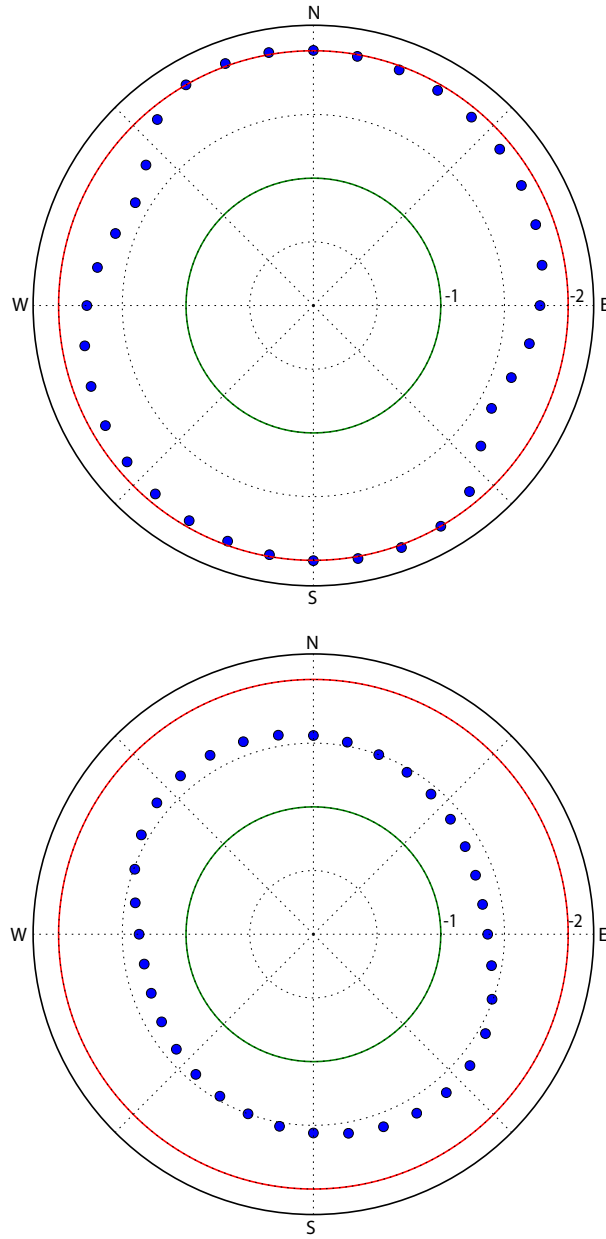


Figure 4.3: Spectral indices of GRZA (blue dots) that were estimated along with the variances (see Figure 4.2). Values far from the origin represent high time correlation. The green circle corresponds to flicker noise, the red circle to random walk. The spectral indices have been estimated from the raw time series (top) and from the residual time series after correcting for the SSEs (bottom).

4 VELOCITY COVARIANCE OF GPS TIME SERIES IN THE PRESENCE OF TRANSIENTS AND TIME CORRELATED NOISE

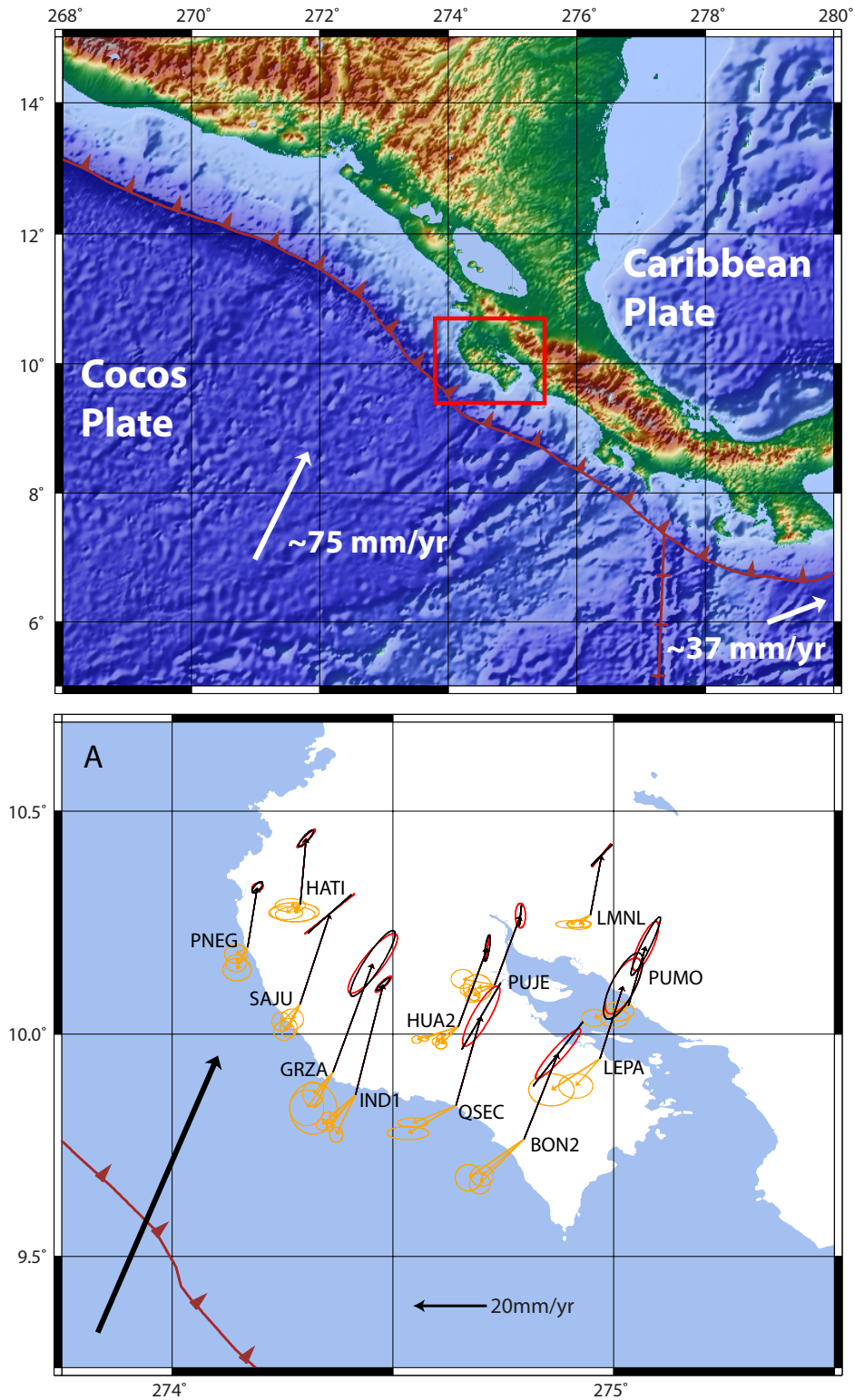
Table 4.1: Estimated noise amplitudes and 1σ velocity uncertainties in principal axis directions based on a "white noise + flicker noise + random walk" error model of continuous GPS sites in Costa Rica.

site	azimuth deg cw from N		principal axis	σ_v (mm/yr)		a_{wn} ($mm \cdot day^{0.5}$)		a_{fl} (mm)		a_{rw} ($mm/day^{0.5}$)	
	raw	res		raw	res	raw	res	raw	res	raw	res
BON2	41.88	46.65	max	3.50	0.90	2.17	1.84	0.00	1.58	0.46	0.11
			min	0.65	0.56	1.85	1.80	1.36	1.40	0.07	0.06
GRZA	38.72	31.07	max	3.95	1.27	1.76	1.53	1.29	1.62	0.47	0.14
			min	1.06	0.71	2.05	2.09	0.71	0.88	0.12	0.08
HATI	45.05	37.73	max	1.35	0.31	1.83	1.78	1.15	1.19	0.15	0.00
			min	0.23	0.26	1.92	2.04	1.15	0.98	0.00	0.00
HUA2	9.66	63.6	max	1.46	0.25	1.91	1.58	0.96	1.67	0.23	0.00
			min	0.01	0.17	1.67	1.89	1.55	1.10	0.00	0.00
IND1	45.22	50.15	max	1.17	0.31	1.94	2.17	2.35	2.09	0.17	0.00
			min	0.27	0.20	2.23	2.27	1.41	1.35	0.03	0.00
LEPA	28.38	36.52	max	3.29	0.32	1.83	1.57	0.00	1.24	0.39	0.00
			min	1.26	0.26	1.88	1.84	0.81	1.00	0.14	0.00
LMNL	39.44	-50.66	max	1.57	0.34	1.86	1.89	0.74	1.06	0.17	0.00
			min	0.01	0.30	1.84	1.81	1.17	0.94	0.00	0.00
PNEG	62.26	65.2	max	0.62	0.56	2.29	2.43	2.04	1.83	0.00	0.00
			min	0.42	0.41	2.39	2.41	1.38	1.35	0.00	0.00
PUJE	-0.66	-85.77	max	1.30	0.24	2.21	1.96	0.89	1.55	0.20	0.00
			min	0.53	0.19	1.93	2.12	1.59	1.21	0.07	0.01
PUMO	24.52	-79.83	max	2.83	0.39	1.77	1.65	0.00	1.20	0.29	0.00
			min	0.77	0.37	1.60	1.55	1.28	1.13	0.05	0.00
QSEC	29.93	28.78	max	3.62	1.27	2.11	1.64	0.00	1.66	0.43	0.14
			min	0.90	0.31	2.12	2.12	1.02	1.03	0.10	0.02
SAJU	51.28	62.12	max	3.38	0.57	1.73	1.71	1.20	1.43	0.32	0.00
			min	0.01	0.43	1.74	1.87	1.36	1.06	0.00	0.00

Table 4.2: Estimated power law indices and 1σ velocity uncertainties in principal axis directions based on a “white noise + power law noise” error model of continuous GPS sites in Costa Rica.

site	azimuth deg cw from N		principal axis	σ_v (mm/yr)		power law index	
	raw	res		raw	res	raw	res
BON2	37.8	41.57	max	4.30	0.82	-2.16	-1.42
			min	0.01	0.52	-1.28	-1.29
GRZA	33.15	14.83	max	4.10	1.12	-2.02	-1.62
			min	0.88	0.66	-1.61	-1.35
HATI	41.56	57.72	max	1.13	0.36	-1.60	-1.16
			min	0.30	0.11	-1.15	-0.57
HUA2	8.79	21.24	max	1.37	0.21	-1.91	-0.98
			min	0.23	0.12	-1.38	-0.74
IND1	46.53	40.79	max	0.94	0.28	-1.43	-0.93
			min	0.20	0.10	-0.93	-0.65
LEPA	26.98	6.08	max	3.88	0.33	-2.14	-1.04
			min	1.24	0.12	-1.82	-0.57
LMNL	44.59	70.46	max	1.58	0.13	-2.02	-0.56
			min	0.01	0.12	-1.18	-0.33
PNEG	42.96	65.73	max	0.73	0.24	-1.13	-0.51
			min	0.34	0.14	-0.82	-0.36
PUJE	5.53	29.9	max	1.14	0.27	-1.80	-1.17
			min	0.01	0.08	-1.04	-0.64
PUMO	26.05	15.26	max	3.42	0.22	-2.32	-0.73
			min	0.47	0.15	-1.63	-0.48
QSEC	30.34	25.97	max	4.08	1.20	-2.14	-1.58
			min	0.01	0.39	-1.42	-1.20
SAJU	48.68	44.76	max	3.05	0.31	-1.82	-0.63
			min	0.01	0.13	-0.98	-0.32

4 VELOCITY COVARIANCE OF GPS TIME SERIES IN THE PRESENCE OF TRANSIENTS AND TIME CORRELATED NOISE



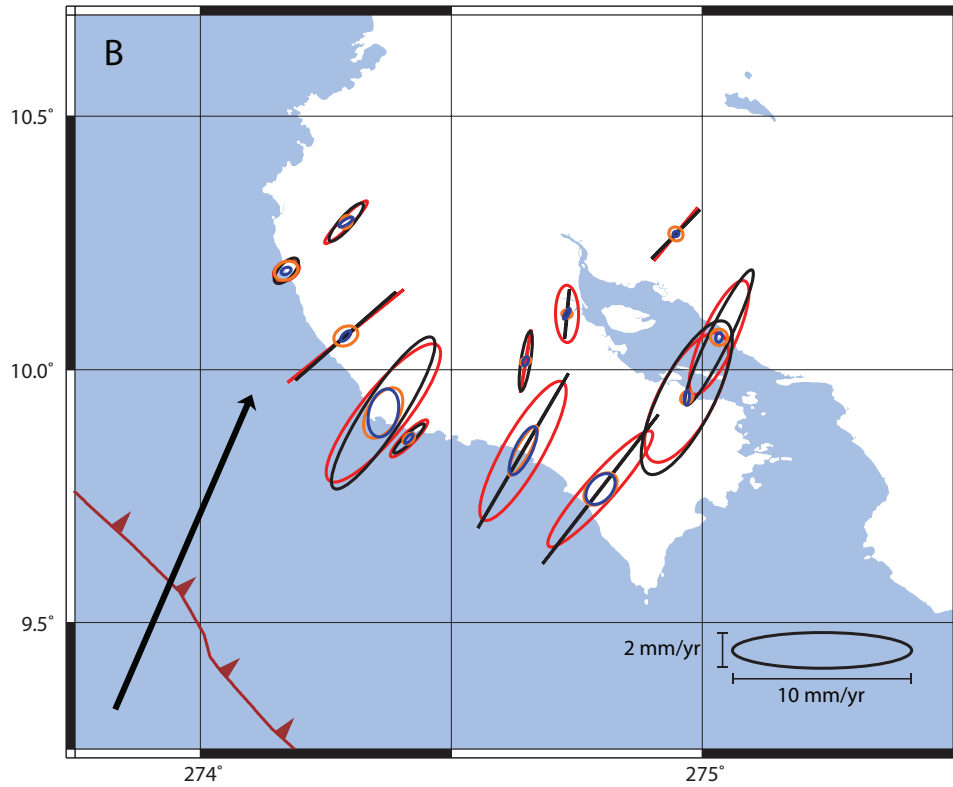


Figure 4.4: Figure of the Nicoya peninsula, Costa Rica, with interseismic GPS velocity field. All velocities are with respect to a fixed Carribean Plate. (A) shows 95% velocity confidence ellipses using the raw time series, where red ellipses are based on a “white noise + flicker noise + random walk” error model, and black ellipses on a “white noise + power law” error model. Orange arrows indicate horizontal displacements during the SSE according to Jiang *et al.* (2012). (B) shows the 95% confidence ellipses of the velocities (black and red ellipses are the same than in (A)) in a larger scale. Orange and blue ellipses represent the 95% confidence ellipses of the rates (“white noise + flicker noise + random walk”: orange; “white noise + power law noise”: blue) based on the residual time series, after subtracting the SSE modeled by Jiang *et al.* (2012) from the time series.

4 VELOCITY COVARIANCE OF GPS TIME SERIES IN THE PRESENCE OF TRANSIENTS AND TIME CORRELATED NOISE

by the large scatter of directions for the model SSE, which also reflects in a broad scatter of directions for the modeled SSE displacements.

To test the possibility that the orientation of the ellipses is controlled by the high time correlated noise introduced by the SSE, we subtract from each time series the corresponding surface displacements caused by SSEs as modeled by Jiang *et al.* (2012). The corrected velocity variances do not indicate the presence of a preferred orientation anymore, but the ellipses seem to become more circular instead, indicating that a significant portion of the apparent time correlation in the time series is explained by transients present in the time series. This is also confirmed by the noise characteristics of the raw time series and the corrected time series for each direction. In the case of the “white noise + flicker noise + random walk” error model the raw time series exhibit a significant amount of random walk that is drastically reduced in the corrected time series (Table 4.1). A similar conclusion can be drawn from the “white noise + power law noise” error model, where the spectral index (measure of time correlation) that is estimated along with uncertainty is significantly smaller (higher time correlation) in the case of the uncorrected time series, especially in the directions of the SSEs (Table 4.2 and Fig. 4.5). These results are also summarized in Fig. 4.4 (B), where the 95% confidence ellipses of the velocities are shown. The residual time series, after subtracting the SSEs, show less eccentricity (blue and orange ellipses) compared to the raw time series (black and red ellipses).

4.4 PANGA

If the presence of SSE in Costa Rica is the principal factor in the eccentricity of the confidence ellipses a similar behavior should be observed in other regions affected by SSE as the Cascadia subduction zone. Among others, Dragert *et al.* (2001); Miller *et al.* (2002); Rogers and Dragert (2003) describe SSEs accompanied by non volcanic tremor at this plate boundary, where the Juan de Fuca plate is subducted beneath the North American plate at a rate of $\sim 38\text{mm/yr}$. 34 SSEs between 1997 and 2005 have been characterized by Szeliga *et al.* (2008) using GPS data. The events occurred at Puget Sound and south of the Sound down to $\sim 46^\circ$ North. The region is covered by ~ 600 continuously operating GPS sites providing the possibility to analyze the spatial distribution of transients.

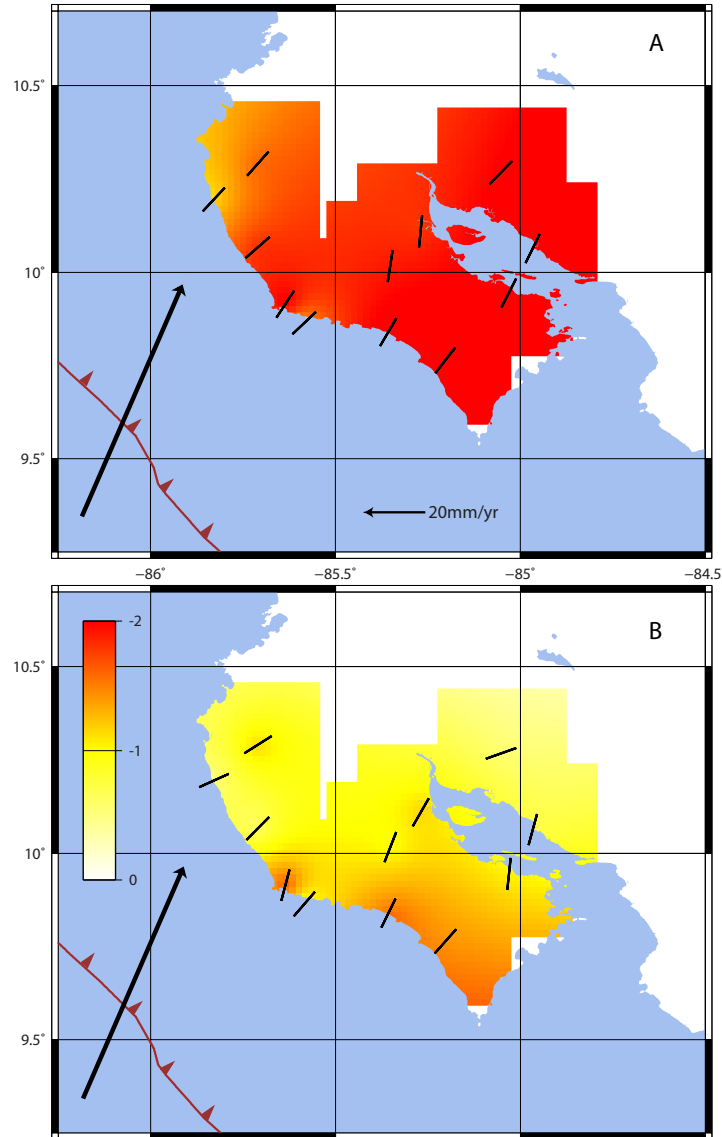


Figure 4.5: Interpolated fields of the estimated spectral indices (see colorbar) in direction of the highest time correlation (black bars). A spectral index of -1 corresponds to flicker noise, -2 to random walk. (A) shows the spectral indices calculated from the cleaned time series (corrected for trends, offsets, annual, and semiannual signals). (B) is based on time series that have additionally been corrected for modeled SSEs.

4 VELOCITY COVARIANCE OF GPS TIME SERIES IN THE PRESENCE OF TRANSIENTS AND TIME CORRELATED NOISE

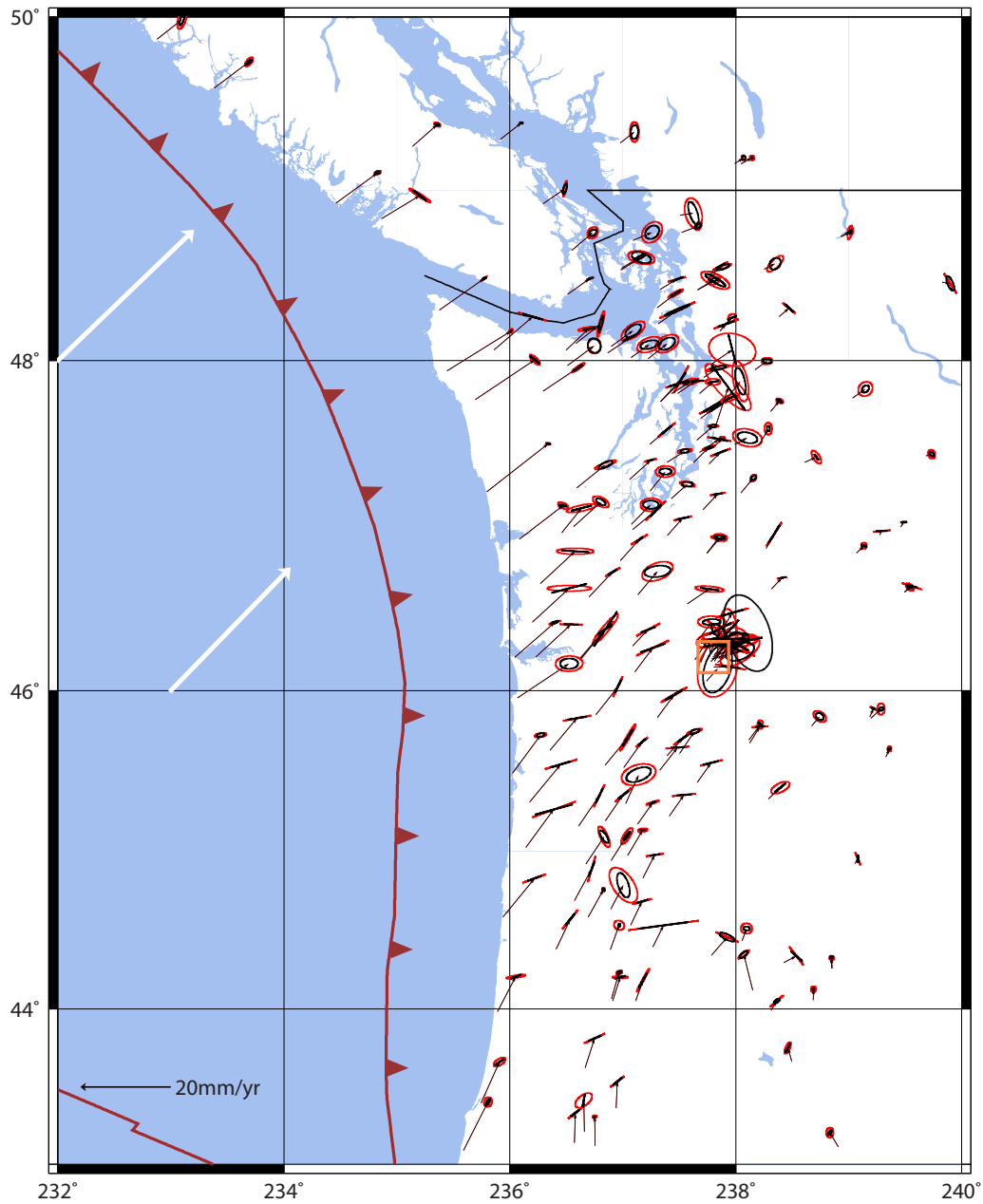


Figure 4.6: PANGA GPS interseismic velocity field with 95% confidence ellipses calculated using a “white noise + power law noise” error model (black) and a “white noise + flicker noise + random walk” error model (red). Red arrows indicate plate motions with respect to stable North America. The orange rectangular indicates the position of Mount St. Helens (see Fig. 4.8)

We applied the same analysis we did for the Costa Rica sites to all time series of the PANGA (Pacific Northwest Geodetic Array¹) network with more than 4 years of data (Fig. 4.6). As expected, many coastal sites show uncertainty ellipses that are elongated almost perpendicular to the plate boundary, similar to the observation in Costa Rica. Inbound sites have ellipses that are elongated aligned to the relative plate motion direction. Uncertainty ellipses of sites further to the east, close to the volcanic arc are oriented mainly E-W again. Sites south and east of the area affected by SSEs have in general smaller uncertainties with randomly distributed principal axes.

For the “white noise + power law noise” error model we estimated the spectral indices of the power law noise along with the uncertainties. Fig. 4.7 shows an interpolation of the smallest spectral index (highest time correlation) and the corresponding directions. For this analysis we excluded the sites around Mount St. Helens since the volcanic activity is likely to mask the effects of SSEs (these sites are analyzed in Section 4.5). Fig. 4.7 A shows the spectral index for detrended time series corrected for known offsets and filtered from annual and semiannual signals. Usually, GPS time series that are not affected by transients exhibit a power law noise that is close to flicker noise ($\nu = -1$) (e.g. Mao *et al.*, 1999; Hackl *et al.*, 2011). However, most of the sites in this region affected by SSEs show time correlated noise close to random walk ($\nu = -2$).

The geodetic group at the Central Washington University (T. Melbourne pers. comm., 29 November 2011) measured the offsets in the time series caused by 20 SSEs between 1997 and 2011 and modeled the surface displacements caused by these events. The analysis of the spectral index for the time series corrected for the modeled surface displacement or the measured offset are presented in Fig. 4.7 B and C, respectively. In both cases the time correlation of the noise in the regions affected by SSE is reduced significantly. Some sites, however, show still relatively high time correlation. This is especially true for the sites close to the coast of Puget Sound. A part for the obvious possibility of an incomplete correction of the effects due to SSEs, a very likely reason for high time correlated noise in this region is the presence of transient effects due to the $M_w = 6.8$ Nisqually earthquake in 2001. It is intriguing that the region where the spectral index is not reduced to flicker noise is highly correlated with the area mostly affected by surface displacement during the earthquake (Bustin *et al.*, 2004). This

¹<http://www.geodesy.cwu.edu/>

4 VELOCITY COVARIANCE OF GPS TIME SERIES IN THE PRESENCE OF TRANSIENTS AND TIME CORRELATED NOISE

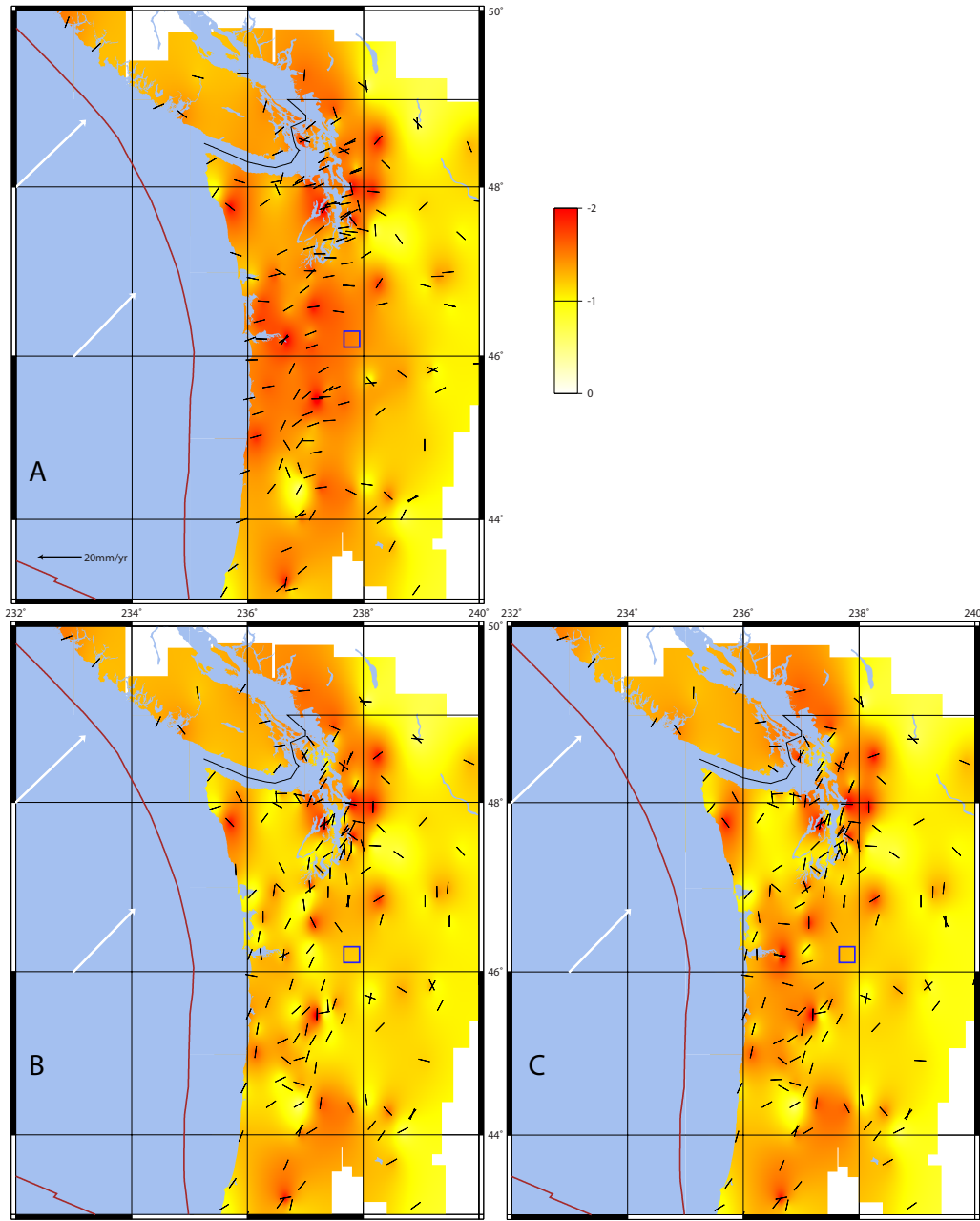


Figure 4.7: Interpolated fields of the estimated spectral indices (see colorbar) in direction of the highest time correlation (black bars). (A) shows the spectral indices calculated from the cleaned time series (corrected for trends, offsets, annual, and semiannual signals). (B) is based on time series that have additionally been corrected for 20 modeled SSEs. (C) is based on time series that have been corrected for the measured offsets during the SSEs.

would also be the region more affected by post-seismic relaxation. It is very likely that the high time correlated noise in these time series after the correction for the SSE do reflect this transient phenomena. Another source of crustal deformation in that region is glacial isostatic adjustment (James *et al.*, 2000).

4.5 Mount St. Helens

Mount St. Helens is the most active strato-volcano in the Cascade volcanic arc (e.g. Scott *et al.*, 2008). It experienced a dome building eruption in 2004 and ongoing activity until 2010. The associated ground deformation was measured by GPS (Dzurisin *et al.*, 2008; Lisowski *et al.*, 2008; Palano *et al.*, 2012). Lava extruded building a dacite dome during the first part of the unrest. The associated deflation of a magma chamber caused surrounding GPS sites to move towards the center of the volcano. Subsequently, the magma chamber was filled up again causing a complex pattern of inflation.

We analyzed time series that were not corrected for any volcanic induced transients applying the method introduced above. Results are summarized in Fig. 4.8. Black arrows show the inter-seismic long term rates with 95% confidence ellipses (red ellipses). This region is affected by SSEs despite the distance from the plate boundary. Close to Mt. St. Helens however, the situation is more complex due to different phases of volcanic activity. As an example, the green arrows in Fig. 4.8 represent modeled horizontal velocities in a local reference frame during the deflation phase. Most confidence ellipses are clearly affected and show significant uncertainties radial to the center of Mt. St. Helens. These deflation velocities are supposed to have an effect on the long term velocities distorting the confidence ellipses. However, the velocities and their confidence ellipses are also affected by the inflation and the subduction related transients (see Section 4.4). Additionally, the GPS antennas are affected by snow accumulation.

Many GPS time series are affected by time dependent signals. Those signals can be caused by a variety of sources including tectonic related transients and time correlated noise. The analysis of transients provides insights to processes like post-seismic relaxation, SSEs, and volcanic deformation. The tectonic mechanisms usually result in a high time correlation (similar to a random walk process) in some preferred direction associated with large and highly eccentric velocity confidence ellipses. Additionally, tectonic related transients often show a spatial correlation in dense GPS networks.

4 VELOCITY COVARIANCE OF GPS TIME SERIES IN THE PRESENCE OF TRANSIENTS AND TIME CORRELATED NOISE

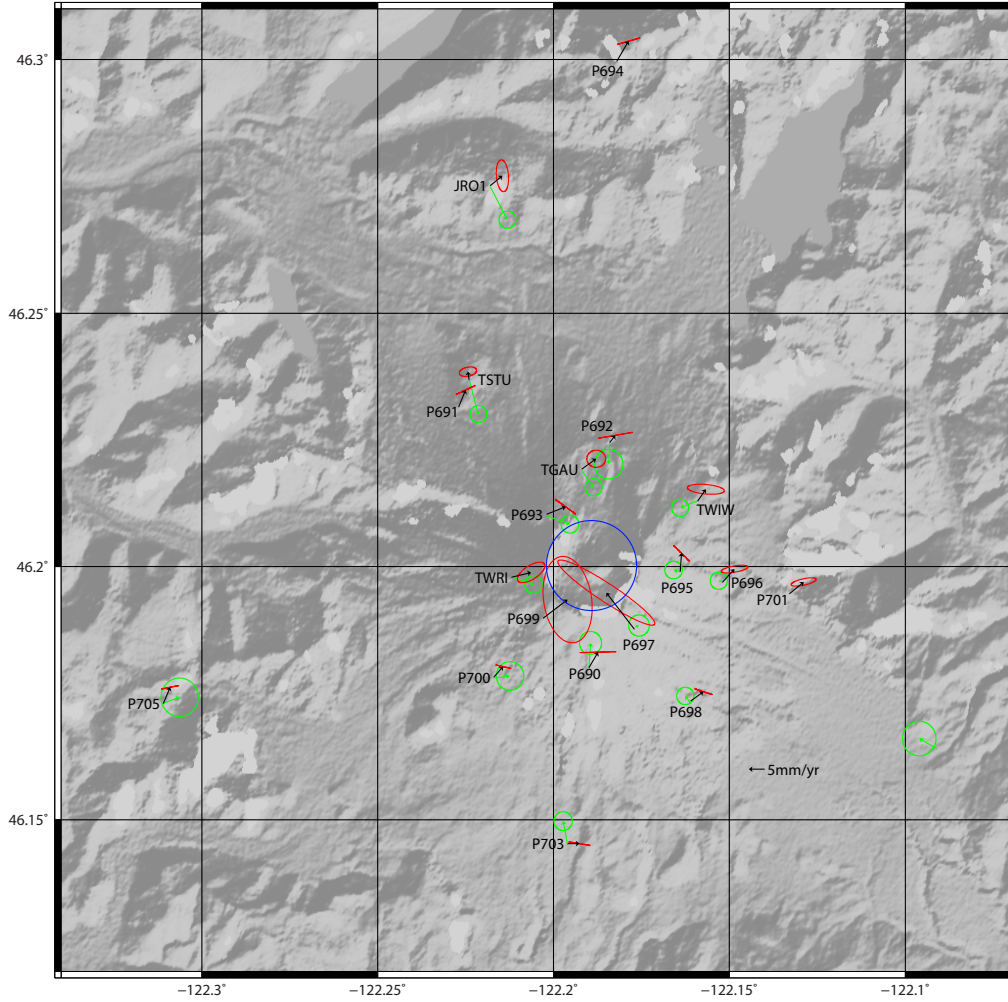


Figure 4.8: Interseismic horizontal GPS velocities (black arrows) at the Mount St. Helens volcano in a stable North America reference frame. Red ellipses show the 95% confidence ellipses of the rates based on a “white noise + flicker noise + random walk” error model (red). The green arrows show the modeled site velocities during a deflation period Oct. 2004 - Oct. 2005 in a local reference frame (Lisowski *et al.*, 2008). The blue circle indicates the position of the caldera.

In order to analyze the directional dependence of time correlated noise in GPS time series, we computed the velocity covariance from GPS time series. The full covariance of the rate of GPS time series is obtained by projecting the position time series into different horizontal directions, applying the Allan variance of the rate for every direction in order to estimate the velocity variance in this direction, and fit Eqn. 4.2 to the variances. This method is easy to implement, accounts for time correlated noise, and allows for different noise characteristics for different directions.

Most GPS sites in Costa Rica and Cascadia that experience SSEs have velocity confidence ellipses which are elongated in the direction of known transient events as SSEs. After subtracting models that account for the transients from the time series, the confidence ellipses are significantly less eccentric. This indicates that SSEs account for a large portion of the apparent time correlated “noise” in the analyzed networks. Time series not affected by or corrected for transients show a dominant time correlation close to flicker noise. A similar behavior, although in a more complex context, can be observed at Mount St. Helens due to volcanic deformation.

Accurate GPS velocity estimates are necessary in order to provide confidence intervals of any model that is based on GPS velocities. Furthermore, the examples of Costa Rica and Cascadia demonstrate the importance of the full covariance in networks that are affected by transients, which result in a spatial correlation of the time correlation. For example, if the Costa Rica data are used to compute the rotation of Nicoya peninsula, the confidence interval of the Euler pole is significantly affected by the unidirectional GPS velocity confidence ellipses. The importance of the orientation of highly eccentric error ellipses can also be exemplified by the analysis of the residuals of slowly deforming regions. In these regions the deformation signal is often of the same magnitude than the uncertainties. In those cases the presence of a signal is inferred by a non-random distribution of the azimuth of the residuals (e.g. Plattner *et al.*, 2007; Malservisi *et al.*, 2012). While this observation is reasonable in the case of isotropic error ellipses, a bias might be introduced in the case of spatially coherent eccentric error ellipses. In the latter case, the observed “noise” has a preferred direction implying that also the residuals could present a preferred orientation without to represent a signal.

4.6 Acknowledgments

We used data of the Pacific Northwest Geodetic Array provided by the Central Washington University. We are grateful to Tim Melbourne and the geodetic group of the Central Washington University for providing the surface displacement data due to the slow slip events. We would like to thank Tim Dixon for his comments that helped to improve this manuscript. This research was funded by the Bavarian Elite Network and the DFG grant BA1210/18-1.

5

Conclusion and Outlook

An increasing number of GPS receivers, the improving accuracy of the position measurement, and the deployment of new GNSS systems like GLONASS, Galileo, and Beidou provide continuously improving opportunities for earth sciences. Some of the principal challenges consist in extracting the information that is related to tectonics, drawing conclusions on crustal deformation rates, and characterizing the noise in order to separate it from the signal. The principal goal of this thesis is to contribute to different aspects of the application of GPS measurements in tectonics. In a first part I set up an algorithm to derive the continuous 2d strain rate tensor from dense GPS networks. Then I developed a method to estimate realistic velocity uncertainties in the presence of time correlated noise. Subsequently, I implemented an algorithm to obtain the full GPS velocity covariance. The results of these three methods are discussed in the following.

In chapter 2 (Hackl *et al.*, 2009) I developed a method that provides the continuous 2d strain rate tensor and its characteristics such as the maximum shear strain rate, the rotation and dilatation strain rates. It has been shown that active structures can be identified by the method, which does not require any additional information such as the fault geometry, and that the estimated strain rates are in good agreement with independently calculated values (Sandwell *et al.*, 2010). Furthermore, the algorithm is also capable to

infer fault rupture characteristics, when applied to co-seismic and or post-seismic displacement vectors. Additionally, it has been shown in the context of this work that many GPS velocity fields are biased by transient signals. On the one hand the presence of biases due to transient behavior implies that the error budget in GPS time series has to be estimated including time dependent effects, on the other hand the transient signals provide important information, if the transients can be modeled properly. Those aspects were addressed in the subsequent work. Future work on further development of the strain rate analysis may include the use of the vertical component, the integration of other geodetic techniques like InSAR, and the temporal evolution of the strain rate field along with realistic confidence estimates.

In chapter 3 (Hackl *et al.*, 2011), I developed a method to characterize the noise content of GPS time series in the presence of time correlated noise. This algorithm is based on the Allan variance, which is widely used in the estimation of oscillator stability and can be applied in the presence of time correlated noise. A lot of emphasis was placed on thorough testing with synthetic time series and the effect of different kinds of noise on the Allan variance of the rate (AVR). The robust and fast algorithm, which does not require spectral analysis in the frequency domain, was tested on the South African TrigNet network and the results were compared against the ones obtained by a maximum likelihood estimation based method. However, this algorithm provides a lot of possibilities for further expansions. In a first step the effect of a temporal change of the time correlated noise on the AVR may be analyzed. Due to advancing models, the repeatability of GPS position measurements continuously improves. This may also reflect in the velocity uncertainty. Another possible enhancement can address current and future developments in high rate GPS and the related necessity of real time noise analysis. A possible “dynamic AVR” can provide an important contribution.

Finally, in chapter 4 I implemented an algorithm to obtain the full velocity covariance from GPS time series (Hackl *et al.*, 2012). This provides realistic velocity uncertainty confidence intervals in the presence of time correlated noise. The uncertainties are important for models that are based on GPS rates and form the basis of confidence estimates of any information derived from GPS velocities. I showed that GPS networks at subduction zones can be significantly affected by transients caused by slow slip events, which result in spatially correlated highly eccentric error ellipses. Subtracting the modeled displacements of those events from the time series, reduces

significantly the eccentricity. Thus, the covariance analysis is particularly useful in the detection of transient signals in GPS time series and can provide an independent measure of the model quality. A thorough analysis of different GPS networks along with statistical characterizations of different effects caused by tectonic and tropospheric settings are possible topics to be addressed in future studies. Finally, the development is clearly heading towards more complex velocity models that account not only for the long term rate, but also for a number of time dependent mechanisms. Models of those time dependent effects will improve dramatically our understanding of many processes in the system earth.

References

- Agnew, D. C.** (1992). The time-domain behavior of power-law noises. *Geophysical Research Letters*, **19**(4), 333–336. 3.2, 3.3.1, 3.3.1
- Allan, D. W.** (1966). Statistics of Atomic Frequency Standards. *Proceedings of the IEEE*, **54**(2), 221–230. 3.1, 3.2, 3.2, 3.3.1
- Allan, D. W.** (1987). Should the classical variance be used as a basic measure in standards metrology? *IEEE Transactions on Instrumentation Measurement*, **36**, 646–654. 3.2
- Allmendinger, R. W., Reilinger, R., and Loveless, J.** (2007). Strain and rotation rate from GPS in Tibet, Anatolia, and the Altiplano. *Tectonics*, **26**(TC3013). 2.2.1
- Árnadóttir, T., Hreinsdóttir, S., Gudmundsson, G., Einarsson, P., Heinert, M., and Völksen, C.** (2001). Crustal Deformation Measured by GPS in the South Iceland Seismic Zone Due to Two Large Earthquakes in June 2000. *Geophysical Research Letters*, **28**(21), 40314033. 2.3.6
- Atwater, T. and Stock, J.** (1988). Pacific-North America Plate Tectonics of the Neogene Southwestern United States - An Update. *International Geological Review*, **40**, 375–402. 2.3.1
- Barnes, J. A.** (1966). Atomic Timekeeping and the Statistics of Precision Signal Generators. *Proceedings of the IEEE*, **54**(2), 207–220. 3.1, 3.2
- Bawden, G. W., Thatcher, W., Stein, R. S., Hudnut, K. W., and Peltzer, G.** (2001). Tectonic contraction across Los Angeles after removal of groundwater pumping effects. *Nature*, **412**(6849). 4.1
- Beavan, J. and Haines, J.** (2001). Contemporary horizontal velocity and strain rate fields of the Pacific-Australian plate boundary zone through New Zealand. *Journal of Geophysical Research*, **106**(B1), 741–770. 2.2.1

REFERENCES

- Bennett, R. A., Rodi, W., and Reilinger, R. E.** (1996). Global Positioning System constraints on fault slip rates in southern California and northern Baja, Mexico. *Journal of Geophysical Research*, **101**, 21943–21960. 2.3.1
- Bevington, P. and Robinson, D.** (2003). *Data reduction and error analysis for the physical sciences*. McGraw-Hill Higher Education. McGraw-Hill. 4.2
- Blewitt, G. and Lavallée, D.** (2002). Effect of annual signals on geodetic velocity. *Journal of Geophysical Research*, **107**(2145). 3.3.3, 3.3.3, 3.3.3
- Bos, M., Bastos, L., and Fernandes, R.** (2010). The influence of seasonal signals on the estimation of the tectonic motion in short continuous GPS time-series. *Journal of Geodynamics*, **49**, 205–209. 3.3.3
- Bos, M. S., Fernandes, R. M. S., Williams, S. D. P., and Bastos, L.** (2008). Fast error analysis of continuous GPS observations. *Journal of Geodesy*, **82**(3), 157–166. 3.1, 3.2, 3.3.1, 3.4, 3.5
- Bracewell, R.** (1965). *The Fourier Transform and its Applications*. McGraw-Hill, New York. 3.3.1
- Brown, J. R., Beroza, G. C., Ide, S., Ohta, K., Shelly, D. R., Schwartz, S. Y., Rabbel, W., Thorwart, M., and Kao, H.** (2009). Deep low-frequency earthquakes in tremor localize to the plate interface in multiple subduction zones. *Geophysical Research Letters*, **36**(L19306). 4.3
- Brown, K. M., Tryon, M. D., DeShon, H. R., Dorman, L. M., and Schwartz, S. Y.** (2005). Correlated transient fluid pulsing and seismic tremor in the Costa Rica subduction zone. *Earth and Planetary Science Letters*, **238**(12). 4.3
- Bürgmann, R. and Dresen, G.** (2008). Rheology of the Lower Crust and Upper Mantle: Evidence from Rock Mechanics, Geodesy, and Field Observations. *Annual Review of Earth and Planetary Sciences*, **36**, 531–567. 4.1
- Bürgmann, R., Kogan, M., Levin, V., Scholz, C., King, R., and Steblov, G.** (2001). Rapid aseismic moment release following the 5 december, 1997 Kronotsky, Kamchatka, earthquake. *Geophysical Research Letters*, **28**(7), 13311334. 2.3.4

- Bustin, A., Hyndman, R. D., Lambert, A., Ristau, J., He, J., Dragert, H., and Van der Kooij, M.** (2004). Fault Parameters of the Nisqually Earthquake Determined from Moment Tensor Solutions and the Surface Deformation from GPS and InSAR. *Bulletin of the Seismological Society of America*, **94**(2), 363–376. 4.4
- Cai, J. and Grafarend, E. W.** (2007). Statistical analysis of geodetic deformation (strain rate) derived from the space geodetic measurements of BIFROST Project in Fennoscandia. *Journal of Geodynamics*, **43**(2), 214–238. 2.2.1
- Caporali, A.** (2003). Average strain rate in the Italian crust inferred from a permanent GPS network - I. Statistical analysis of the time-series of permanent GPS stations. *Geophysical Journal International*, **155**(6), 241–253. 3.1
- Dach, R., Hugentobler, U., Fridez, P., and Meindl, M.** (2007). *Bernese GPS Software Version 5.0*. User manual, Astronomical Institute, University of Bern. 3.4
- Davis, E., Heesemann, M., and Wang, K.** (2011). Evidence for episodic aseismic slip across the subduction seismogenic zone off Costa Rica: CORK borehole pressure observations at the subduction prism toe. *Earth and Planetary Science Letters*, **306**(34). 4.3
- Dixon, T., Decaix, J., Farina, F., Furlong, K., Malservisi, R., Bennett, R., Suarez-Vidal, F., Fletcher, J., and Lee, J.** (2002). Seismic cycle and rheological effects on estimation of present-day slip rates for the Agua Blanca and San Miguel-Vallecitos faults, northern Baja California, Mexico. *Journal of Geophysical Research*, **107**(B10). 2.3.2
- Dixon, T. H.** (1991). An introduction to the Global Positioning System and some geological applications. *Reviews of Geophysics*, **29**, 249–276. 3.1, 4.1
- Dixon, T. H., Robaudo, S., Jeffrey Lee, J., and Reheis, M. C.** (2000). Present-day motion of the Sierra Nevada block and some tectonic implications for the Basin and Range province, North American Cordillera. *Tectonics*, **14**(4), 755–772. 2.3.4, 3.1
- Dong, D., Fang, P., Bock, Y., Webb, F., Prawirodirdjo, L., Kedar, S., and Jamason, P.** (2006). Spatiotemporal filtering using

REFERENCES

- principal component analysis and Karhunen-Loeve expansion approaches for regional GPS network analysis. *Journal of Geophysical Research*, **111**(B03405). 4.1
- Dow, J. M., Neilan, R. E., and Rizos, C.** (2009). The International GNSS Service in a changing landscape of Global Navigation Satellite Systems. *Journal of Geodesy*, **83**, 191198. 3.4
- Dragert, H., Wang, K., and James, T. S.** (2001). A Silent Slip Event on the Deeper Cascadia Subduction Interface. *Science*, **292**(5521), 1525–1528. 4.1, 4.4
- Dzurisin, D.** (2003). A comprehensive approach to monitoring volcano deformation as a window on the eruption cycle. *Reviews of Geophysics*, **41**(1001). 4.1
- Dzurisin, D., Lisowski, M., Poland, M. P., Sherrod, D. R., and LaHusen, R. G.** (2008). Constraints and Conundrums Resulting from Ground-Deformation Measurements Made During the 2004-2005 Dome-Building Eruption of Mount St. Helens, Washington. In D. R. Sherrod, W. E. Scott, and P. H. Stauffer, Herausgeber, *A Volcano Rekindled: The Renewed Eruption of Mount St. Helens, 2004-2006*, chapter 14, Seiten 281–300. USGS Professional Paper 1750. 4.5
- Fernandes, R. M. S., Miranda, J. M., Meijninger, B. M. L., Bos, M. S., Noomen, R., Bastos, L., Ambrosius, B. A. C., and Riva, R. E. M.** (2007). Surface velocity field of the Ibero-Maghrebien segment of the Eurasia-Nubia plate boundary. *Geophysical Journal International*, **169**, 315–324(10). 2.2.1
- Fitch, T. J.** (1972). Plate convergence, transcurrent faulting, and internal deformation adjacent to Southeast Asia and the western Pacific. *Journal of Geophysical Research*, **77**(23), 4432–4460. 4.3
- Frank, F. C.** (1966). Deduction of earth strains from survey data. *Bulletin of the Seismological Society of America*, **56**(1), 35–42. 2.2.1
- Hackl, M., Malservisi, R., and Wdowinski, S.** (2009). Strain patterns from dense GPS networks. *Natural Hazards and Earth System Sciences*, **9**(4), 1177–1187. 2.3.2, 2.3.3, 3.1, 4.1, 5

- Hackl, M., Malservisi, R., Hugentobler, U., and Wonnacott, R.** (2011). Estimation of velocity uncertainties from GPS time series: Examples from the analysis of the South African TrigNet network. *Journal of Geophysical Research*, **116**(B11404). 4.1, 4.2, 4.3, 4.3, 4.4, 5
- Hackl, M., Malservisi, R., Hugentobler, U., and Jiang, Y.** (2012). Velocity Covariance of GPS Time Series in the Presence of Transients and Time Correlated Noise. *submitted to Geophysical Journal International*. 5
- Haines, A., Jackson, J., Holt, W., and Agnew, D.** (1998). Representing distributed deformation by continuous velocity fields. *Institute of Geological and Nuclear Sciences - Science Report*, **98/5**. 2.2.1
- Hammond, W., Kreemer, C., Blewitt, G., and Plag, H.-P.** (2010). Effect of viscoelastic postseismic relaxation on estimates of interseismic crustal strain accumulation at Yucca Mountain, Nevada. *Geophysical Research Letters*, **37**(L06307). 4.1
- Hill, E. M., Davis, J. L., Elósegui, P., Wernicke, B. P., Malikowski, E., and Niemi, N. A.** (2009). Characterization of site-specific GPS errors using a short-baseline network of braced monuments at Yucca Mountain, southern Nevada. *Journal of Geophysical Research*, **114**(B11402). 3.1
- Hirose, H., Hirahara, K., and Kimata, F.** (1999). A slow thrust slip event following the two 1996 Hyuganada earthquakes beneath the Bungo Channel, southwest Japan. **26**(21), 3237–3240. 4.1
- Howe, D. A., Allan, D. W., and Barnes, J. A.** (1981). Properties of Signal Sources and Measurement Methods. In *Proceedings of the 35th Annual Symposium on Frequency Control*. 3.2
- Jade, S. and Vijayan, M. S. M.** (2008). GPS-based atmospheric precipitable water vapor estimation using meteorological parameters interpolated from NCEP global reanalysis data. *Journal of Geophysical Research*, **113**(D03106), 1–12. 4.1
- Jamason, P., Bock, Y., Fang, P., Gilmore, B., Malveaux, D., Prawirodirdjo, L., and Scharber, M.** (2004). SOPAC Web site (<http://sopac.ucsd.edu>). *GPS Solutions*, **8**(4), 272–277. 2.3.2

REFERENCES

- James, T. S., Clague, J. J., Wang, K., and Hutchinson, I.** (2000). Postglacial rebound at the northern Cascadia subduction zone. *Quaternary Science Reviews*, **19**, 1527–1541. 4.4
- Ji, K. H. and Herring, T. A.** (2011). Transient signal detection using GPS measurements: Transient inflation at Akutan volcano, Alaska, during early 2008. *Geophysical Research Letters*, **38**(L06307). 4.1
- Jiang, Y., Wdowinski, S., Dixon, T. H., Hackl, M., Protti, M., and Gonzalez, V.** (2012). Slow Slip Events in Costa Rica Detected by Continuous GPS Observations, 2002-2011. *Geochemistry Geophysics Geosystems*, **13**(1). 1, 4.3, 4.3, 4.3, 4.3, 4.4, 4.3
- Jimenez-Munt, I., Sabadini, R., Gardi, A., and Bianco, G.** (2003). Active deformation in the Mediterranean from Gibraltar to Anatolia inferred from numerical modeling and geodetic and seismological data. *Journal of Geophysical Research*, **108**(B1), 2006. 2.2.1
- Johansson, J. M., Davis, J. L., Scherneck, H.-G., Milne, G. A., Vermeer, M., Mitrovica, J. X., Bennett, R. A., Jonsson, B., Elgered, G., Elósegui, P., Poutanen, M., Rönnäng, B. O., and Shapiro, I. I.** (2002). Continuous GPS measurements of postglacial adjustment in Fennoscandia 1. Geodetic results. *Journal of Geophysical Research*, **107**(B8). 4.1
- Johnson, H. O. and Agnew, D. C.** (1995). Monument motion and measurements of crustal velocities. *Geophysical Research Letters*, **22**(21), 2905–2908. 3.1, 4.1
- Kahle, H.-G., Cocard, M., Peter, Y., Geiger, A., Reilinger, R., Barka, A., and Veis, G.** (2000). GPS-derived strain rate field within the boundary zones of the Eurasian, African, and Arabian Plates. *Journal of Geophysical Research*, **105**(B10), 23,353–23,370. 2.2.1
- Kasdin, N. J.** (1995). Discrete Simulation of Colored Noise and Stochastic Processes and $1/f^\alpha$ Power Law Noise Generation. *Proceedings of the IEEE*, **83**(5). 3.3.1
- King, G. C. P., Stein, R. S., and Lin, J.** (1994). Static stress changes and the triggering of earthquakes. *Bulletin of the Seismological Society of America*, **84**(3), 935–953. 2.3.5

- King, M. A. and Williams, S. D. P.** (2009). Apparent stability of GPS monumentation from short-baseline time series. *Journal of Geophysical Research*, **114**(B10403). 3.1
- Kreemer, C., Haines, J., Holt, W. E., Blewitt, G., and Lavallee, D.** (2000). On the determination of a global strain rate model. *Earth, Planets, and Space*, **52**, 765–770. 2.2.1
- LaFemina, P., Dixon, T. H., Govers, R., Norabuena, E., Turner, H., Saballos, A., Mattioli, G., Protti, M., and Strauch, W.** (2009). Fore-arc motion and Cocos Ridge collision in Central America. *Geochemistry Geophysics Geosystems*, **10**(Q05S14). 4.3
- Langbein, J.** (2004). Noise in two-color electronic distance meter measurements revisited. *Journal of Geophysical Research*, **109**(B04406). 3.1
- Langbein, J.** (2008). Noise in GPS displacement measurements from Southern California and Southern Nevada Noise in GPS displacement measurements from Southern California and Southern Nevada. *Journal of Geophysical Research*, **113**(B05405). 3.1, 4.1
- Langbein, J. and Johnson, H.** (1997). Correlated errors in geodetic time series: Implications for time-dependent deformation. *Journal of Geophysical Research*, **102**(B1), 591–603. 3.1
- Langbein, J. O., Linker, M. F., McGarr, A. F., and Slater, L. E.** (1987). Precision of two-color geodimeter measurements: Results from 15 months of observations. *Journal of Geophysical Research*, **92**(B11), 11644–11656. 3.1
- Larson, K. M.** (2009). GPS seismology. *Journal of Geodesy*, **83**(3-4), 227–233. 1
- Le Bail, K.** (2004). *Etude statistique de la stabilité des stations de géodésie spatiale - Application à DORIS*. Dissertation, Institut Géographique National - FRANCE. 3.2
- Lisowski, M., Dzurisin, D., Denlinger, R. P., and Iwatsubo, E. Y.** (2008). Analysis of GPS-Measured Deformation Associated with the 2004–2006 Dome-Building Eruption of Mount St. Helens, Washington. In D. R. Sherrod, W. E. Scott, and P. H. Stauffer, Herausgeber, *A Volcano Rekindled: The Renewed Eruption of Mount St. Helens, 2004–2006*, chapter 15, Seiten 301–333. USGS Professional Paper 1750. 4.5, 4.8

REFERENCES

- Lomb, N. R.** (1976). Least-squares frequency analysis of unequally spaced data. *Astrophysics and Space Science*, **39**, 447–462. 3.2, 3.3.1, 3.2
- Malservisi, R., Furlong, K., and Dixon, T.** (2001). Influence of the earthquake cycle and lithospheric rheology on the dynamics of the Eastern California shear zone. *Geophysical Research Letters*, **28**(14), 2731–2734. 4.1
- Malservisi, R., Gans, C., and Furlong, K.** (2005). Microseismicity and Creeping Faults: Hints from Modeling the Hayward Fault, California (USA). *Earth Plan. Sci. Lett.*, **234**(3-4), 421–435. 2.3.4
- Malservisi, R., Hugentobler, U., Wonnacott, R., and Chacko, R.** (2008). How rigid is a rigid plate? Geodetic constraint from the Kalahari craton, South Africa. European Geosciences Union General Assembly 2008, Vienna, Austria. 3.4
- Malservisi, R., Hugentobler, U., Wonnacott, R., and Hackl, M.** (2012). How rigid is a rigid plate? Geodetic constraint from the TrigNet CGPS network, South Africa. *submitted to Geophysical Journal International*. 1, 4.5
- Mandelbrot, B. B.** (1983). *The Fractal Geometry of Nature*. Freeman, San Francisco. 3.2
- Mandelbrot, B. B. and Van Ness, J. W.** (1968). Fractional Brownian Motions, Fractional Noises and Applications. *SIAM Review*, **10**(4), 422–437. 3.2
- Mao, A., Harrison, C. G. A., and Dixon, T. H.** (1999). Noise in GPS coordinate time series. *Journal of Geophysical Research*, **104**(B2), 2797–2816. 3.1, 3.3.2, 3.4, 4.1, 4.4
- McCaffrey, R.** (1992). Oblique Plate Convergence, Slip Vectors, and Fore-arc Deformation. *Journal of Geophysical Research*, **97**(B6), 8905–8915. 4.3
- McGuire, R. K.** (1993). Computations of seismic hazard. *Annals of Geophysics*, **36**(3-4). 2.1

- Michaud, F., Sosson, M., Royer, J.-Y., Chabert, A., Bourgois, J., Calmus, T., Mortera, C., Bigot-Cormier, F., Bandy, W., Dymment, J., Pontoise, B., and Sichler, B. (2004). Motion partitioning between the Pacific plate, Baja California and the North America plate: The Tosco-Abreojos fault revisited. *Geophysical Research Letters*, **31**(L08604). 2.1
- Miller, M. M., Melbourne, T., Johnson, D. J., and Sumner, W. Q. (2002). Periodic Slow Earthquakes from the Cascadia Subduction Zone. *Science*, **295**(5564), 2423. 4.4
- Milotti, E. (2006). PLNoise: a package for exact numerical simulation of power-law noises. *Computer Physics Communication*, **175**, 212–225. 3.3.1
- Muir-Wood, R. (1993). From global seismotectonics to global seismic hazard. *Annals of Geophysics*, **36**(3-4). 2.1
- Nadeau, R. M. and Guilhem, A. (2009). Nonvolcanic Tremor Evolution and the San Simeon and Parkfield, California, Earthquakes. *Science*, **325**(5937), 191–193. 2.3.5
- Oppenheim, A. V. and Schaffer, R. W. (1989). *Discrete-Time Signal Processing*. Prentice Hall. 3.3.1
- Outerbridge, K. C., Dixon, T. H., Schwartz, S. Y., Walter, J. I., Protti, M., Gonzalez, V., Biggs, J., Thorwart, M., and Rabbel, W. (2010). A tremor and slip event on the Cocos-Caribbean subduction zone as measured by a global positioning system (GPS) and seismic network on the Nicoya Peninsula, Costa Rica. *Journal of Geophysical Research*, **115**(B10408). 4.3, 4.3, 4.3
- Palano, M., Guarrera, E., and Mattia, M. (2012). GPS ground deformation patterns at Mount St. Helens (Washington, USA) from 2004 to 2010. *Terra Nova*, Seiten 148–155. 4.5
- Perfettini, H. and Avouac, J.-P. (2007). Modeling afterslip and aftershocks following the 1992 Landers earthquake. *Journal of Geophysical Research*, **112**(B7), 1–19. 4.1
- Plattner, C., Malservisi, R., Dixon, T. H., Lafemina, P., Sella, G. F., Fletcher, J., and Suarez-Vidal, F. (2007). New constraints on relative motion between the Pacific Plate and Baja California microplate

REFERENCES

- (Mexico) from GPS measurements. *Geophysical Journal International*, **170**, 1373–1380. 2.3.1, 2.3.2, 4.5
- Prescott, W. H., Savage, J. C., Svarc, J. L., and Manaker, D.** (2001). Deformation across the Pacific-North America plate boundary near San Francisco, California. *Journal of Geophysical Research*, **106**, 6673–6682. 2.3.1
- Reid, H. F.** (1910). The mechanics of the earthquake: the California earthquake of April, 18, 1906, Report of the State Investigation Commission, v.2. Technical report, Carnegie Institution of Washington. 2.1
- Rogers, G. and Dragert, H.** (2003). Episodic Tremor and Slip on the Cascadia Subduction Zone: The Chatter of Silent Slip. *Science*, **300**(5627), 1942–1943. 4.4
- Rutman, J.** (1978). Characterization of phase and frequency instabilities in precision frequency sources: Fifteen years of progress. *Proceedings of the IEEE*, **66**(9), 1048–1075. 3.1, 3.2
- Saballos, J. A., Malservisi, R., Connor, C. B., La Femina, P. C., and Wetmore, P.** (2012). Gravity and geodesy of Concepcion volcano, Nicaragua. In J. L. Palma, W. I. Rose, N. Varley, and H. Delgado, Herausgeber, *Open-Vent Volcanism and Related Hazards*. Geological Society of America Special Paper (in press). 4.1
- Sandwell, D., Becker, T., Bird, P., Freed, A., Hackl, M., Holt, W., Hooks, B., Kedar, S., Kreemer, C., McCaffrey, R., Meade, B., Parsons, T., Pollitz, F., Shen, Z.-K., Smith-Konter, B., Tape, C., and Zeng, Y.** (2010). Comparison of 16 Strain-Rate Maps of Southern California. SCEC Presentation. 1, 5
- Santamaría-Gómez, A., Bouin, M.-N., Collilieux, X., and Wöppelmann, G.** (2011). Correlated errors in GPS position time series: Implications for velocity estimates. *Journal of Geophysical Research*, **116**(B01405). 3.1
- Savage, J. C. and Lisowski, M.** (1998). Viscoelastic coupling model of the San Andreas Fault along the big bend, southern California. *Journal of Geophysical Research*, **103**, 7281–7292. 2.3.4, 2.4, 4.1

- Scargle, J. D.** (1982). Studies in astronomical time series analysis. II - Statistical aspects of spectral analysis of unevenly spaced data. *Astrophysical Journal*, **263**, 835–853. 3.2, 3.3.1, 3.2
- Schmalzle, G., Dixon, T., Malservisi, R., and Govers, R.** (2006). Strain accumulation across the Carrizo segment of the San Andreas Fault, California: Impact of laterally varying crustal properties. *Journal of Geophysical Research*, **111**(B05403). 4.1
- Schmidt, D. A. and Gao, H.** (2010). Source parameters and time-dependent slip distributions of slow slip events on the Cascadia subduction zone from 1998 to 2008. *Journal of Geophysical Research*, **115**(B00A18). 4.1
- Schwartz, S. Y. and Rokosky, J. M.** (2007). Slow slip events and seismic tremor at circum-Pacific subduction zones. *Reviews of Geophysics*, **45**(3). 4.1
- Scott, W. E., Sherrod, D. R., and Gardner, C. A.** (2008). Overview of the 2004 to 2006, and Continuing, Eruption of Mount St. Helens, Washington. In D. R. Sherrod, W. E. Scott, and P. H. Stauffer, Herausgeber, *A Volcano Rekindled: The Renewed Eruption of Mount St. Helens, 2004-2006*, chapter 1, Seiten 3–22. USGS Professional Paper 1750. 4.5
- Segall, P.** (2010). *Earthquake and Volcano Deformation*. Princeton University Press. 3.1
- Segall, P. and Davis, J. L.** (1997). GPS Applications for Geodynamics and Earthquake Studies. *Annual Review of Earth and Planetary Sciences*, **25**, 301–+. 1, 4.1
- Sella, G. F., Stein, S., Dixon, T. H., Craymer, M., James, T. S., Mazzotti, S., and Dokka, R. K.** (2007). Observation of glacial isostatic adjustment in stable North America with GPS. *Geophysical Research Letters*, **34**(2), 1–6. 4.1
- Shen, Z.-K., Jackson, D. D., and Ge, B. X.** (1996). Crustal deformation across and beyond the Los Angeles basin from geodetic measurements. *Journal of Geophysical Research*, **101**(B12), 27,957–27,980. 2.2.1
- Shen, Z.-K., Agnew, D. C., King, R. W., Dong, D., Herring, T. A., Wang, M., Johnson, H., Anderson, G., Nikolaidis, R.,**

REFERENCES

- van Domselaar, M., Hudnut, K. W., and Jackson, D. D. (2003). SCEC crustal motion map, version 3.0: <http://epicenter.usc.edu/cmm3/> (September 2008). 2.3.2
- Smolka, A. (2007). Schadenspiegel - Special feature issue Risk factor of earth. Technical report, Munich Re. 2.1
- Spakman, W. and Nyst, M. (2002). Inversion of relative motion data for estimates of the velocity gradient field and fault slip. *Earth and Planetary Science Letters*, **203**, 577–591(15). 2.2.1
- Stamps, D. S., Calais, E., Saria, E., Hartnady, C., Nocquet, J.-M., Ebinger, C. J., and Fernandez, R. M. (2008). A kinematic model for the East African Rift. *Geophysical Research Letters*, **35**(L05304). 3.5
- Stoica, P. and Moses, R. L. (1997). *Introduction to Spectral Analysis*. Prentice Hall. 3.3.1
- Strang, G. and Borre, K. (1997). *Linear algebra, geodesy, and GPS*. Wellesley-Cambridge Press. 4.2, 4.2
- Szeliga, W., Melbourne, T., Santillan, V., and Miller, M. (2008). GPS constraints on 34 slow slip events within the Cascadia subduction zone, 1997 - 2005. *Journal of Geophysical Research*, **113**(B04404). 4.1, 4.4
- Tryon, M. D. (2009). Monitoring aseismic tectonic processes via hydrologic responses: An analysis of log-periodic fluid flow events at the Costa Rica outer rise. *Geology*, **37**(2). 4.3
- Walter, J. I., Schwartz, S. Y., Protti, J. M., and Gonzalez, V. (2011). Persistent tremor within the northern Costa Rica seismogenic zone. *Geophysical Research Letters*, **38**(L01307). 4.3
- Wdowinski, S., Bock, Y., Zhang, J., Fang, P., and Genrich, J. (1997). Southern California permanent GPS geodetic array: Spatial filtering of daily positions for estimating coseismic and postseismic displacements induced by the 1992 Landers earthquake. *Journal of Geophysical Research*, **102**, 18,057–18,070. 4.1
- Wdowinski, S., Sudman, Y., and Bock, Y. (2001). Geodetic detection of active faults in S. California. *Geophysical Research Letters*, **28**, 2321–2324. 2.2.1

- Wdowinski, S., Smith-Konter, B., Bock, Y., and Sandwell, D.** (2007). Diffuse interseismic deformation across the Pacific-North America plate boundary. *Geology*, **35**(4), 311–314. 2.2.1, 2.3.4
- Welch, P.** (1967). The use of fast Fourier transform for the estimation of power spectra: A method based on time averaging over short, modified periodograms. *IEEE Transactions on Audio and Electroacoustics*, **15**(2). 3.3.1
- Wessel, P. and Bercovici, D.** (1998). Interpolation with Splines in Tension: A Green's Function Approach. *Mathematical Geology*, **30**(1), 77–93. 2.1, 2.2.2
- Wessel, P. and Smith, W. H. F.** (1991). Free software helps map and display data. *EOS Transactions*, **72**, 441–441. 2.3.3, 3.6
- Williams, S. D. P.** (2003a). Offsets in Global Positioning System time series. *Journal of Geophysical Research*, **108**(B6). 3.3.4, 4.1, 4.3
- Williams, S. D. P.** (2003b). The effect of coloured noise on the uncertainties of rates estimated from geodetic time series. *Journal of Geodesy*, **76**(9-10), 483–494. 3.1, 3.3.1, 4.1
- Williams, S. D. P.** (2008). CATS: GPS coordinate time series analysis software. *GPS Solutions*, **12**(2), 147–153. 3.1, 3.2
- Williams, S. D. P., Bock, Y., Fang, P., Jamason, P., Nikolaidis, R. M., Prawirodirdjo, L., Miller, M., and Johnson, D. J.** (2004). Error analysis of continuous GPS position time series. *Journal of Geophysical Research*, **109**(B03412). 3.1, 4.1
- Wyatt, F. K.** (1982). Displacement of surface monuments: Horizontal motion. *Journal of Geophysical Research*, **87**(B2), 979–989. 3.1
- Wyatt, F. K.** (1989). Displacement of surface monuments - Vertical motion. *Journal of Geophysical Research*, **94**, 1655–1664. 3.1
- Zhang, J., Bock, Y., Johnson, H., Fang, P., Williams, S., Genrich, J., Wdowinski, S., and Behr, J.** (1997). Southern California Permanent GPS Geodetic Array: Error analysis of daily position estimates and site velocities. *Journal of Geophysical Research*, **102**(B8), 18,035–18,055. 3.1, 3.3.2, 4.1

Acknowledgments

An dieser Stelle möchte ich mich bei allen bedanken, die mir bei der Erstellung dieser Arbeit geholfen haben.

Mein besonderer Dank gilt dabei Rocco Malservisi, der alle meine wissenschaftliche Arbeiten seit der Diplomarbeit betreut und begleitet hat. Durch ihn bin ich auf das Thema dieser Arbeit gekommen. Dabei hat er mich immer unterstützt und stand stets mit Rat und Tat zur Seite. Nach seinem Wechsel nach Florida hat er ständigen Kontakt gehalten und mich dort über Monate aufgenommen. Mit seinem wertvollen Wissen und vielen Diskussionen hat er wesentlich zum Gelingen dieser Arbeit beigetragen.

Besonders bedanken möchte ich mich auch bei Valerian Bachtadse, der nach dem Weggang Roccas ohne zu zögern die Betreuung dieser Arbeit übernommen hat. Ohne seine vielfältige Unterstützung wäre diese Arbeit nicht möglich gewesen.

Desweiteren möchte ich mich bei Urs Hugentobler bedanken, der immer wieder bereitwillig sein Wissen und seine wertvolle Zeit teilte. Seine Ideen, seine kritischen Fragen und seine Expertise haben einen wesentlichen Beitrag zu dieser Arbeit an der Schnittstelle von Geodäsie und Geophysik geleistet.

Bedanken möchte ich mich auch bei der Arbeitsgruppe Geodynamik von Peter Bunge und bei den Doktorandenkollegen, besonders bei meinen Zimmerkollegen Katha Aubele und Uwe Kirscher für die angenehme Arbeitsatmosphäre.

Schließlich möchte ich meinen Eltern, meiner Familie und meinen Freunden danken für ihre Unterstützung während dieser Arbeit. Sie haben nie einen Zweifel am Erfolg meiner Arbeit aufkommen lassen und mich während dieser Zeit immer ertragen.

Curriculum Vitae

Personal Information

Name: Hackl, Matthias

Date and Place of Birth: 13.03.1980, Bad Tölz

Education

since 2008: Doctoral candidate at the Department of Earth- and Environmental Sciences, Ludwig-Maximilians-Universität, Munich.

2008: Diploma degree (1.53) in Geophysics from Ludwig-Maximilians-Universität, Munich.

2001: Alternative civilian service in Posadas, Argentina.

2000: University-entrance diploma (Abitur: 1.7)
